



מכון ויצמן למדע  
WEIZMANN INSTITUTE OF SCIENCE

Thesis for the degree  
***Doctor of Philosophy***

חבור לשם קבלת התואר  
**דוקטור לפילוסופיה**

By  
***Sven Rühle***

מאת  
**סוון רולה**

מעבר אלקטרונים בשכבת  $TiO_2$  מזופורוזיבית  
ותכונות המגע החשמלי בממשק בין מוליך ל  $TiO_2$

***Electron transport in mesoporous  $TiO_2$  structures  
and  
contact properties at the  $TiO_2$ /conductive substrate interface***

Advisor  
***Prof. David Cahen***

מנחה  
**פרופ' דוד כאהן**

October 2004

חשוון תשס"ה

Submitted to the Scientific Council of the  
Weizmann Institute of Science  
Rehovot, Israel

מוגש למועצה המדעית של  
מכון ויצמן למדע  
רחובות, ישראל



## Abstract

Dye-sensitized solar cells (DSSCs) are a promising low cost alternative to conventional single- or poly-crystalline  $p$ - $n$  junction solar cells. DSSCs consist of a mesoporous  $\text{TiO}_2$  film, sintered onto a conducting transparent substrate. The mesoporous film is covered with a monolayer of dye and immersed into a redox electrolyte, which is electrically connected via a Pt counter electrode. Upon illumination electrons are injected from the excited dye state into the  $\text{TiO}_2$  conduction band while the oxidized dye cation is recharged by the electrolyte.

A major difference in DSSCs, compared to  $p$ - $n$  junction cells is the unipolar charge transport inside the mesoporous  $\text{TiO}_2$  film and the electrolyte. Charge separation occurs at the  $\text{TiO}_2$ /dye/electrolyte interface and electrons diffuse towards the transparent front contact, while positive charges diffuse through the electrolyte to the counter electrode. Electron transport through the  $\text{TiO}_2$  film occurs always close to an interface with the conducting phase that contains the positive counter charges. This interface area is up to three orders of magnitude larger than the geometric surface area of the mesoporous  $\text{TiO}_2$  film. Electronic gap states present at the  $\text{TiO}_2$  surface are thought to act as electron traps, which slow down the electron diffusion process tremendously. Therefore I focused on the question ‘*what controls electron transport through mesoporous  $\text{TiO}_2$  films, immersed in an electrolyte?*’

To investigate electron transport in mesoporous  $\text{TiO}_2$  films and in DSSCs I used the experimental tool of molecular modification and studied the effect on the solar cell characteristics. These measurements revealed that the open circuit voltage changes in a systematic fashion with the dipole moment of the molecules used for modification. Surprisingly, also the short circuit current was affected in a similar fashion. While the effect on the photovoltage can be explained by a dipole-induced shift of the  $\text{TiO}_2$  conduction band, it is not obvious how the molecules affect the photocurrent in such devices. Steady state and time-resolved transport measurements were performed to investigate the molecular effect on the conductivity in more detail and to understand the fundamentals of electron migration through nano-structured materials.

Steady state measurements were carried out in a bipotentiostat system and major efforts were made to produce micrometer sized, interdigitated electrodes by photolithography. It turned out to be rather complicated to get experimental control over the system so that reproducible results could only be achieved with a limited number of molecules. I found that the most pronounced molecular effect on the conductivity is related to the earlier mentioned dipole-induced shift of the TiO<sub>2</sub> conduction band.

Time-resolved photocurrent transient measurements turned out to be a suitable tool for a fundamental investigation of the effect of electronic gap states and electron recombination on the electron transport. A UV laser was used for photo-excitation and a simplified model system without surface-adsorbed organic molecules was used to avoid irreversible photo-catalytic reactions on the TiO<sub>2</sub> surface. I used the pH value of the aqueous electrolyte to change the TiO<sub>2</sub> surface chemistry and, thereby, the rate constant for electron recombination into the electrolyte. Furthermore, I used potential- and intensity-dependent measurements to investigate the effect of trap filling.

To analyze the experimental results I developed a numerical program to simulate photocurrent transients.<sup>1</sup> Comparison of measured with simulated transients showed clearly that the transport in the nano-structured TiO<sub>2</sub> films is dispersive which is consistent with reported results in the literature. While simplified models to describe photocurrent transients have been published, these models either do not consider dispersive transport or are restricted to a very simplified dispersion. The model presented in this work includes dispersive transport in a more quantitative fashion, which can be correlated to the trap distribution in the TiO<sub>2</sub>.

Comparison of intensity dependent measurements with simulations showed, furthermore, that recombination in TiO<sub>2</sub> is highly non-linear with increasing excess electron density in the TiO<sub>2</sub>. This finding is very relevant for appropriate description of transients as well as for solar cell operation, because it shows that the recombination mechanism is very different from what is known in solid state devices

---

<sup>1</sup> Parts of the theoretical model were conceptual developed with 2 other Ph.D. students, in a sub-project that I initiated within the framework of an EU FP5 research training network, "ETA solar cells". My collaborators were Cateljine Grasso (Ghent University, Belgium) and Kristofer Fredin (Uppsala University, Sweden). All the programming needed for this was done by me.

(e.g. Shockley-Read-Hall, Auger or radiative recombination). Transient measurements furthermore showed that the FTO/TiO<sub>2</sub> interface has an impact on the photocurrent response.

Incident laser light from the FTO side was used to generate electron-hole pairs at the FTO/TiO<sub>2</sub> interface and to investigate the electrostatic potential distribution close to the FTO. Mesoporous TiO<sub>2</sub>/FTO and compact TiO<sub>2</sub>/FTO interfaces were measured and the results indicate that the electrostatic potential drop appears across the entire compact TiO<sub>2</sub> layer, while it drops on a very small distance within the first layer of TiO<sub>2</sub> particles at the mesoporous TiO<sub>2</sub>/FTO interface.

The importance of an electrostatic built-in field for the operation of DSSCs is still a matter of controversy and a commonly accepted theory about the DSSC working principle is missing. The main disagreement concerns the electrostatic field at the interface between the TiO<sub>2</sub> and the conducting FTO substrate. Several models were proposed which required, implicitly or explicitly, some built-in field at this interface, even though there is lack of direct experimental evidence for such a field. The second major part of my thesis was dedicated to the question *‘what is the working principle of DSSCs and how important is a built-in electrostatic field at the substrate/TiO<sub>2</sub> interface for cell operation?’*

Finally, I used the insights gained from the steady state and transient measurements and from the simulations to clarify the working principle of DSSCs. For this I derived a model based on experimental data from Kelvin probe measurements. I obtained the necessary work function data by modifying existing equipment and methodology to allow measurements of both, solids and liquids, with respect to the same reference. These data indicate that an energy barrier exists at the FTO/TiO<sub>2</sub> interface in the dark, in contrast to all existing models which are based on an electrostatic built-in field. I derived a model based on electron tunneling through a thin barrier at the FTO/TiO<sub>2</sub> interface. Due to the specific geometric boundary conditions this model is restricted to DSSCs with a mesoporous TiO<sub>2</sub>/FTO interface, which is the most common DSSC configuration. For DSSCs with a compact TiO<sub>2</sub> layer electron hopping is proposed to be the dominant transport mechanism the presence of a barrier at the FTO/TiO<sub>2</sub> interface.



## Acknowledgements

I would like to thank my advisor Prof. David Cahen and all the members of the Cahen-group for the good working atmosphere. I would like to express my gratefulness to my advisor that he gave me the opportunity to present scientific results and to represent our group in international meetings. This showed his faith and confidence in my work which was important to gain self-confidence and to grow as an independent scientist. Furthermore I learned from him that it is important to keep always the big picture in mind, to put scientific aspects together and to see the work in broader context.

I would like to thank Prof. Arie Zaban (Bar Ilan University) and his group for help and advice in all kinds of aspects related to mesoporous TiO<sub>2</sub> films and DSSCs. Especially I would like to thank for the opportunity to use his lab facilities and to have extended access to the bipotentiostat system in order to perform conductivity measurements.

I thank Dr. Diana Mahalu and Dr. Roman Krane for advice in mask design and help to establish a photolithography procedure to produce interdigitated electrodes in the facilities of the submicron center of the Weizmann Institute. Furthermore I thank Dr. Alexander Yoffe and Dr. Miron Hazani for help and support to develop a lithography procedure in the clean room facilities of the Department of Material and Interfaces.

Electrochemical modification of the mesoporous TiO<sub>2</sub> films was done at the University of Tel Aviv and I would like to thank Alexandra Merson for help with the deposition process.

I thank Prof. Gary Hodes for fruitful discussions about photo-electrochemical solar cells and photovoltaic concepts and Prof. Israel Rubenstein for advice regarding electrochemical measurements. Furthermore I would like to thank Dr. Leeor Kronik for scientific discussions related to all aspects of Kelvin probe measurements. Dr. Igor Lubomirsky and Dr. Michael Rappaport I thank for technical advice in the design of

vacuum systems. I am grateful for technical support which was provided by Menashe Lev, Reuven Dagan, Reuven De-Roos, John Harrison, Moshe Gantz and Naomi Raz.

This PhD thesis was done in the framework of the ETA project (RTN), financed by the European Union, and I would like to acknowledge partial financial support, given by the project. Furthermore I thank all the partners involved in the project for the very friendly and productive atmosphere. My special thanks is dedicated to the coordinator of the project, Dr. Jeanette Wienke, who put a lot of emphasis on the training aspects of us, the young researches, and gave us the opportunity to present our scientific results during the network meetings by ourselves.

Special thanks to Dr. Thomas Dittrich from the Hahn-Meitner-Institute, Berlin, who invited me to his lab for one month to perform time resolved transport measurements (conducted in the framework of the ETA project).

I am thankful for partial financial support from the Minerva foundation, Munich.

I would like to thank Yehudit Rousso, Osnat Lotan, Herut Sharan and Galia August for help and support in administrative issues.

I want to thank Adi Salomon, Dr. Yoram Selzer, Shikma Tsuray, Olivia Niitsoo, Dr. Hossam Haick, Dr. Iris Visoly-Fisher, Dr. Tao He, Shaibal Sarkar, Shira Yohelis, Tali Aqua, Dr. Olga Girshevitz, Dr. Jamal Ghabboun, Dr. Yiftach Nevo, Christophe Pejoux, Dr. Ayelet Vilan, Dr. Yongdong Jin, Dr. Doron Gal, Dr. Yizhak Mastai, Supratim Guha Ray, Inbal Friedler and Erez Boukobza for the very friendly atmosphere in my working environment, for scientific advice and discussions and for chocolate and candies which were brought after travels from abroad.

Last but not least I want to thank my parents and my sister for support whenever it was needed.

# Table of contents

<b>SYMBOLS AND ABBREVIATIONS.....</b>	<b>5</b>
<b>1 INTRODUCTION.....</b>	<b>7</b>
1.1 World energy consumption and greenhouse effect.....	7
1.2 Alternative energy sources .....	7
1.3 Solar energy for electricity production .....	8
1.4 Nano-composite solar cells .....	9
<b>2 THEORETICAL BACKGROUND.....</b>	<b>12</b>
<b>2.1 Working principle of solar cells.....</b>	<b>12</b>
2.1.1 Potentials and quasi-Fermi levels .....	13
2.1.2 Driving forces for electron and hole currents .....	16
2.1.3 Contact selectivity.....	17
2.1.4 The open circuit voltage.....	18
2.1.5 Solar cells without electrostatic built-in field .....	20
2.1.6 Solar cell characteristics.....	21
<b>2.2 The dye-sensitized solar cell.....</b>	<b>22</b>
2.2.1 The kinetic model.....	23
2.2.2 The junction model .....	25
2.2.3 The thermionic emission model.....	27
<b>2.3 Electron transport in mesoporous TiO<sub>2</sub> films .....</b>	<b>31</b>
2.3.1 Trapping/detrapping and hopping transport.....	31
2.3.2 Molecular modification of semiconductor surfaces.....	32
<b>3 EXPERIMENTAL SECTION .....</b>	<b>34</b>
<b>3.1 Solar cell measurements .....</b>	<b>34</b>
3.1.1 TiO <sub>2</sub> electrode preparation and characterization.....	34
3.1.2 Fabrication of compact TiO <sub>2</sub> underlayers .....	35
3.1.3 Fabrication of dye-sensitized solar cells .....	35
3.1.4 Molecular modification of mesoporous TiO <sub>2</sub> electrodes .....	36
3.1.5 Optical absorption measurements .....	36
3.1.6 I-V characterization of dye-sensitized solar cells .....	37

<b>3.2</b>	<b>Electron transport measurements .....</b>	<b>37</b>
3.2.1	Preparation of interdigitated micro-electrodes.....	37
3.2.2	Electrochemical modification of TiO <sub>2</sub> films on gap electrodes.....	38
3.2.3	Bi-potentiostat measurements .....	39
3.2.4	Photocurrent transient measurements .....	39
<b>3.3</b>	<b>Investigation of the FTO/TiO<sub>2</sub> interface .....</b>	<b>41</b>
3.3.1	Transient spectroscopy of the FTO/TiO <sub>2</sub> contact .....	41
3.3.2	Kelvin Probe measurements on liquids.....	42
3.3.3	Numerical simulations .....	43
<b>4</b>	<b>RESULTS .....</b>	<b>44</b>
<b>4.1</b>	<b>Molecular modification of DSSCs .....</b>	<b>45</b>
4.1.1	<i>I-V</i> characteristics of molecular modified DSSCs .....	45
4.1.2	Molecular impact on the $V_{oc}$ and $I_{sc}$ .....	47
<b>4.2</b>	<b>Electron transport in TiO<sub>2</sub> films I: Bi-potentiostat measurements.....</b>	<b>49</b>
4.2.1	Molecular effect on the conductivity in mesoporous TiO <sub>2</sub> films.....	52
<b>4.3</b>	<b>Electron transport in TiO<sub>2</sub> films II: Photocurrent transients.....</b>	<b>54</b>
4.3.1	Potential dependence of photocurrent transients .....	56
4.3.2	Light intensity dependence of photocurrent transients .....	58
4.3.3	pH dependence of photocurrent transients.....	60
<b>4.4</b>	<b>Electron transport in TiO<sub>2</sub> films III: Numerical simulations .....</b>	<b>61</b>
4.4.1	The SLICE model for numerical photo-transient simulations .....	61
4.4.2	Simulations I: Dispersive transport without recombination .....	69
4.4.3	Determination of $D_e$ from thickness-dependent measurements.....	71
4.4.4	Simulations II: Non-dispersive transport with recombination.....	72
4.4.5	Simulations III: Dispersive transport with recombination .....	74
4.4.6	Simulations IV: The impact of the <i>RC</i> -time constant.....	77
<b>4.5</b>	<b>Investigation of the TiO<sub>2</sub>/substrate interface.....</b>	<b>79</b>
4.5.1	Potential-dependent transients .....	80
4.5.2	pH dependent transients .....	81
<b>4.6</b>	<b>The tunnel model for dye-sensitized solar cells .....</b>	<b>82</b>
4.6.1	Work function and redox potential measurements .....	82
4.6.2	Band edge movement and band bending in mesoporous TiO <sub>2</sub> films.....	85
4.6.3	The electrostatic potential distribution at the mesoporous TiO <sub>2</sub> /FTO interface	89
4.6.4	Electron tunneling at the metal/barrier/TiO <sub>2</sub> interface.....	90
4.6.5	Simulated <i>I-V</i> characteristics for DSSCs based on the tunnel model .....	93

<b>5</b>	<b>DISCUSSION .....</b>	<b>96</b>
<b>5.1</b>	<b>Molecular modification and electron transport .....</b>	<b>96</b>
5.1.1	Solar cell measurements.....	97
5.1.2	Molecular effect on the conductivity .....	100
<b>5.2</b>	<b>Dispersive transport and trap filling.....</b>	<b>103</b>
5.2.1	Dispersive transport: Qualitative analysis.....	105
5.2.2	Dispersive transport: Numerical analysis .....	107
<b>5.3</b>	<b>Numerical simulations including recombination .....</b>	<b>111</b>
<b>5.4</b>	<b>Investigation of the FTO/TiO<sub>2</sub> interface .....</b>	<b>114</b>
5.4.1	The impact of the <i>RC</i> contact on photocurrent transients.....	118
<b>5.5</b>	<b>The tunnel model.....</b>	<b>122</b>
<b>6</b>	<b>CONCLUSIONS .....</b>	<b>125</b>
	<b>APPENDIX A: Simulation input parameters.....</b>	<b>129</b>
	<b>APPENDIX B: Contact free photovoltage measurements.....</b>	<b>130</b>
	<b>APPENDIX C: List of publications.....</b>	<b>131</b>
	<b>REFERENCES.....</b>	<b>133</b>



# List of Symbols and Abbreviations

Abbreviation	Explanation
$A^*$	Richardson constant
$CB$	Conduction band
$CE$	Counter electrode
$CPD$	Contact potential difference
$D_{CB}$	Density distribution in energy space of electronic states in the CB
$D_{ox}$	Density distribution in energy space of oxidized redox species
$D_{red}$	Density distribution in energy space of reduced redox species
$D_e$	Electron diffusion coefficient
$D_h$	Hole diffusion coefficient
$dp$	Dispersion coefficient
DSSC	Dye-sensitized solar cell
$\vec{E}$	Electric field vector
$E_{CB}$	Conduction band energy level
$E_g$	Energy gap
$E_F$	Fermi level (electrochemical potential of electrons)
$E_{Fn}$	Electron quasi-Fermi level
$E_{Fp}$	Hole quasi-Fermi level
$E_{loc}$	Local vacuum level
$E_{redox}$	Redox potential of the electrolyte (electrochemical potential of electrons)
$E_{ref}$	Reference energy level
$E_t$	Energy level of a trap state
$E_{VB}$	Valence band energy level
$ETA$	Extreme thin absorber
$FF$	Fill factor
$FTO$	F-doped tin oxide ( $\text{SnO}_2:\text{F}$ )
$h$	Planck constant
$HL$	Helmholtz layer
$I_0$	Laser energy per pulse
$I_{sc}$	Short circuit current
$J_b$	Current through FTO/ $\text{TiO}_2$ interface barrier
$J_e$	Electron current density
$J_h$	Hole current density
$J_G$	Generation current density
$J_R$	Recombination current density
$J_{sc}$	Short circuit current density
$k_B$	Boltzmann constant
$K_n$	Recombination rate constant
$kp$	Recombination exponent
$KP$	Kelvin Probe
$L$	$\text{TiO}_2$ film thickness
$n_{if}$	Ideality factor
$n$	Electron density
$N_{CB}$	Effective density of electronic states at the bottom of the CB
$N_{VB}$	Effective density of electronic states at the top of the VB
$m_e^*$	Effective electron mass
$m_h^*$	Effective hole mass

<b>Abbreviation</b>	<b>Explanation</b>
$p$	Hole density
$R$	Resistance
$RE$	Reference electrode
$T$	Absolute temperature
$U$	Electrostatic potential difference
$V_{oc}$	Open circuit voltage
$V_{ph}$	photo voltage
$V_{fb}$	Flat band voltage
$VB$	Valence band
$WE_1$	Working electrode one
$WE_2$	Working electrode two
$q$	Elementary charge
$\varepsilon_0$	Permittivity of free space
$\varepsilon$	Dielectric constant
$\chi$	Electron affinity
$\eta_e$	Electron mobility
$\eta_h$	Hole mobility
$\mu_n$	Chemical potential of electrons
$\mu_p$	Chemical potential of holes
$\varphi$	Electrostatic potential
$\Phi$	Work function
$\sigma$	Conductivity

# 1 Introduction

## 1.1 World energy consumption and greenhouse effect

The global energy demand is steadily growing, on the one hand caused by a steady population growth and on the other hand by increasing average energy consumption per person. The latter trend is particularly pronounced in industrialized countries like the USA and Canada and in European countries. The limited resources of oil, coal and gas require alternative energy sources, which can replace them in the future. Additionally, it seems meanwhile widely accepted that the global warming over the last hundred years is, at least partly, caused by the combustion of fossil energy carriers (oil, coal, gas). CO<sub>2</sub> molecules in the atmosphere absorb the infrared radiation, reflected from the earth and change the energy balance. As a result less radiation reaches outer space and the atmosphere heats up, which is the so-called greenhouse effect. Global warming causes an increase in the sea level due to melting of the polar ice and is, thus, a threat for ocean/sea islands and for countries with a sea-side territories around sea level. An increase in the surface temperature of sea water furthermore increases the probability of heavy storms due to a changed energy exchange between the air and the water. Furthermore, a shift of climate zones can be caused by the greenhouse effect with severe consequences for agriculture. Deserts will grow and take away valuable farm land – an effect with an important impact on water resources and food supply.

## 1.2 Alternative energy sources

Nuclear energy is one candidate to produce electricity without significant CO<sub>2</sub> exhaust, an advantage compared to conventional power plants which burn coal, oil or gas. Nevertheless, nuclear energy has several serious disadvantages. Accidents during regular operation cannot be excluded. The most prominent examples are the accident in Harrisburg (USA) in 1979 and the explosion of the reactor in Chernobyl (former USSR) in 1986, which caused wide-spread contamination with an uncounted number of casualties. Another problem is the storage of radioactive waste, because it requires appropriate technical handling over thousands of years which can only be provided

under stable political boundary conditions. Looking into the history of the last centuries of the countries which are using nuclear energy today one finds several revolutions including two world wars. There is no obvious reason why such harsh political changes will not take place in the future and it is more than doubtful that appropriate storage and maintenance can be provided in the long run.

Other alternatives like fusion are still far away from practical application and do not provide a solution for regions with a low population density. Fusion reactors, if ever available, will have a minimum size of several GW ( $10^9$  W), so that electricity has to be distributed over huge distances.

Wind energy is the most important alternative energy source in Europe today apart from hydroelectric energy. It is a growing sector but restricted to windy regions. Undoubtedly a future energy supply will consist of many components and one part of it will be solar energy.

### **1.3 Solar energy for electricity production**

Solar energy has many advantages as a future energy source. It is everywhere available, creates no CO<sub>2</sub> exhaust, power stations can be realized for every application - from the mW to the MW scale - and the basic ingredient, the “fuel”, sun energy is provided for free. While it is very economical to use solar energy for water heating it is still rather expensive to convert sunlight into electricity. Silicon solar cells are the most prominent ones for this type of energy conversion but the high material requirements and production costs are still the major reason for their high price. To decrease the price for photovoltaic electricity generation the solar cells have to become either more efficient or significant cheaper than they are today. New low-cost materials and new solar cell designs have been proposed in the last years to lower the price for photovoltaic cells. One of the best-known new concepts is the dye-sensitized solar cell (DSSC), based on nanocrystalline TiO<sub>2</sub>. This cell can reach light to electric power conversion efficiency of around 10%.<sup>1,2</sup> Even though this cell was first realized at close to 10 % efficiency some 15 years ago it has not been possible until today to increase its efficiency

significantly. One problem for optimizing the DSSC is that a commonly agreed theory about its working principle is still missing. Especially the possible role of a built-in electrostatic field, such as the one that is central for the operation of Si  $p$ - $n$  solar cells, has raised many questions has been the origin of vivid discussions.

## 1.4 Nano-composite solar cells

DSSCs or in general nano-composite solar cells have a design that is very different from that of one dimensional  $p$ - $n$  junction solar cells. Conventional  $p$ - $n$  junction solar cells consist of a  $p$ -type layer, which acts usually as an absorber, deposited onto an  $n$ -type semiconductor. Figure 1.1a shows schematically a  $p$ - $n$  junction with the negatively charged space charge region in the  $p$ -part of the junction and the positively charged region on the  $n$ -side. Light-generated electron-hole pairs are spatially separated at the  $p$ - $n$  junction so that electrons migrate towards the  $n$ -type side while holes remain in the  $p$ -type part of the cell. Both types of charge carriers then diffuse into the respective metal contact. The  $n$ -type material acts as the electron conductor while the  $p$ -type absorber is the hole conducting layer. Recombination is only relevant in that part of the cell where light-generated electrons and holes are present, i.e., in the  $p$ -type absorber material.

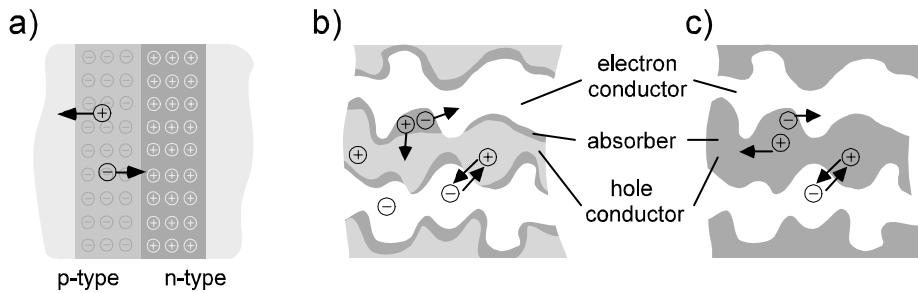


Figure 1.1: (a) Schematic drawing of a conventional  $p$ - $n$  junction solar cell. Electron hole pairs are spatially separated in the junction. (b) Schematic of nano-composite solar cell with an electron and hole conductor and an absorber in between. (c) Nano-composite solar cell where the hole conductor is also the absorber.

In contrast to that nano-composite solar cells form a three-dimensional intercalated network of the electron- and hole-conducting material. The absorber material can be a separate phase, which is located in between the electron and hole conductor, or one of

the conductors can act as an absorber. Such cells are also known as ETA cells, due to the **Extreme Thin Absorber** layer. A schematic drawing of a nano-composite solar cell with a separate absorber is shown in Figure 1.1b while Figure 1.1c shows a cell where the hole-conducting phase is the absorber material.

The concept of nano-composite or ETA solar cells is that electron-hole pairs are always generated close to an interface where they are spatially separated, as shown by arrows pointing away from the counter charge. Bulk recombination inside the absorber is very low due to the small distance to the charge separating interface, which is an advantage of the intercalated structure. The disadvantage of the high interface area is a strong increase in the interface recombination (shown by arrows pointing towards the counter charge).

The nanocrystalline structure gives rise to many open questions about the working principle of such solar cells. The major aspects which are different in such cells are the charge transport due to the intercalated structure and the electrostatic potential distribution due to the absence of macroscopic space charge layers. The subject of this thesis was the investigation of electron transport in mesoporous TiO<sub>2</sub> films used in the DSSC, the investigation of the electrostatic potential distribution in such a cell and a theoretical description of its working principle, so that the following questions were answered:

- What controls electron transport in mesoporous TiO<sub>2</sub> films?
- What is the electrostatic potential distribution in DSSCs?
- How does this electrostatic potential distribution affect the performance of such cells?
- What is the working principle of DSSCs?

Charge transport in the intercalated, nanocrystalline material is fundamentally different from that in single or polycrystalline bulk semiconductors. The charge is always

moving close to an interface, where electronic gap states are present. These can trap the charge carriers and thus slow down the transport significantly. Molecular modification was used as one tool to investigate the influence of the TiO<sub>2</sub> surface on solar cell performance and electron transport through the nanocrystalline TiO<sub>2</sub> network. Conductivity studies were conducted in quasi-steady state as well as time-resolved ones. Steady state measurements were used to study molecular effects on the conductivity while the time-resolved measurements were used to study fundamental aspects of electron transport inside mesoporous structures. Much emphasis was put on the analysis of time-resolved measurements. Such analysis required a numerical model that, in turn, revealed new insights into the analysis of such measurements.

The time-resolved transient technique was furthermore applied for the first time to investigate the electrostatic potential distribution in DSSCs. The measurements revealed important information about the relevance of the electrostatic potential distribution for DSSC performance and its working principle. Over the last years several models were proposed to explain DSSC operation, all based on a built-in electrostatic field. In this work measurements of the contact potential difference (CPD) of the various surfaces served to derive an energy band diagram for a given type of DSSC. The CPD data indicate that no built-in field is present in the dark. Thus a new model, based on electron tunneling, was derived to explain the operation of DSSCs and point out its working principle.

## 2 Theoretical Background

In this chapter the theoretical framework is introduced that is needed for the analysis and interpretation of the measurements presented in chapter 4. The first section discusses the general concepts of semiconductors and solar cells. This includes the introduction of the chemical, the electrostatic and the electrochemical potential, which are needed to describe charge transport and the general concept of solar cell operation. In section 2.2 the DSSC, as the most prominent example of a nano-composite solar cell, is introduced in detail and proposed models about its working principle are reviewed and summarized. The last section of this chapter discusses electron transport in the presence of electrostatic gap states which results in trapping/detrapping events and hopping. These mechanisms become dominant in the presence of a large number of trap states, which is the case in nanocrystalline, mesoporous TiO<sub>2</sub> films.

### 2.1 Working principle of solar cells

Solar cells, or more precisely, photovoltaic cells, are devices to convert sunlight into electrical energy. Until today the most commonly used devices are *p-n* junction cells based on silicon. The incident light generates electrons and holes which move towards the contacts of the solar cell, thus generating a photocurrent. Redistribution of charge between the contacts changes the electrostatic potential distribution across the solar cell which results in the built-up of a photovoltage.<sup>3</sup> In very general terms the working principle of solar cells can be generalized as follows:<sup>4</sup>

- a) Light interacts with the absorber of the solar cell where it excites electrons to the LUMO or conduction band in a semiconductor, leaving an electron vacancy in the HOMO, a hole in the case of a semiconductor. The energy of the light is converted into chemical potential energy of electrons and holes.
- b) Driving forces act on the charges so that the charges are separated in space and a current is generated.
- c) The direction of the current is defined by the boundary conditions, e.g. the selectivity of the contacts. One contact has to be transparent for electrons, while

positive charges are blocked, while the other contact should be selective for the collection of the positive charge and electron injection into the contact should be suppressed.

- d) To generate a photovoltage the chemical potential difference between electrons and holes has to be converted into an electrostatic potential difference, which occurs by charge redistribution.

In *p-n* junction solar cells parts of the absorber material create the junction so that steps a), b) and d), as well as part of step c) take place in the junction region. The light is absorbed in or close to the junction, and current flows in the direction dictated by the electrostatic field which also imparts some kind of selectivity because it spatially separates electrons and holes. The photovoltage is mainly generated in the junction region because only there photoexcitation causes significant deviations from equilibrium net charge density (because of changes in minority carrier densities due to photogeneration).<sup>5</sup>

In devices like DSSCs steps a) to d) take place in different parts of the cell, which is what has led to a controversy in the literature about the working principle of such cells.<sup>6-15</sup> In the following the driving forces for the photocurrent, the origin of the charge redistribution and the limit of the photovoltage are discussed in general terms. The conclusion will then be applied to DSSCs.

### 2.1.1 Potentials and quasi-Fermi levels

A general semiconductor structure with a varying electron affinity ( $\chi$ ), band gap ( $E_g$ ) and electrostatic potential ( $\varphi$ ) is shown Figure 2.1 and one can think of a semiconductor alloy with a composition that changes gradually in space. The energy level of the bottom of the conduction band ( $E_{CB}$ ) and the top of the valence band ( $E_{VB}$ ), the Fermi level ( $E_F$ ) as well as the local vacuum level ( $E_{loc}$ ) are measured with respect to a reference energy level ( $E_{ref}$ ). Surface physicists usually take the vacuum level at infinity as a reference level while electrochemists use the potential of the normal hydrogen electrode. The energies are depicted as arrows and the direction of the arrow indicates

if the energy is taken as negative (arrow direction down) or positive (arrow direction up). The chemical potential ( $\mu$ ) and the electron affinity are measured with respect to  $E_{loc}$ . The electron and hole densities deviate from their thermal equilibrium value if the semiconductor is illuminated. In thermal equilibrium the chemical potential for electrons ( $\mu_n$ ) is identical with the chemical potential for holes ( $\mu_p$ ), while it splits off into separate (non-equilibrium) potentials upon illumination, as shown in Figure 2.1b.

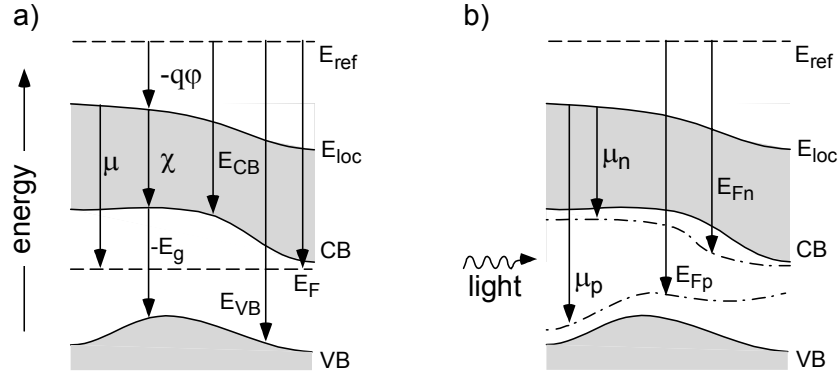


Figure 2.1: (a) Energy band diagram in thermal equilibrium of a semiconductor alloy with spatially varying electron affinity, band gap and built-in electrostatic field. The arrows show the chemical potential ( $\mu$ ), the electrostatic potential ( $\phi$ ), the electron affinity ( $\chi$ ), the band gap ( $E_g$ ) and the energy levels of the band edges of the conduction and valence bands ( $E_{CB}$  and  $E_{VB}$ ). (b) Upon illumination the chemical potentials for electrons and holes ( $\mu_n$  and  $\mu_p$ ) change. Their splitting corresponds to the quasi-Fermi level splitting ( $E_{Fn}$  and  $E_{Fp}$ ).

In a semiconductor without electronic states in the energy gap, the chemical potentials depend on the concentration of electrons ( $n$ ) in the conduction band (CB) and holes ( $p$ ) in the valence band (VB) and are defined as

$$\mu_n = \chi + k_B T \ln(n/N_{CB}) \quad \text{and} \quad \mu_p = \chi - E_g - k_B T \ln(p/N_{VB}) \quad (2.1)$$

if the energy difference between the chemical potential and the band edge is several times the thermal energy ( $k_B T$ ).  $N_{CB}$  and  $N_{VB}$  are the effective densities of electronic states at the bottom of the CB and top of the VB, respectively, which are defined as

$$N_{CB} = 2 \left( \frac{2\pi m_e^* k_B T}{h^2} \right)^{3/2} \quad \text{and} \quad N_{VB} = 2 \left( \frac{2\pi m_h^* k_B T}{h^2} \right)^{3/2} \quad (2.2)$$

where  $h$  is Planck's constant and  $m_e^*$  and  $m_h^*$  are the effective masses of electrons and holes at the respective band edges.

The relation between the chemical, the electrostatic and the electrochemical potentials (also denoted as the (quasi)-Fermi levels  $E_{Fn}$  and  $E_{Fp}$ ) can easily be derived from Figure 2.1 by adding the arrows, which yields

$$E_{Fn} = \mu_n - q\varphi \quad \text{and} \quad E_{Fp} = \mu_p - q\varphi \quad (2.3)$$

where  $q$  is the elementary charge. Similar relations can be found for the energies of the band edges

$$E_{CB} = \chi - q\varphi \quad \text{and} \quad E_{VB} = \chi - E_g - q\varphi \quad (2.4)$$

Combining eqns. (2.1), (2.3) and (2.4) gives for the electrochemical potentials for electrons ( $E_{Fn}$ ) and holes ( $E_{Fp}$ ):

$$E_{Fn} = E_{CB} + k_B T \ln(n/N_{CB}) \quad \text{and} \quad E_{Fp} = E_{VB} - k_B T \ln(p/N_{VB}) \quad (2.5)$$

The light-induced splitting of  $E_F$  into its quasi-Fermi levels is due to a change in density of electrons and holes and, thus, a change in the chemical potential of CB electrons and VB holes ( $\mu_n$  and  $\mu_p$ ).

For practical use the output voltage is the relevant parameter, which is the electrostatic potential difference between the contacts of the solar cell. Therefore the efficiency of photovoltaic cells depends, among other things, on how well the chemical potential difference ( $\mu_n - \mu_p$ ) can be transformed into an electrostatic potential difference. In energy band diagrams the changes in the electrostatic potential are shown as changes in the local vacuum level, as well as in conduction and valence bands (for the latter they come on top of any changes in electron affinity). The electrostatic field is shown by a gradient in  $E_{loc}$ . Charge reorganization upon illumination is responsible for the

generation of a photovoltage. The driving forces for current flow and subsequent charge reorganization are the subject of the following section.

### 2.1.2 Driving forces for electron and hole currents

To make a solar cell work the light-generated electrons and holes have to reach and be collected at the contacts. The driving force for an electron or hole current density is defined by the gradient of the relevant quasi-Fermi level

$$\vec{J}_e = n\eta_e \vec{\nabla} E_{Fn} \quad \text{and} \quad \vec{J}_h = p\eta_h \vec{\nabla} E_{Fp} \quad (2.6)$$

where  $\eta_e$  and  $\eta_h$  are the electron and hole mobilities in the CB and VB, respectively. The partial currents can be written more explicitly when equations (2.4) and (2.5) are substituted into equation (2.6) so that

$$\vec{J}_e = n\eta_e \left( q\vec{\nabla}\phi + \vec{\nabla}\chi - k_B T \vec{\nabla} \ln N_{CB} \right) + qD_e \vec{\nabla} n \quad (2.7a)$$

$$\vec{J}_h = -p\eta_h \left( q\vec{\nabla}\phi + \vec{\nabla}\chi + \vec{\nabla}E_g - k_B T \vec{\nabla} \ln N_{VB} \right) + qD_h \vec{\nabla} p \quad (2.7b)$$

The first term describes the drift current, caused by an electrostatic field while the last term is the diffusion current (where I used the Einstein relations,  $\eta_e k_B T = qD_e$  and  $\eta_h k_B T = qD_h$ ). An additional driving force is provided by a gradient or a discontinuity in the electron affinity. This term is often overlooked when driving forces for electrons and holes are discussed. In section 2.2.3 and 4.6 it will be shown that this term is essential to explain the working principle of DSSCs. The last term in the brackets is due to a gradient in the effective density of electronic states close to the band edges. Equation 2.7b furthermore contains a term which depends on a possible gradient of the electronic gap.

In *p-n* junction solar cells the major driving force is due to the built-in field and other driving forces are often not considered. For DSSCs and ETA solar cells one has to consider all driving forces in order to understand the limitations of such cells, which will be discussed in detail in section 2.2.

### 2.1.3 Contact selectivity

The interface between the semiconductor and the metal electrodes, which are needed to make electrical contact to the cell, is of particular importance for cell operation. Contact recombination needs to be minimized in a well-performing cell, which can be achieved by an interface design that makes the contacts selective. Figure 2.2a shows a  $p$ - $n$  junction solar cell between contacts  $A$  and  $B$ . Light, incident from the left side, generates electrons and holes in a  $p$ -doped part of the cell.  $E_{Fn}$  is strongly shifted towards to the CB edge while  $E_{Fp}$  is not significantly shifted. From the figure we see that light-generated electrons can not only diffuse into the electrostatic field in the  $p$ - $n$  junction but can also diffuse into contact A and thus give rise to a high contact recombination. Possible designs to achieve contact selectivity are shown in Figure 2.2b & c and more of them can be found in the literature.<sup>3</sup> The first design makes use of a thin semiconductor layer with a smaller electron affinity than the absorber so that a barrier for electron transfer is created while hole transfer remains unblocked. Another possibility is to increase the  $p$ -type doping density close to the contact drastically (Figure 2.2c) so that the  $E_{Fp}$  shifts into the VB. This causes some interface band bending close to the contact A, which is beneficial for hole collection while the electron current towards the contact is decreased.

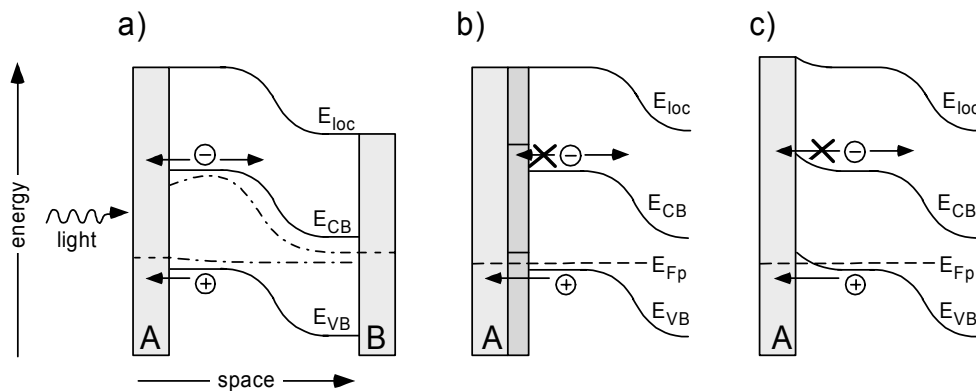


Figure 2.2: (a) Energy band diagram for a  $p$ - $n$  junction cell upon illumination. The contact at the illuminated side is not selective so that also the light-generated electrons are collected at the contact. This causes high contact recombination. (b) A thin, lower electron affinity layer (with similar or smaller bandgap) will create a barrier for electrons and can be used to achieve contact selectivity. (c) Heavy  $p$ -type doping close to the interface is another possibility to achieve selectivity.

Selectivity at the interface with contact B is not crucial as long as most of the light is absorbed in the  $p$ -type side so that the minority carrier density close to contact B is negligible. In this case the electrostatic field at the  $p$ - $n$  junction suffices to block a hole-current towards the  $n$ -type material and only light-generated electrons can reach the interface with contact B.

Different systems like semiconductor/electrolyte interfaces can be intrinsically selective due to different rate constants for electron or hole injection into the electrolyte. It was shown in the literature that the polarity of the photocurrent of a CdS or CdSe quantum dot photo-electrode can be inverted when the electrolyte composition is changed so that the interface kinetics are affected.<sup>16</sup> Interface kinetics also play an important role for DSSC operation because a difference in the rate constants is required to achieve high cell efficiencies. This issue will be explained in more detail in section 2.2.1.

Selective charge collection at the contact as well as charge redistribution in the  $p$ - $n$  junction or in the contacts is responsible for the build-up of a photovoltage. The components that contribute to a photovoltage as well as the theoretical limit of the open circuit voltage are discussed in the next section.

#### 2.1.4 The open circuit voltage

The photovoltage of a solar cell can in general be calculated from the change in the electric field upon illumination

$$V_{PV} = \int_A^B (\vec{E} - \vec{E}_0) \cdot d\vec{l} \quad (2.8)$$

where  $\vec{E}$  is the electrostatic field upon illumination and  $\vec{E}_0$  is the field in thermal equilibrium. The integration has to be made from the front contact  $A$  to the back contact  $B$  along a continuous path  $l$ , which is shown in Figure 2.3 for a generalized band structure with varying electron affinity and band gap.

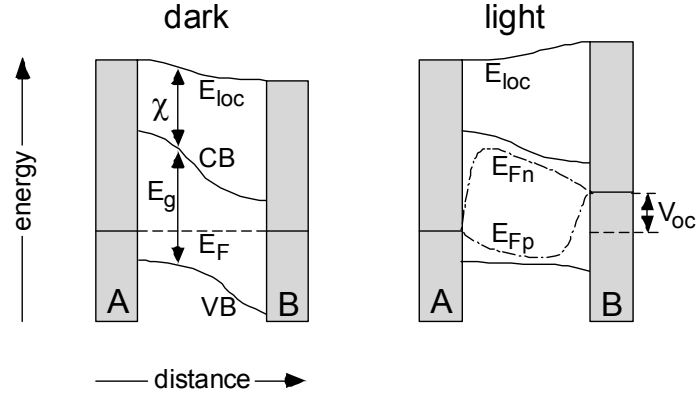


Figure 2.3: Energy band diagram of a semiconductor alloy which acts as an absorber material. The absorber has varying electron affinity,  $\chi$  and band gap,  $E_g$ , and is contacted, in a sandwich configuration, by two metal electrodes A and B. Upon illumination the Fermi level splits into the quasi-Fermi levels of electrons and holes ( $E_{Fn}$  and  $E_{Fp}$ ). The charge redistribution that accompanies this process changes the local vacuum level.

The open circuit voltage ( $V_{oc}$ ) of solar cells can be calculated from eqs. (2.7) and (2.8) with as boundary condition that the total current at  $V_{oc}$  is zero. A detailed derivation can be found in ref. 17, so that only the final result is given here

$$V_{oc} = - \int_A^B \left( \frac{q\eta_e \Delta n + q\eta_h \Delta p}{\sigma} \right) \vec{E}_0 \cdot d\vec{l} \quad (2.9a)$$

$$+ \int_A^B \left( \frac{q\eta_e \Delta n}{\sigma} \right) \vec{\nabla} \chi \cdot d\vec{l} + \int_A^B \left( \frac{q\eta_h \Delta p}{\sigma} \right) \vec{\nabla} (\chi + E_g) \cdot d\vec{l} \quad (2.9b)$$

$$- k_B T \int_A^B \left( \frac{q\eta_e \Delta n}{\sigma} \vec{\nabla} \ln N_{CB} - \frac{q\eta_h \Delta p}{\sigma} \vec{\nabla} \ln N_{VB} \right) \cdot d\vec{l} \quad (2.9c)$$

$$+ k_B T \int_A^B \left( \frac{q\eta_e}{\sigma} \vec{\nabla} (\Delta n) - \frac{q\eta_h}{\sigma} \vec{\nabla} (\Delta p) \right) \cdot d\vec{l} \quad (2.9d)$$

The light-generated excess densities of electrons and holes are given by  $\Delta n = n - n_0$  and  $\Delta p = p - p_0$ , respectively. The conductivity is denoted as  $\sigma$ . Term (2.9a) originates from an electrostatic built-in field, which is usually the largest contributor to the  $V_{oc}$  in  $p$ - $n$  junction solar cells. The contribution to the  $V_{oc}$  from a gradient or discontinuity in the electron affinity is described by the first term in (2.9b) while the second term describes the contribution to the  $V_{oc}$  from a VB gradient that is not caused by an electrostatic field (e.g. a change in ionization potential). A gradual change in the density of electronic states can give a contribution to  $V_{oc}$  as described by (2.9c).

Additionally, a difference in the electron and hole concentration gradient combined with a difference in the mobilities at high photogenerated carrier densities (2.9d) can give a contribution to  $V_{oc}$ , which is also known as the Dember potential. The latter two terms are in the order of  $k_B T$  and thus often of minor importance.

### 2.1.5 Solar cells without electrostatic built-in field

The working principle of solar cells without a  $p-n$  junction is often not obvious. In many cases drift currents, caused by an electric field, and diffusion currents, caused by a concentration gradient are the only considered current contributions. Band discontinuities and gradients in the density of electronic states in the CB or VB are often overlooked as an additional driving force. In a thought experiment it will be shown that a solar cell with a gradient in the electron affinity  $\chi$  can give the same  $V_{oc}$  as a cell with an electric built-in field.

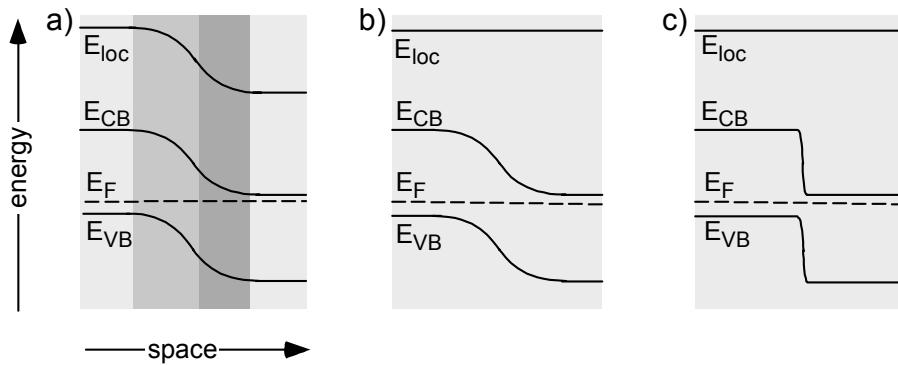


Figure 2.4: (a) Band structure of a  $p-n$  homojunction cell with an electrostatic built-in potential shown by bending of the CB and VB. (b) The same band bending can be achieved by a gradient in the electron affinity. (c) The band bending can also occur on a very narrow scale so that the theoretical derivation includes band 'discontinuities' at phase boundaries.

Figure 2.4a shows the band diagram for a conventional  $p-n$  homojunction cell with a built-in potential  $\phi_{bi}$ . Figure 2.4b shows a solar cell without built-in electrostatic field (which can be seen from the constant  $E_{loc}$ ) but with band bending due to a gradient in the electron affinity. Such a device can theoretically be produced by two semiconducting materials with the same band gap but with a different electron affinity and a different doping type. The region of band bending can be established if the two

materials form an alloy and the mixing ratio is gradually changed from the pure p-type to the pure n-type material. From eq. (2.9a) and (2.9b) one can see that both devices (Figure 2.4a & b) give the same  $V_{oc}$ . This requires of course that the electron and hole mobilities, as well as the effective density of electronic states at the band edges,  $N_{VB}$  and  $N_{CB}$ , are identical in the two materials forming the alloy.

While gradients in the electron affinity over a macroscopic region in the device are rather uncommon, they play an important role at phase boundaries. Two materials with a different electron affinity, in electronic contact with each other, show a discontinuity in the CB. On a microscopic scale such a ‘discontinuity’ is still continuous and can be described by a gradient, which is schematically depicted in Figure 2.4c. The same holds for a discontinuity in the VB, caused by a difference in the ionization potentials (sum of electron affinity and band gap). Both, a CB and VB discontinuity, can contribute significantly to the  $V_{oc}$  of a solar cell and in the following I will show that a CB discontinuity at the  $\text{TiO}_2$ /conducting substrate interface is essential for the operation of a DSSC.

### 2.1.6 Solar cell characteristics

The efficiency of solar cells depends on the open circuit voltage ( $V_{oc}$ ), the short circuit current density ( $J_{sc}$ ) and the fill factor (FF), which is defined as

$$FF = \frac{J_{mpp} V_{mpp}}{J_{sc} V_{oc}} \quad (2.10)$$

The current density at the maximum power point of the cell is denoted by  $J_{mpp}$ ;  $V_{mpp}$  is the photovoltage at maximum power point. An efficient solar cell is characterized by a high  $V_{oc}$ ,  $J_{sc}$  as well as a high fill factor. A low fill factor indicates a lower efficiency of the cell, even though  $J_{sc}$  and  $V_{oc}$  might be high.

## 2.2 The dye-sensitized solar cell

Dye-sensitized solar cells are a promising, potentially low cost alternative to conventional  $p$ - $n$  junction solar cells. DSSCs are based on a mesoporous, nanocrystalline film of a wide band gap semiconductor (usually  $\text{TiO}_2$ ), sintered onto a transparent conductive oxide electrode (mostly F-doped  $\text{SnO}_2$ , FTO). The diameter of single  $\text{TiO}_2$  particles is typically around 20 – 25 nm while the film thickness of the porous network is usually around 10  $\mu\text{m}$ . A monolayer of dye molecules is adsorbed to the surface of the  $\text{TiO}_2$  particles and the pores of the film are filled with an  $\text{I}^- / \text{I}_3^-$  redox electrolyte to close the electrical circuit via a Pt (counter) electrode. Upon illumination electrons are injected by the photo-excited dye into the semiconductor and collected at the FTO substrate, as shown in Figure 2.5. The electrolyte reduces the oxidized dye and transports the positive charge to the Pt electrode.<sup>1</sup> While in the laboratory such systems can reach solar to electric conversion efficiencies up to 11%,<sup>2,18</sup> they are not yet manufactured on a large scale, mainly due to technical problems like sealing. Solid-state devices, in which the liquid electrolyte is replaced by a solid-state hole conductor, including ETA cells, are a promising alternative, but their efficiency ( $\sim 4\%$ ) is still significantly below that of the liquid electrolyte cells.<sup>19-21</sup>

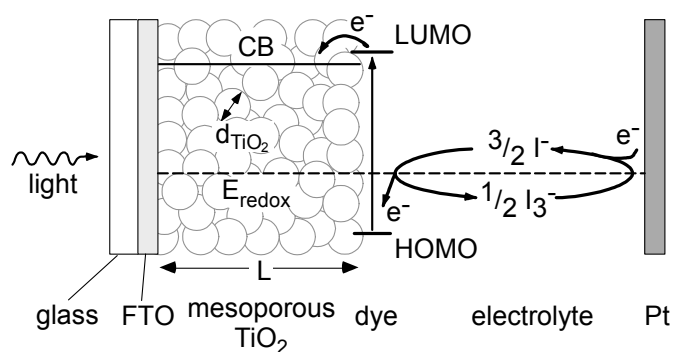


Figure 2.5: Schematic drawing of a DSSC with superimposed on it the electron energy levels of the  $\text{TiO}_2$  CB and of the dye, as well as the redox potential of the electrolyte, on the same energy scale. The light is incident from the FTO-covered glass substrate. Upon excitation of the dye, electrons are promoted from the HOMO to the LUMO level. From the LUMO level electrons are injected into the  $\text{TiO}_2$  CB. The dye cation is recharged by the electrolyte and the positive charge is transferred to the electrolyte in the form of the  $\text{I}_3^-$  ions. These diffuse to the Pt electrode while electrons diffuse towards the FTO substrate. The  $\text{TiO}_2$  particle diameter  $d_{\text{TiO}_2}$  is usually 20 - 25 nm and the film thickness  $L$  is typically  $\sim 10 \mu\text{m}$ .

Further improvement of liquid and solid-state DSSCs requires an understanding of the electric and chemical potential distributions in the dark and upon illumination.<sup>22-24</sup> Initially it was accepted that the  $V_{oc}$  of DSSCs is limited by the energy difference between the bottom of the TiO<sub>2</sub> conduction band and the redox potential ( $E_{redox}$ ) of the electrolyte (the so-called kinetic model). Some years ago it was proposed that the  $V_{oc}$  is limited by a built-in electric field at the TiO<sub>2</sub>/FTO interface and that such a field is essential for the operation of DSSCs (the so-called junction model).<sup>6</sup> Subsequently, it was suggested that one can merge both models, so that a built-in potential does not necessarily limit the  $V_{oc}$ <sup>25,26</sup> but might have a strong effect on the fill factor,<sup>9,26</sup> which has a strong impact on the cell efficiency.

It appears that what happens at the FTO/TiO<sub>2</sub> interface is the origin of disagreements about the working principle of DSSCs. In the following, existing models are briefly reviewed with emphasis on their (dis)agreements, especially regarding the FTO/TiO<sub>2</sub> interface. Two types of DSSCs will be distinguished, one that consists of the mesoporous TiO<sub>2</sub> film which is directly sintered onto the FTO substrate. The other consists of an additional dense, compact TiO<sub>2</sub> layer, with a width of some tens of nanometers. The compact layer is often used to avoid direct contact between the electrolyte and the conductive substrate and suppress recombination from the FTO substrate. While this compact layer does not improve the performance of liquid electrolyte DSSCs, it is obligatory in solid state DSSCs which apparently do not show any significant conversion efficiency without it.

### 2.2.1 The kinetic model

In DSSCs electrons are injected, upon illumination with photon energies larger than the dye's HOMO-LUMO gap, from the excited dye state into the CB of the TiO<sub>2</sub>. While electron injection is a very fast process (on the femtosecond scale),<sup>27</sup> the reduction of the oxidized dye by the redox electrolyte's I<sup>-</sup> ions occurs in about 10<sup>-8</sup> seconds.<sup>28</sup> Recombination of photo-injected CB electrons with oxidized dye molecules or with the oxidized form of the electrolyte redox couple (I<sub>3</sub><sup>-</sup> ions) occurs in microseconds,<sup>28</sup> and, thus, is orders of magnitude slower than the injection and recharging process of the

dye. The high efficiency of charge separation at the  $\text{TiO}_2/\text{dye}/\text{electrolyte}$  interface is explained by the huge difference in these rate constants, for electron and hole injection into the  $\text{TiO}_2$  CB and redox electrolyte, respectively, on the one hand, and for recombination of CB electrons with oxidized dye molecules or  $\text{I}_3^-$  ions, on the other hand. These are kinetic parameters, which is the origin of the models' name.

The upper limit for  $V_{oc}$  in the kinetic model is given by the energy difference between the bottom of the  $\text{TiO}_2$  CB and the redox potential of the  $\text{I}^- / \text{I}_3^-$  couple.<sup>8</sup> The photogenerated increase of electron density in the  $\text{TiO}_2$  network causes a shift of the electron's quasi-Fermi level,  $E_{Fn}$ , towards the CB of the  $\text{TiO}_2$  (Figure 2.6). At the same time the redox potential remains nearly unchanged due to the high concentration of redox species<sup>a</sup> and, thus, will be taken as a reference potential. The energy difference between  $E_{Fn}$  at the FTO contact and  $E_{redox}$  corresponds to the photovoltage of DSSCs and the electron current in the mesoporous structure is driven by a gradient in  $E_{Fn}$ . A photo-induced increase of the electron density inside the mesoporous  $\text{TiO}_2$  structure shifts the chemical potential towards the CB. Additionally, the  $\text{TiO}_2$  energy bands can shift towards the vacuum level due to a change of the electrostatic potential difference between the  $\text{TiO}_2$  and the electrolyte.<sup>29</sup> Thus, a shift of  $E_{Fn}$  can be caused by a shift of  $\mu$  and/or of  $\varphi$ . In section 4.6.2 it will be shown that a change of the electrostatic potential at the  $\text{TiO}_2/\text{electrolyte}$  interface, (e.g., uniform or non-uniform band edge movement) is 2-3 orders of magnitude smaller than the chemical potential shift inside the  $\text{TiO}_2$ , even if there are only a few photo-injected electrons per particle.<sup>30,31</sup> Therefore band edge movement is usually neglected which is consistent with experimental observations.<sup>32</sup>

---

<sup>a</sup> The concentrations normally used in DSSCs are about 0.5 M LiI and 0.05 M  $\text{I}_2$ , which translates into  $\sim 3 \cdot 10^{20}$  and  $\sim 3 \cdot 10^{19}$  redox species/ $\text{cm}^3$ , respectively. Under steady state operation there is about one mobile electron /  $\text{TiO}_2$  particle. This yields around  $10^{18}$  electrons/ $\text{cm}^3$  for commonly used  $\text{TiO}_2$  particles with a diameter of approximately 20 nm and a film porosity of 50%.

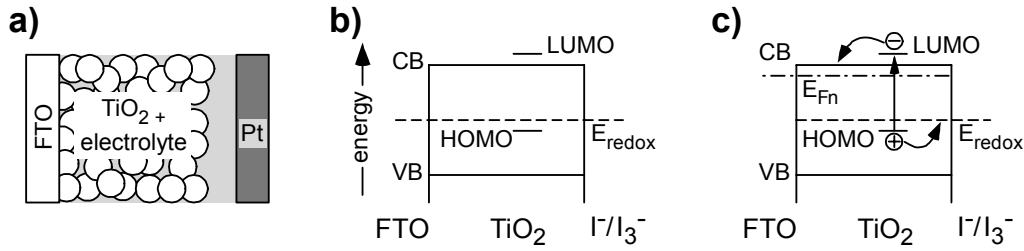


Figure 2.6: (a) Schematic drawing of a DSSC without compact TiO<sub>2</sub> underlayer. (b) Energy band diagram at thermal equilibrium. (c) Energy band diagram upon illumination at open circuit voltage.

An analytical solution to describe the current-voltage behaviour was presented, assuming a perfectly ohmic contact at the FTO/TiO<sub>2</sub> interface.<sup>33</sup> This means that the chemical potential of the electrons inside the TiO<sub>2</sub> is converted into an electrical potential at the FTO contact without any loss of potential. The kinetic model usually does not discuss explicitly the electrostatic potential distribution, whether in the dark or under illumination ( $E_{loc}$  is usually not depicted in energy band diagrams; see e.g. Figure 2.6b & c), but was explicitly addressed by the junction model.<sup>6</sup>

## 2.2.2 The junction model

The junction model is based on an electrostatic approach, in contrast to the kinetic model, which deals mostly with chemical potentials. While both models agree that no electric field is present in most of the TiO<sub>2</sub> film, so that  $E_{CB}$  remains constant, the junction model states that a built-in electric field exists in the dark at the FTO/TiO<sub>2</sub> interface. According to the model this field is essential for the operation of DSSCs and sets an upper limit to the maximum attainable  $V_{oc}$ .<sup>6</sup> While in conventional  $p-n$  junction solar cells space charge regions in the cell cause the built-in field, in the case of DSSCs the origin of such a built-in field has to be different. It is caused by a difference between the FTO work function and the redox potential of the electrolyte. Once both materials are brought into contact, there will be an electrostatic potential drop over a Helmholtz layer at the FTO/electrolyte interface. Due to the low number of mobile charge carriers and the small particle dimensions, the TiO<sub>2</sub> network is incapable to screen the electric field between the FTO substrate and the electrolyte. A simplified geometry was used to calculate the electrostatic potential distribution inside the

TiO<sub>2</sub>,<sup>25,34</sup> where the mesoporous TiO<sub>2</sub> film was approximated by TiO<sub>2</sub> cylinders, oriented normal to the FTO substrate, with a diameter equivalent to the particle diameter  $d$  and a length equivalent to the film thickness  $L$  (Figure 2.7a). Ferber *et al* solved the Poisson equation for the 2-dimensional projection of such a simplified geometry, while Bisquert *et al* solved the Laplace equation inside the rod, assuming that the density of mobile electrons inside the TiO<sub>2</sub> structure is negligible. Both calculations led to a similar result, namely that nearly all of the electrostatic potential drops close to the FTO substrate. Energy band diagrams in the dark and upon illumination are shown in Figure 2.7b and c, respectively.

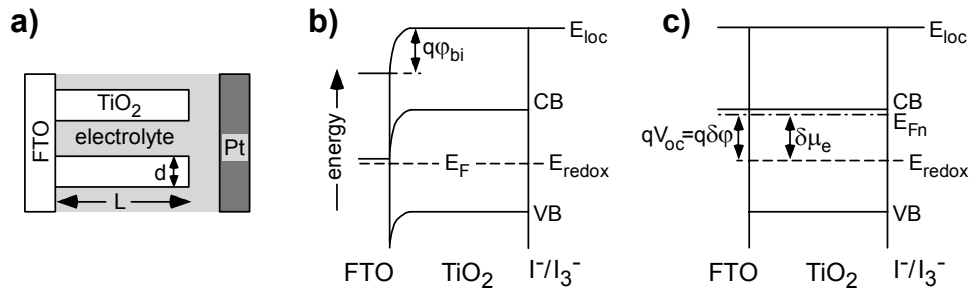


Figure 2.7: (a) Schematic drawing of the simplified DSSC structure where the TiO<sub>2</sub> film is approximated by cylinders of length  $L$  and diameter  $d$ . (b) Energy band diagram in the dark with a built-in potential  $\phi_{bi}$  at the FTO/TiO<sub>2</sub> interface. (c) Upon illumination the built-in field is neutralized due to a chemical potential shift  $\delta\mu_e$  in the TiO<sub>2</sub>. This shift is converted into an electrostatic potential shift ( $\delta\phi$ ) in the FTO substrate.

It should be emphasized that the electrostatic (built-in) field at the TiO<sub>2</sub>/FTO interface is caused by the properties of the surrounding materials (redox potential of the electrolyte and work function of the FTO substrate) and that the junction model states that the  $V_{oc}$  is limited by the magnitude of that built-in electric field. A problem of the junction model is the lack of experimental evidence for the postulated correlation between  $V_{oc}$  and the energy difference between the substrate work function and the redox potential. Measurements of the  $V_{oc}$  on systems, where the FTO was replaced by other conducting substrates with different work functions did not show the predicted effect on the  $V_{oc}$ . In contrast the  $V_{oc}$  seemed to be nearly independent on the work function of the substrate.<sup>7,9</sup>

### 2.2.3 The thermionic emission model

A numerical model for DSSCs<sup>25</sup> as well as calculations based on an equivalent circuit<sup>9,26</sup> showed that a built-in field does not necessarily limit the  $V_{oc}$ , if thermionic emission at the FTO/TiO<sub>2</sub> interface is taken into account. In the following this approach will be denoted as the thermionic emission model. The thermionic emission model assumes that the built-in potential is around 600 mV, such that a Schottky barrier of about 150 mV is present at  $V_{oc} = 750$  mV. This model was presented for a DSSC with a compact TiO<sub>2</sub> underlayer between the conductive substrate and the mesoporous network, as is schematically shown in Figure 2.8a. A band diagram with a built-in field and a discontinuity in the CB at the FTO/TiO<sub>2</sub> interface (due to a difference in the electron affinity  $\chi$  of the FTO and the TiO<sub>2</sub>) is depicted in Figure 2.8b, c & d.

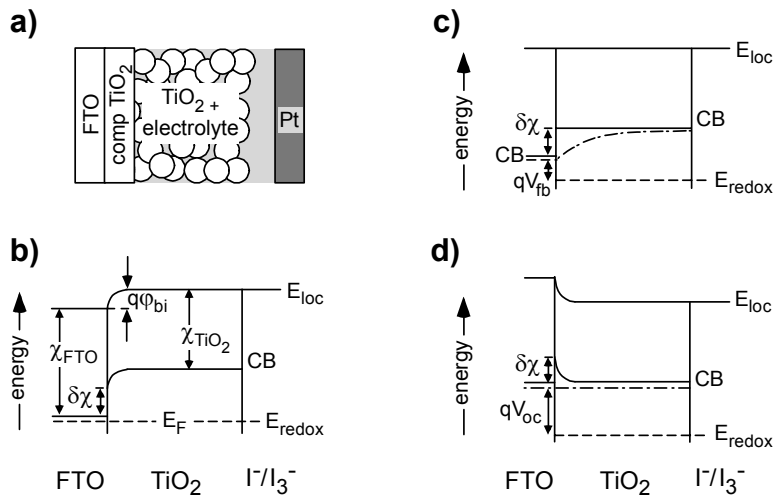


Figure 2.8: (a) Schematic drawing of a DSSC with a compact TiO<sub>2</sub> layer between the mesoporous film and the FTO substrate. (b) Energy band diagram in the dark which includes a built-in potential,  $\phi_{bi}$  and a CB discontinuity  $\delta\chi$ . (c) as (b) at the flat band voltage  $V_{fb}$ . (d) At open circuit voltage including the Schottky barrier at the FTO/TiO<sub>2</sub> interface.

Figure 2.8b shows the situation in the dark ( $E_F = E_{redox}$ ), while the band alignment at the intermediate photovoltage, smaller than  $V_{oc}$ , at which the built-in field is cancelled by the photovoltage so that the bands are flat (flat band voltage,  $V_{fb}$ ), is shown in Figure 2.8c. Electron current into the FTO electrode continues at applied voltages higher than  $V_{fb}$ , is due to thermionic emission over the electrostatic barrier at the TiO<sub>2</sub>/FTO interface, as depicted in Figure 2.8d which shows the situation at open circuit. The

photovoltage beyond  $V_{fb}$  is due to the CB discontinuity and the maximum photovoltage that can be achieved is limited by the energy difference between the bottom of the  $\text{TiO}_2$  CB (at the interface with the electrolyte) and the redox potential, just as in the kinetic model.

$I$ - $V$  characteristics of DSSCs were analyzed with the simple equivalent circuit depicted in Figure 2.9, assuming that there is a Schottky barrier at the FTO/ $\text{TiO}_2$  interface.<sup>9,26</sup> The photocurrent was represented by a current source ( $J_G$ ), and recombination of photo-generated electrons with ions from the electrolyte or oxidized species of the dye was described by a regular diode equation ( $J_R$ ). A resistor,  $R_S$ , was connected in series to account for transport losses in the electrolyte. The potentials applied to the building blocks of the equivalent circuit are electrochemical ones and not entirely electrical. They are explicitly labelled in Figure 2.9a in units of volts. The potential difference applied to the diode, which represents recombination, is a pure chemical potential difference ( $E_{Fn} - E_{redox}$ ), while the potential difference which generates a current  $J_b$  across the FTO/ $\text{TiO}_2$  interface barrier is due to a difference in the electrostatic potential applied from the FTO side and the chemical potential, applied from the  $\text{TiO}_2$  side. Thus the FTO/ $\text{TiO}_2$  junction can be regarded as a chemical to electrical potential converter, which is schematically shown in Figure 2.9b.<sup>35</sup>

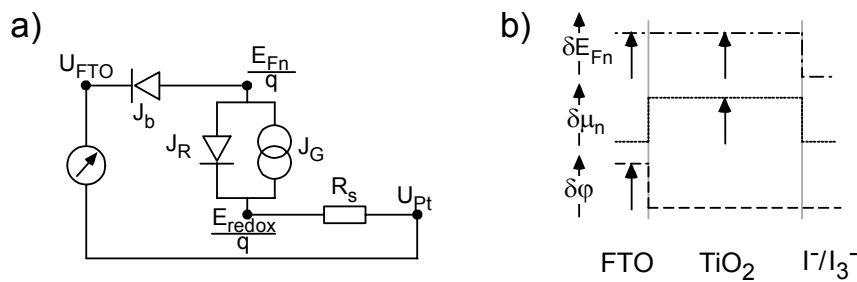


Figure 2.9: (a) Simple equivalent circuit for a DSSC that includes a barrier ( $J_b$ ) at the FTO/ $\text{TiO}_2$  interface. The generation and recombination currents are labelled as  $J_G$  and  $J_R$ , while  $R_S$  represents transport losses in the electrolyte. The potentials applied to the components are explicitly labelled at the nodes of the circuit. (b) Schematic drawing of the light-induced chemical potential shift ( $\delta\mu_n$ ), of the electrostatic potential shift ( $\delta\phi$ ) and of the shift of the electron quasi Fermi level ( $\delta E_{Fn}$ ) in the DSSC. Each potential diagram is drawn with respect to a separate reference level.

At  $V_{oc}$  the electron quasi Fermi level,  $E_{Fn}$ , shifts upwards in the  $\text{TiO}_2$  and in the FTO substrate. This is due to a strong chemical potential shift inside the  $\text{TiO}_2$  and an electrostatic potential change in the FTO. These shifts are much larger, usually, than any chemical potential shift in the FTO and electrostatic potential change in the  $\text{TiO}_2$ . Therefore, they are neglected in Figure 2.9b.

Calculations showed<sup>26</sup> that the influence of the Schottky barrier on the  $I$ - $V$  characteristics is negligible for barrier heights  $<0.5$  eV (taking a Richardson constant of  $670 \text{ A cm}^{-2} \text{ K}^{-2}$ ). For higher barrier heights the  $I$ - $V$  curves showed some S-shape and the fill factor decreased significantly, while  $V_{oc}$  remained constant. These calculations were supported by experiments where the Schottky barrier height at the conducting substrate/ $\text{TiO}_2$  interface was systematically changed.<sup>9</sup>

The problem of this type of equivalent circuit-based analysis that includes a Schottky barrier is that it cannot model the dark  $I$ - $V$  characteristics correctly with physically reasonable parameters. Built-in voltages of several hundreds of mV are required for a good fit with measured data. In section 4.6.1 experimental data will be presented which indicate that no built-in field is present at this interface. In contrast it seems that an electrostatic barrier is present in the dark, which increases if a photovoltage develops. Because of this I developed a new model, based on electron tunnelling through a barrier at the FTO/ $\text{TiO}_2$  interface, which I will introduce in section 4.6.

The working principle of a DSSC can be summarized in terms of the general solar cell working principle that was introduced at the beginning of this chapter:

- a) Light is absorbed by the dye and charge separation occurs at the  $\text{TiO}_2$ /dye/electrolyte interface.
- b) The driving force for the electron current is a concentration (= activity) gradient in the  $\text{TiO}_2$  particles. Positive charges in the electrolyte move due to a concentration gradient of the oxidized species ( $\text{I}_3^-$ ). Thus, in both cases current is due to diffusion.

- c) The direction of the diffusion currents is defined by the selectivity of the contacts which set the boundary conditions for the currents. Electron injection from the  $\text{TiO}_2$  into the FTO is kinetically favoured over electron injection into the electrolyte is a much slower process. Furthermore, positive charges from the electrolyte are efficiently transferred to the Pt counter electrode while charge transfer from the electrolyte into the FTO electrode is kinetically blocked.
- d) Electron injection into the  $\text{TiO}_2$  particles increases the electron density and shifts the chemical potential towards the CB. The chemical potential of the electrons is converted into an electrostatic potential shift due to charge accumulation in the FTO substrate (in the Helmholtz layer at the FTO/electrolyte interface).

One can see that the working principle of DSSCs is quite different from that of conventional  $p$ - $n$  junction solar cells, where almost all steps occur at the  $p$ - $n$  junction. In DSSCs, for example step a) occurs at a different interface than does step d).

In summary I have shown that the FTO/ $\text{TiO}_2$  interface plays a fundamental role in the understanding of DSSCs and detailed investigation of this interface is presented in sections 4.5 and 4.6.3.

The second fundamental difference between nano-composite and conventional  $p$ - $n$  junction solar cell is the charge transport. The electron conductor as well as the electrolyte or solid state hole conductor are mesoscopic structures which are intercalated with each other. Transport of electrons inside the  $\text{TiO}_2$  structure occurs always close to the hole conducting phase and the surface to volume ratio is orders of magnitude higher than for bulk material. At surfaces usually electronic gap states are present so that these materials consist of a rather high density of gap states which act as traps. Transport in the presence of traps is discussed in the following section.

## 2.3 Electron transport in mesoporous TiO<sub>2</sub> films

In section 2.1.2 it was shown that an electric field, a gradient in the electron affinity and band gap, a concentration gradient of electronic states or a concentration gradient of electrons and holes contribute to a gradient in  $E_{Fn}$  and  $E_{Fp}$ , which is the driving force for the respective electron or hole current. The current depends additionally on the electron and hole mobility. Electronic states in the energy gap often act as electron or hole acceptors and, thus, function as traps, which can slow down the mobility significantly. Electron transport is the relevant process in DSSCs so that the following sections consider the effect of electronic gap states on electrons rather than on hole transport.

### 2.3.1 Trapping/detrapping and hopping transport

Electrons in the TiO<sub>2</sub> CB can occupy energy acceptor levels which are present at the energy level  $E_t$  within the energy gap. These gap states are created at the crystal surface where the symmetry is broken and unsaturated (dangling) bonds are present. Furthermore they can be created by defects in the crystal lattice and by impurities. First electron transport is considered, based on trapping and detrapping events of quasi-free CB electrons. Trapping of electrons depends on the capture cross section of the specific trap states (which can be described by a rate constant  $k_{tr}$ ), the probability that this state is not already occupied and the concentration of CB electrons. The release of electrons from trap states is only possible if they have sufficient thermal energy to be excited into the CB. The dwell time in a trap state depends exponentially on the energy difference between the trap level and the bottom of the CB,  $E_t - E_{CB}$ .<sup>36</sup> Once an electron is thermally released from a trap state it moves in the CB band until it is trapped again, as is schematically depicted in Figure (2.10a). Often the dwell time in trap states is one to several orders of magnitude larger than the time the electron spends in an unbound state in the CB. Therefore it is often sufficient to consider the electron in its trapped states and to neglect the drift or diffusion time in the CB.

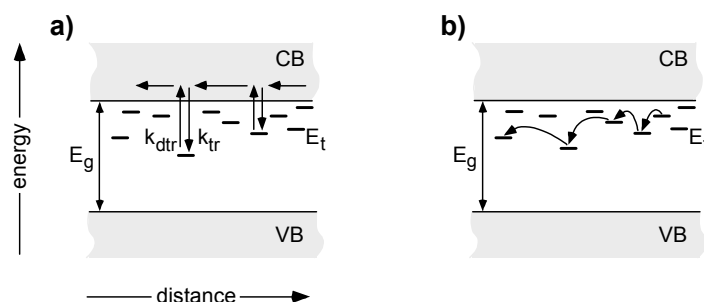


Figure 2.10: Energy band diagram of a semiconductor with electronic trap states (at energy levels  $E_t$ ) in the energy gap  $E_g$ . (a) Electron transport, governed by trapping and detrapping events, described by the rate constants  $k_{tr}$  and  $k_{dtr}$ , respectively. (b) Electron hopping from one trap state to the next. Trapped electrons tunnel directly between trap states in contrast to trapping/detrapping transport were electrons are thermally released into the CB.

When the electron concentration in the  $\text{TiO}_2$  is increased deeper traps are getting filled and electrons involved in the transport process are trapped and detrapped in shallow trap states. The dwell time in shallow traps is significantly shorter and the electrons transport becomes faster. This can be included into the equation for electron transport (eq. (2.7a)) by an electron density dependent electron mobility  $\eta_e(n)$  and diffusion coefficient  $D_e(n)$ , which describes dispersive transport.

Another transport mechanism that involves trap states is hopping. Thermal activation into the CB is not required for hopping transport, in contrast to trapping/detrapping. Hopping transport becomes significant when the density of trap states is high enough so that the spatial distance between trap states becomes short enough for electron tunnelling from one trap state to the neighbouring one. Figure 2.10b shows a scheme for electron hopping. The dwell time in trap states is significantly shorter if hopping is possible, due to the significantly lower energy, required for release from the trap state. Hopping transport is thought to be the dominant transport process in many organic semiconductors.<sup>37</sup>

### 2.3.2 Molecular modification of semiconductor surfaces

Molecular modification of semiconductor surfaces is a powerful tool to tune the electronic properties of semiconductor/semiconductor and semiconductor/metal junctions.<sup>38-47</sup> It has been shown that the  $I$ - $V$  characteristics of molecularly modified

Schottky junctions correlate well with the dipole moment of the molecules that are introduced.<sup>42,45,46</sup> Molecules adsorbed to a semiconductor surface can change the electron affinity, the work function and the surface band bending.<sup>38,39,47</sup> A change in  $\chi$  is caused by a change in the surface dipole while a change in the surface band bending is caused by a change in fixed surface charge density due to electronic interaction of the molecular binding group with the semiconductor surface via the electronic gap states present at the surface (surface states). The work function is affected by both, by a change in the surface dipole and by a change in the surface band bending.

For the operation of DSSCs two molecular interactions with the TiO<sub>2</sub> surface are relevant:

- i. A change of the electron affinity, which changes the energy level of the bottom of the CB ( $E_{CB}$ ) relative to that of the redox potential ( $E_{redox}$ ). According to the kinetic and thermionic emission model this should affect the  $V_{oc}$ , which is limited by energy difference  $E_{CB} - E_{redox}$ . The investigation of this effect is presented in section 4.1 where dye-sensitized TiO<sub>2</sub> electrodes were modified with co-adsorbed dicarboxylic acid and benzoic derivatives with different dipole moments.
- ii. Interaction of the molecular binding group with gap states, which can modify the energy distribution of the gap states. This should affect strongly the electron transport properties of TiO<sub>2</sub> electrodes, which is thought to be governed by trapping events. An experimental investigation of the molecular effect on the transport properties is presented in section 4.2.

Molecular and other effects on the band bending in mesoporous TiO<sub>2</sub> electrodes are usually neglected because the dimensions of the nano-crystals and the excess charge density are too small to support significant band bending.<sup>25,34</sup> A detailed analysis about band bending in single TiO<sub>2</sub> nanoparticles and mesoporous films is presented in section 4.6.2. In chapter 4 electron transport measurements are presented as a function of the surface modification, which was done by molecular adsorption, by electrochemical surface modification or by a change of the surface pH.

## 3 Experimental Section

### 3.1 Solar cell measurements

#### 3.1.1 TiO<sub>2</sub> electrode preparation and characterization

TiO<sub>2</sub> electrodes were prepared from commercially available P25 powder or from particles which were synthesized by dissolving titanium tetra-isopropoxide in isopropanol and hydrolyzing by adding acetic acid till the solution pH = 2. The synthesized TiO<sub>2</sub> slurries consisted of particles with an average diameter of 23 nm, which were characterized by XRD and TEM. After stirring overnight, the isopropanol was evaporated at 82 °C before the suspension was autoclaved at 250 °C for 13 h.

The P25 paste was prepared by dissolving the TiO<sub>2</sub> powder in acetic acid (pH 2) and keeping it for several minutes in an ultrasonic bath to break the P25 aggregates. Carbowax was added to the P25 paste to improve the quality of the films. Glass substrates covered with a conducting fluorine doped tin dioxide layer (Libby Owens Ford, 8 Ω/square) were cleaned with soap, rinsed with de-ionized water (18.2 MΩ), and dried in an air stream. The resulting suspension was spread on the conducting glass substrates by a glass rod, using Scotch tape as spacers. After drying in air, an interconnected network of TiO<sub>2</sub> nanoparticles was formed by annealing (at 250 °C for 30 min) and sintering (at 450 °C for 30 min) before the samples were allowed to cool down to room atmosphere. The thickness of the porous TiO<sub>2</sub> films was well controlled by the viscosity of the slurries and the number of Scotch tape spacers. The TiO<sub>2</sub> films were around 5 μm thick if the spacer thickness was one Scotch tape, 10 μm for two Scotch tapes, stuck on top of each other, and 15 μm when three tapes were used. The 5 μm thick films were used for solar cells measurements while photocurrent transient were measured with films of 5, 10 and 15 μm thickness.

### 3.1.2 Fabrication of compact TiO<sub>2</sub> underlayers

Compact underlayers were provided by Dr. Frank Lenzmann from the Energy Center, the Netherlands (ECN). The compact TiO<sub>2</sub> layers were prepared by spray pyrolysis at a temperature of 450 °C, using a "Camag" spray head (Camag, Muttenz, Switzerland). Compact TiO<sub>2</sub> films of a thickness of about 100 nm were obtained using a spray procedure similar to the one described in ref. 48, for which I used a precursor solution containing 200 mM titanium tetra-isopropoxide and 400 mM acetylacetonone in ethanol. After spray-deposition the samples were left at 450 °C for another 15 minutes, before letting them cool down to room temperature. The compact layers were characterized with a high resolution scanning electron microscope to monitor cracks or inhomogeneous areas in the layer.

### 3.1.3 Fabrication of dye-sensitized solar cells

The dye, [cis-di(isothiocyanato)-bis (4,4-dicarboxy-2,2-bipyridine) ruthenium (II)](also known as N3), purchased from Solaronix SA Co, was adsorbed onto the TiO<sub>2</sub> films from ethanol solution (0.5 mM). To minimize surface adsorbed water, the TiO<sub>2</sub> films were heated to 150 °C and cooled to 80 °C before they were immersed into the solution, where they were kept overnight. After adsorption the films were rinsed with ethanol and dried in a nitrogen stream.

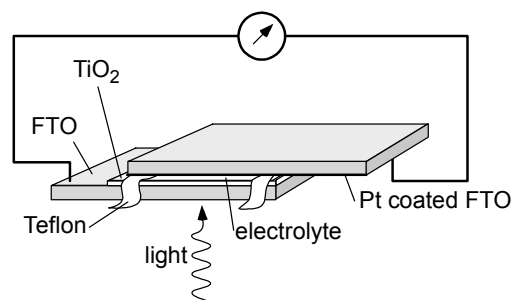


Figure 3.1: Schematic drawing of a DSSC in a sandwich configuration. The cell is illuminated from the bottom side. The dye-sensitized TiO<sub>2</sub> electrode is separated from the Pt counter electrode with Teflon spacers.

To assemble the dye-sensitized TiO<sub>2</sub> electrode into a complete solar cell in a sandwich configuration (shown in Figure 3.1), Teflon spacers were used to avoid direct contact

between the Pt counter and the TiO<sub>2</sub> working electrode. The counter electrode consisted of a conducting glass substrate which was either covered by a Pt film that was sputtered onto the substrate or electrochemically deposited. A drop of the redox electrolyte (0.5 M LiI, 0.05 M I<sub>2</sub>, dissolved in a 1:1 mixture of acetonitrile (ACN) and 3-methyl-2-oxazolidinone) was introduced between the electrodes by capillary forces.

### 3.1.4 Molecular modification of mesoporous TiO<sub>2</sub> electrodes

Two different methods were used to prepare molecular modified mesoporous TiO<sub>2</sub> electrodes. A series of dicarboxylic acid derivatives<sup>39</sup> was adsorbed in a one step process from an ethanol solution that contained the N3 dye (0.5 mM) together with the dicarboxylic acid (0.3 mM). The preparation procedure was identical to the method described above for dye-sensitization. Dicarboxylic acid (DHDC) and its derivatives with two cyano (**dicyano-dicarboxylic acid**, DCDC) or two methoxy groups (**dimethoxy-dicarboxylic acid**, DMDC) were used for molecular modification. These molecules have different dipole moments due to their different functional groups.

For a second set of experiments benzoic acid derivatives were co-adsorbed onto TiO<sub>2</sub> electrodes which were already sensitized with the N3 dye (two step process). For dye adsorption the mesoporous TiO<sub>2</sub> films were immersed overnight into an ethanol solution containing 0.5 mM N3, rinsed and dried, as described above. In a second step these electrodes were immersed into an ACN solution which contained the respective benzoic acid derivative in a concentration of 0.3 mM. The N3 dye does not dissolve well in ACN so that this procedure kept the dye coverage constant while benzoic acids adsorbed to vacant binding sites in between the N3 molecules, which are larger and bulkier and cannot form a monolayer that occupies all binding sites. The dipole moments of the benzoic and dicarboxylic acid derivatives were calculated as described elsewhere.<sup>45</sup>

### 3.1.5 Optical absorption measurements

Optical absorption was measured by transmission spectra of the molecularly modified electrodes with a spectrophotometer (Jasco V-570) to assure that all samples had the same surface coverage of N3 dye. For the baseline measurement mesoporous TiO<sub>2</sub>

films without dye were introduced into the measurement and reference beam. For transmission measurements the dye sensitized electrode was introduced into the measurements beam while a bare TiO<sub>2</sub> film was kept in the reference beam.

### 3.1.6 I-V characterization of dye-sensitized solar cells

Current-voltage ( $I$ - $V$ ) curves in the dark and under illumination were measured with a voltage source (Keithley 230 programmable voltage source) and an Ampere meter (Keithley 195A digital multimeter). The solar cells were illuminated with a halogen lamp and the illuminated surface area had a size between 0.6 to 1 cm<sup>2</sup>, depending on the aperture that was used. The lamp intensity was roughly calibrated to the solar spectrum by comparison of the short circuit current of a Si photodiode measured in the lab and in sun light.<sup>b</sup> Solar cell parameters like the open circuit voltage ( $V_{oc}$ ), the short circuit current ( $I_{sc}$ ), the short circuit current density ( $J_{sc}$ ) and the fill factor (FF) were calculated by a Labview program, which controlled the  $I$ - $V$  system.

## 3.2 Electron transport measurements

### 3.2.1 Preparation of interdigitated micro-electrodes

Micrometer sized, interdigitated electrodes were produced by photolithography. Microscope slides were used as a substrate material. After subsequent cleaning in warm acetone, methanol and isopropanol the glass slides were dried in a nitrogen stream. The glass samples were heated to 80 °C for three minutes before they were covered with the photoresist by spin coating. An adhesion promoter was used to improve adhesion of photoresist to the glass substrate. The photoresist was exposed to UV light for about 10 seconds, hard baked for 3 minutes and exposed to UV light for another 3 minutes, before the samples were immersed into a developer (AZ 726) for 10 to 15 seconds, rinsed in water and dried in nitrogen. After development the quality of the lithography process was checked with an optical microscope.

---

<sup>b</sup> The measurements were performed on the roof of the Perlman building of the Weizmann Institute, Israel, around noon time on a sunny day at the beginning of September.

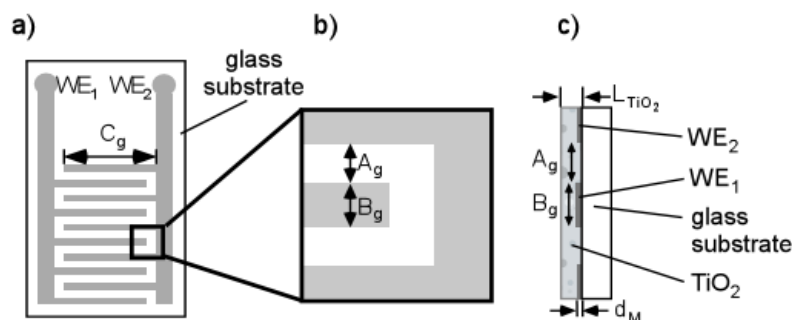


Figure 3.2: (a) Schematic drawing of micro-electrodes used for steady state transport measurements. (b) The magnification shows the gap width  $A_g$  and the finger width  $B_g$ . (c) Cross section of the electrode with a mesoporous  $\text{TiO}_2$  film (with a thickness  $L_{\text{TiO}_2}$ ) deposited on it.

Different metals were investigated as electrode materials, which were thermally deposited in an e-beam evaporator (Edwards). The photoresist together with the excess metal were lifted-off in acetone, which was heated close to its boiling point. In a final step the electrodes were rinsed with de-ionized water and dried in a nitrogen stream. Au turned out to be the most suitable electrode material. It was evaporated with a thickness ( $d_M$ ) of about 100 nm on top of a titanium or chromium underlayer ( $\sim 5$  nm). A schematic drawing of the electrodes is shown in Figure 3.2, where the electrodes are labelled as  $WE_1$  and  $WE_2$ . The insulating gap ( $A_g$ ) between  $WE_1$  and  $WE_2$  was varied from 5 to 150  $\mu\text{m}$  depending on the chosen mask design. The finger width ( $B_g$ ) was 10  $\mu\text{m}$  and the length ( $C_g$ ) varied between 1.2 to 2.0 mm, depending on the electrode design. The number of the fingers was between 100 to 140 (also depending on the chosen design) so that the total gap length  $D_g$  varied from 12 to 15 cm. Mesoporous  $\text{TiO}_2$  films with a thickness ( $L_{\text{TiO}_2}$ ) of about 5  $\mu\text{m}$  were deposited onto the interdigitated electrode by the doctor blade method (as described in section 3.1.1). Figure 3.2c shows the cross section of a mesoporous  $\text{TiO}_2$  film, deposited on the interdigitated structure.

### 3.2.2 Electrochemical modification of $\text{TiO}_2$ films on gap electrodes

$\text{TiO}_2$  films deposited on interdigitated gap electrodes were molecularly modified by adsorption from solution or by electrochemical deposition. In the first case the electrodes were immersed into an ACN solution that contained the respective molecule (benzoic or dicarboxylic acid derivative) at a concentration of 0.5 mM. After

adsorption overnight the electrodes were rinsed with ethanol and dried in an air stream. Electrochemical deposition was performed for molecular modification with derivatives of benzenediazonium-tetrafluoroborate.<sup>49</sup> For this  $WE_1$  and  $WE_2$  were short-circuited and connected as the working electrode in potentiostat system. A potential sweep to -0.9 V vs Ag/AgCl was performed for deposition of the molecules onto the mesoporous film.

### 3.2.3 Bi-potentiostat measurements

For steady state electron transport measurements a bi-potentiostat system (Autolab) was used. The interdigitated micro-electrodes were connected as working electrode one and two ( $WE_1$  and  $WE_2$ ).<sup>50-52</sup> The applied bias was measured with respect to an Ag/AgCl reference electrode ( $RE$ ) and a Pt sheet was used as counter electrode ( $CE$ ). For the measurement a 0.5 M NaCl solution was used as electrolyte. A scheme of the experimental setup is shown in Figure 3.3.

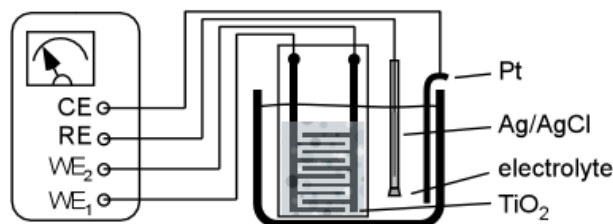


Figure 3.3: Schematic drawing of the bi-potentiostat system. The potential was applied to the working electrodes  $WE_1$  and  $WE_2$  with respect to a Ag/AgCl reference electrode. A Pt metal sheet was used as a counter electrode.

### 3.2.4 Photocurrent transient measurements

Photocurrent transients were measured on mesoporous  $TiO_2$  films of different thickness, deposited on FTO substrate and on FTO, covered with a compact  $TiO_2$  layer. The mesoporous films were immersed into aqueous, 0.5M NaCl electrolyte ( $EL$ ) and excited by the third harmonic of a pulsed Nd:YAG laser ( $\lambda = 355\text{nm}$ , pulse length = 120 ps). The experimental system is shown in Figure 3.4. The sintered  $TiO_2$  films on

the FTO-covered glass substrates were mounted with an O-ring onto a home-made electrochemical cell. The sample was illuminated from the electrolyte (EL) side and the laser flash entered the electrochemical cell through a scattering window (SW) to assure homogeneous illumination intensity throughout the active area, which was approximately  $0.6 \text{ cm}^2$ . The potential of the sample was measured by a voltmeter (V) with respect to a Ag/AgCl reference electrode. A 10 cm long Pt wire (diameter = 0.8 mm) of which an area of  $\sim 2 \text{ cm}^2$  was in contact with the electrolyte, was used as counter electrode and connected to the signal input (SI) of an oscilloscope (Hewlett Packard, 54510B). The transients were measured with an input resistance of the scope of  $1 \text{ M}\Omega$  (dc mode). The scope was triggered from its external trigger input (ETI) by a photodiode (PD), which was excited by the scattered light of the second harmonic, which was also emitted by the Nd:YAG laser. An external potential could be applied by a 9 V battery. The potential was controlled by a simple potential divider, consisting of a fixed resistor ( $R_p$ ) and adjustable resistors ( $R_a$ ).

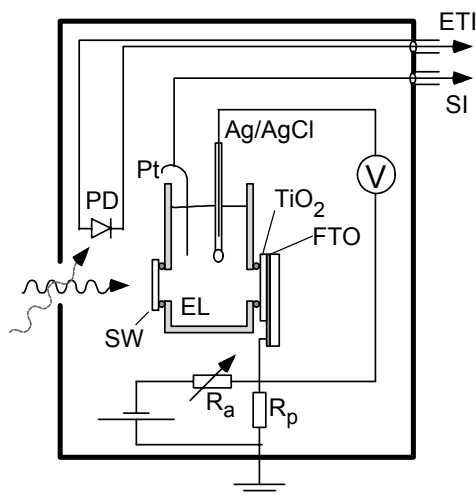


Figure 3.4: Experimental setup for time-resolved transport studies using photocurrent transient measurements.

To improve the signal to noise ratio every transient was measured ten times and averaged. The scope was controlled via a GPIB interface by a Labview program.

Photocurrent transients were recorded

- i. at different electric potentials applied between the FTO substrate and Ag/AgCl reference electrode
- ii. as a function of the laser intensity (0.11 – 3.29 mJ / flash),
- iii. as a function of the electrolyte pH,
- iv. with and without compact TiO<sub>2</sub> underlayer.

### **3.3 Investigation of the FTO/TiO<sub>2</sub> interface**

#### **3.3.1 Transient spectroscopy of the FTO/TiO<sub>2</sub> contact**

Photocurrent transient spectroscopy was used to investigate the electrostatic potential distribution at the FTO/TiO<sub>2</sub> contact. Therefore, mesoporous TiO<sub>2</sub> films with a thickness of 5 μm and compact TiO<sub>2</sub> layers with a thickness of ~100 nm, deposited onto FTO substrate were measured in 0.5 M NaCl or LiCl electrolyte (*EL*). In contrast to the transport measurements described in the previous section, the samples were excited from the glass substrate side by a pulsed N<sub>2</sub> laser ( $\lambda = 337$  nm, pulse duration = 0.5 ns, intensity = 0.1 mJ/pulse). Figure 3.5 shows the experimental system, where the photodiode was excited by a fraction of the incident laser intensity due to a beam splitter (*BS*) that was introduced into the light beam. The photocurrent transient signal was significantly stronger than the signal obtained in the transport measurements, described above, due to electron-hole generation in the vicinity of the FTO substrate. Therefore, there was no need for the 1 MΩ resistor, used in the transport measurements, and the 50 Ω input resistance of the scope could be used.

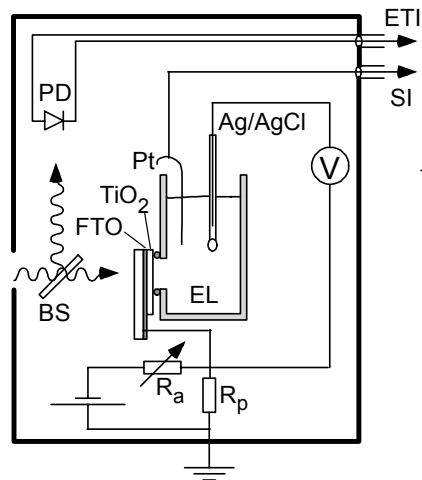


Figure 3.5: Experimental set-up to measure photocurrent with laser light, incident from the substrate side.

An electrostatic potential was applied to the sample in the same fashion as described above. The measurements were performed as a function of applied potential and as a function of the electrolyte's pH value.

### 3.3.2 Kelvin Probe measurements on liquids

The Kelvin probe (KP) method was used to measure the work function of the FTO substrate as well as the redox potential of the  $I^- / I_3^-$  redox electrolyte.<sup>53-55</sup> The FTO work function was measured in ambient air (at a controlled humidity of  $\sim 45-50\%$ ) while a special liquid cell was used to measure the redox potential. This cell was made out of a thin film of sputtered Pt on FTO-covered glass substrate, a microscope cover slide with a thickness of approximately  $100 \mu\text{m}$  and candle wax, which was used to seal and close the cell. The KP was vibrating in front of the glass window and the redox potential was measured through it,<sup>56</sup> as shown in Figure 3.6. The work function and redox potential data were used to derive an energy band diagram for DSSCs. The special feature of this method is that both values are measured with respect to the same reference (the Kelvin probe). A commercially available Kelvin probe (Besocke Delta Phi, Jülich, Germany) in a home-built setup was used for the experiments.

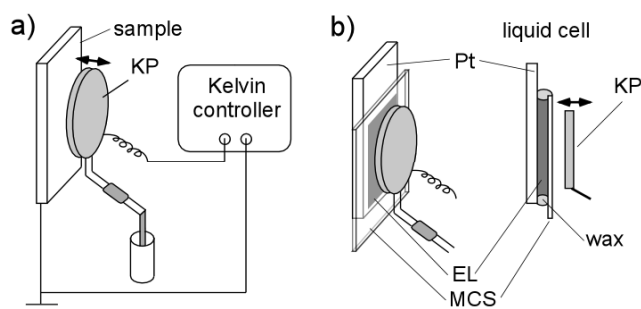


Figure 3.6: (a) Configuration for work function measurements. The Kelvin probe (KP) vibrates in front of the sample. (b) Configuration for redox potential measurements. The compartment of the liquid cell for the electrolyte (EL) consists of a Pt electrode and a microscope cover slide (MCS). The sides are sealed with candle wax.

### 3.3.3 Numerical simulations

Photocurrent transients as well as  $I$ - $V$  characteristics were simulated in Matlab code. The program to simulate photocurrent transients was based on the Forward Time Centred Space (FTCS) finite-difference approximation. A detailed description of the program is presented in section 4.4.

To simulate the  $I$ - $V$  characteristics of DSSCs the system of non-linear equations was solved with the *fsolve* function of Matlab, which is based on the Newton-Raphson method.

## 4 Results

The working principle of DSSCs is still being debated and the different models have been summarized in chapter 2. In this chapter the results of transport and solar cell measurements are presented, which are then used to introduce a new model for the working principle of DSSCs.

Molecular modification of DSSCs was used to tune the solar cell properties like the open circuit voltage, the short circuit current and the fill factor. The molecular shift on the  $V_{oc}$  can easily be described by a dipole related shift of the  $\text{TiO}_2$  conduction band while the difference in the photocurrent requires further investigation. Steady state conductivity measurements that are presented in section 4.2, and the results of time resolved photocurrent measurements, shown in section 4.3, indicated the importance of trapping. The results from section 4.3 show, furthermore, that an analytical expression for photocurrent transients, as presented in the literature,<sup>57-60</sup> is not sufficient for a qualitative and quantitative analysis. A numerical model was developed to investigate the effect of dispersive (i.e., including trap states) transport and recombination on the transient response. The photocurrent transient response is furthermore affected by the FTO/ $\text{TiO}_2$  interface, an aspect that, to the best of my knowledge, was not noted before.

The photocurrent transient measurements were then used for a thorough investigation of the FTO/ $\text{TiO}_2$  interface (section 4.5). This was needed also for fundamental understanding of the DSSC working principle as the FTO/ $\text{TiO}_2$  contact plays a major role in the understanding of DSSCs, as shown in section 2.2. The results indicate that tunneling is the dominant transport mechanism at the mesoporous  $\text{TiO}_2$ /FTO interface if an energy barrier is present. Contact potential difference measurements of the FTO substrate and the redox electrolyte were then used to see if such a barrier is present. The results show that this is indeed the case for the commonly used DSSCs in the dark, something that was not considered in DSSC models in the literature before. In section 4.6 the tunnel junction model for DSSCs is derived, which is based on an analytical expression for electron tunneling at the FTO contact. Numerical  $I$ - $V$  simulations are

used to demonstrate that DSSCs can work without built-in field, and the effect of the tunnel barrier on cell performance is discussed.

## 4.1 Molecular modification of DSSCs

### 4.1.1 *I-V* characteristics of molecular modified DSSCs

Solar cell characteristics were measured on molecularly modified dye-sensitized TiO<sub>2</sub> electrodes. The electrodes were prepared as described in section 3.1.4. Figure 4.1 shows a schematic drawing where some of the binding sites on the TiO<sub>2</sub> surface are occupied by benzoic (4.1a) or dicarboxylic acid derivatives (4.1b). The derivatives used in the experiments had varying dipole moments due to different functional groups in the para-position of the phenyl ring. The series of benzoic and dicarboxylic acids and the used abbreviations are given in Table 4.1. The dipole moments of the benzoic and dicarboxylic acid derivatives were calculated as described elsewhere.<sup>45</sup>

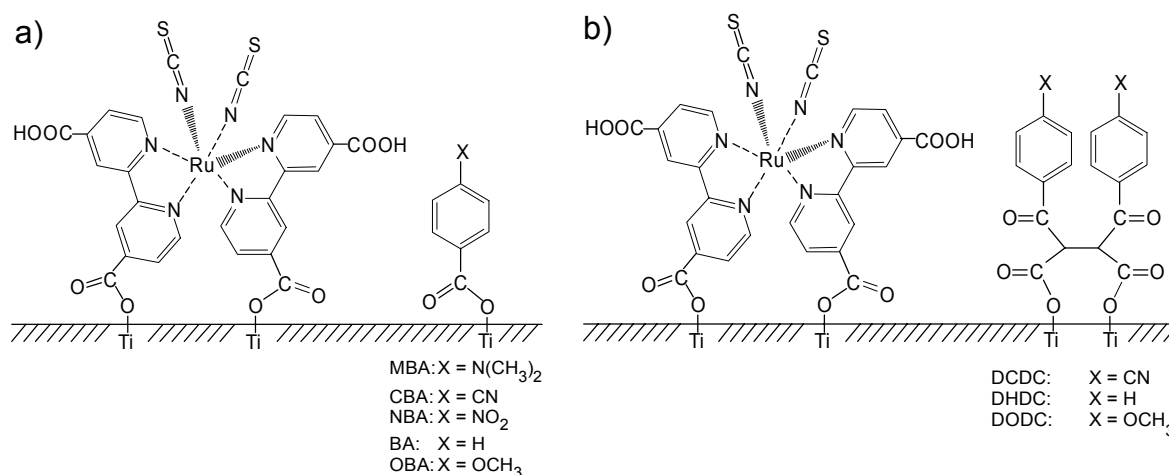


Figure 4.1: (a) Schematic drawing of the molecularly modified TiO<sub>2</sub> surface with benzoic acid derivatives. (b) As (a) with dicarboxylic acid (DHDC) and its derivatives (DODC, DCDC). The concentration ratio between the N3 dye and the dicarboxylic acids was defined by the concentration ratio in the solution as described in section 3.1.4.

*I-V* characteristics of molecular modified TiO<sub>2</sub> electrodes, measured at approximately 1 sun, are shown in Figure 4.2a and b. For both sets the *I-V* curves were normalized with respect to the non-modified TiO<sub>2</sub> electrode. From Figure 4.2a it can be seen that

electrodes modified with OBA and BA show a higher short circuit current ( $I_{sc}$ ) than the unmodified reference electrode, while the  $I_{sc}$  is lower for the electrodes with co-adsorbed MBA, CBA and NBA. Looking at the potential one can see that only the OBA electrode shows a higher  $V_{oc}$  than the reference sample. The fill factor for all electrodes is around 65% ( $\pm 3\%$ ) and thus nearly unaffected by the molecular modification.

All TiO<sub>2</sub> electrodes modified with benzoic acid derivatives were covered by a complete monolayer of dye, due to the two-step preparation method (cf. section 3.1.4). The N3 dye is much larger and bulkier than the relatively small benzoic acid derivatives, such that a monolayer of N3 cannot occupy all binding sites and leaves sites available for molecular modification. Therefore, there are no significant differences in dye coverage between any of the layers with co-adsorbed benzoic acids.

<b>Benzoic acid derivatives</b>		<b>Dicarboxylic acid derivatives</b>	
<b>Bezoic acid</b>	BA	<b>Dicarboxylic acid</b>	DHDC
<b>Dimethylamino benzoic acid</b>	MBA		
<b>Cyano benzoic acid</b>	CBA	<b>Dicyana dicarboxylic acid</b>	DCDC
<b>Nitro benzoic acid</b>	NBA		
<b>Methoxy benzoic acid</b>	OBA	<b>Dimethoxy dicarboxylic acid</b>	DODC

*Table 4.1: Benzoic and dicarboxylic acid derivatives and its abbreviations.*

Figure 4.2b shows the  $I$ - $V$  characteristics of dye-sensitized TiO<sub>2</sub> electrodes with co-adsorbed dicarboxylic acid derivatives. Here the TiO<sub>2</sub> films were modified in a one-step process from a solution that contained the N3 dye plus the functional molecule. During adsorption the dicarboxylic acids compete with dye molecules for available binding sites which results in less than a monolayer of dye on the TiO<sub>2</sub> surface. However, from the transmission spectra, shown in the insert of Figure 4.2b, one can see that the total amount of adsorbed dye is very similar for all modified electrodes. Only the dye coverage of the reference TiO<sub>2</sub> electrode was significantly higher, due to the fact that the solution contained only the N3 dye without additional molecules so that no additional adsorption mechanism competed with dye adsorption.

The  $I$ - $V$  characteristics show the highest current and voltage for the non-modified electrode, due to the highest dye coverage. From the molecular modified samples the electrode with the DODC molecules shows the highest  $I_{sc}$  and the highest  $V_{oc}$ , followed by the DHDC and DCDC modified films. Since the DCDC modified film has a slightly higher dye coverage than the DHDC or DODC modified electrode (see insert of Fig. 4.2b), it is clear that the dicarboxylic acids have a stronger effect on the current and voltage than any effect that can be ascribed to the small variations in the surface concentration of adsorbed dye.

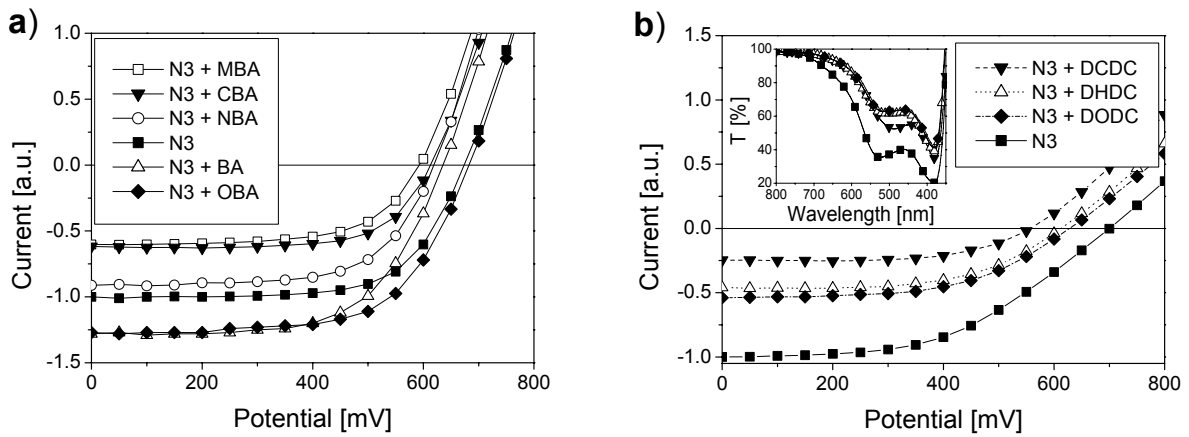


Figure 4.2:  $I$ - $V$  characteristics of DSSCs with co-adsorbed benzoic acid (a) and dicarboxylic derivatives (b). The current is normalized with respect to the unmodified electrode (N3). Optical transmission spectra of dye-sensitized  $TiO_2$  electrodes with co-adsorbed dicarboxylic acid derivatives are shown in the insert of (b).

#### 4.1.2 Molecular impact on the $V_{oc}$ and $I_{sc}$

The effect of the carboxylic and dicarboxylic acid derivatives on the  $V_{oc}$  is shown in Figure 4.3a, where the  $V_{oc}$  is plotted as a function of the molecular dipole moment. The solid line shows the linear fit, which has a slope of 8.6 mV/Debye for the benzoic acids and 5.6 mV/Debye for the dicarboxylic acid derivatives.

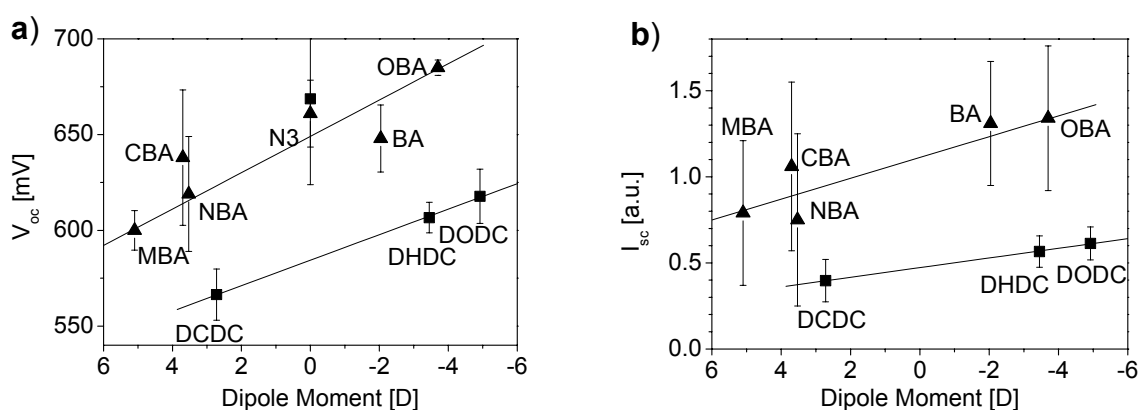


Figure 4.3(a) Open circuit voltage as function of the dipole moment of the co-adsorbed dicarboxylic acid derivatives. (b) Short circuit current as function of the dipole moment, normalized with respect to the non-modified N3 sensitized  $TiO_2$  electrode.

The  $V_{oc}$  of the unmodified reference sample (N3) does not fit with the linear fit of the benzoic and dicarboxylic acids, which can be attributed to the dipole moment of the N3 dye itself, which is more negative than the dipole moment of the methoxy compounds. The MBA modified electrode does not fit the trend when it is plotted with respect to the dipole moment of the free MBA molecule (not shown). One possible way to explain this mismatch is interaction of the  $N(CH_3)_2$  group with a proton, which results in a  $N(CH_3)_2H^+$  group. The protonated dimethylamino benzoic acid has a much more positive dipole moment than the unprotonated one, due to the extra positive charge located at the functional group. If we use the measured  $V_{oc}$  of the MBA sample and put it on the line, obtained from the linear fit made, using the data for the other molecules, we find a dipole moment for the protonated MBA of approximately 5.1 Debye.

I note that  $V_{oc}$  is plotted vs. the dipole moment of the free molecule, which does not take into account any change due to the chemical binding of the COOH group to the  $TiO_2$  surface. From studies on the binding of the N3 dye it is known that the COOH group reacts with OH groups on the  $TiO_2$  surface and creates ester bonds, which most probably imparts a positive contribution to the net dipole moment of the molecule. Nevertheless, this shift should be the same for all the benzoic and dicarboxylic acid derivatives and, thus, while the data shown in Figure 4.3 may be shifted parallel to the x-axes by a constant, their positions will not change relative to each other.

Figure 4.3b shows that the short circuit current also depends linearly on the molecular dipole moment. In chapter 5 it will be discussed that the dipole-dependent  $V_{oc}$  shift can be explained by a shift of the TiO<sub>2</sub> conduction band with respect to the redox potential. There is, however, no obvious explanation for the dipole-dependent behavior of  $I_{sc}$ . A change of  $I_{sc}$  can be caused by, for example, a change in recombination kinetics or by a change in TiO<sub>2</sub> conductivity, caused by molecular passivation of surface states that can act as traps. In the next section steady state transport measurements are presented, which were performed to investigate the effect of molecular modification on the conductivity of mesoporous TiO<sub>2</sub> films.

## **4.2 Electron transport in mesoporous TiO<sub>2</sub> films I: Bi-potentiostat measurements**

Steady state transport measurements were performed in a four-electrode configuration as described in section 3.2.3, where the two contacts of an interdigitated electrode with a micrometer-sized gap were connected as working electrode one and two,  $WE_1$  and  $WE_2$ . The TiO<sub>2</sub> film was immersed into an aqueous NaCl electrolyte (see section 3.2.3) and an Ag/AgCl electrode was used as a reference while a Pt sheet served as a counter electrode. Two potential scans were required to measure the current flow from working electrode one to working electrode two. The first scan was performed without applied potential difference between  $WE_1$  and  $WE_2$  and a cyclic voltammogram between zero and -0.7 V was recorded, where the potential was applied with respect to the reference electrode (base line measurement). A typical scan is shown in Figure 4.4a, recorded with a scan rate of 50 mV/s, which is sufficiently slow to establish steady state conditions at each applied potential. The current into the TiO<sub>2</sub> film increases with increasing negative potential. The slight differences between the curves for  $WE_1$  and  $WE_2$  in (a) are due to the way the bipotentiostat applies the voltage and, possibly, to minor differences in electrode area. The total current of each electrode contains a capacitive and a Faradaic component.

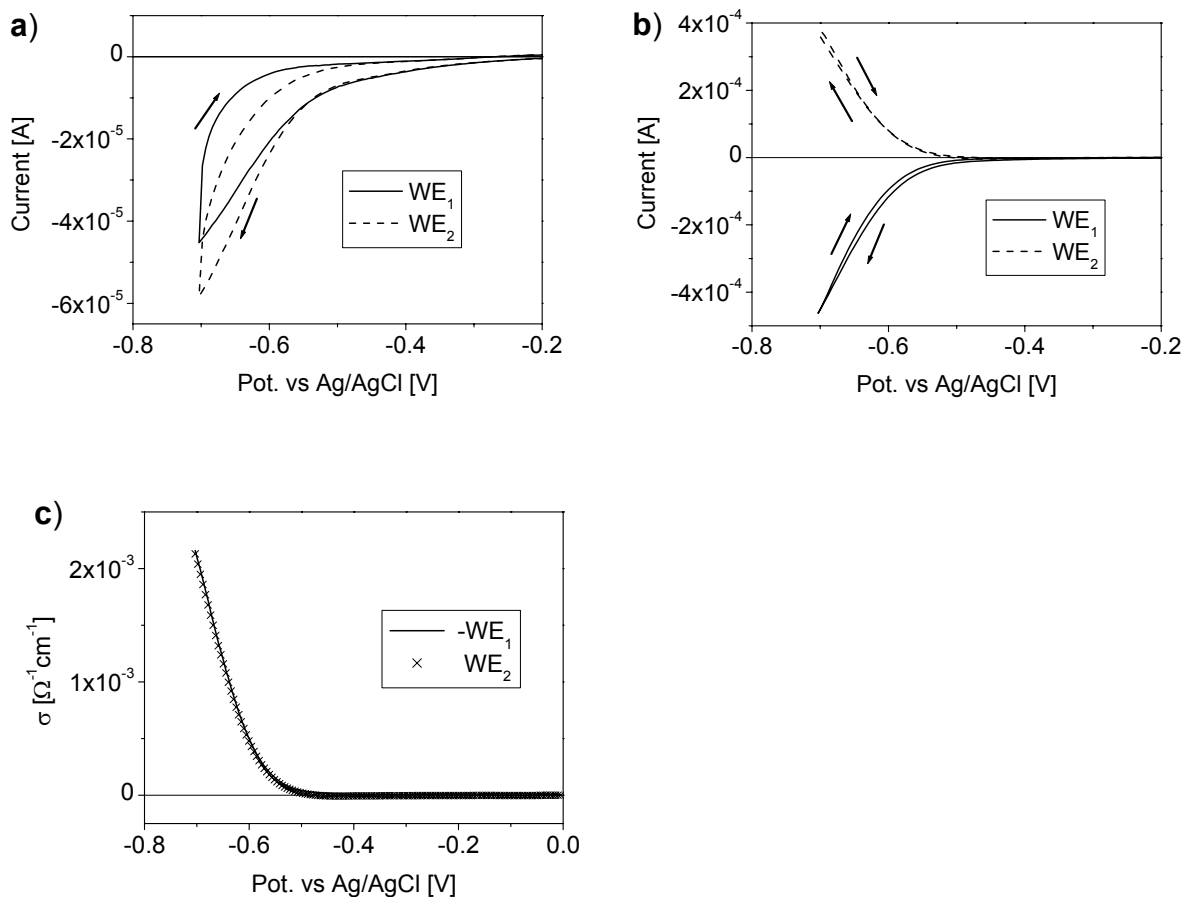


Figure 4.4: (a) Cyclic voltammogram of an interdigitated gap electrode with a mesoporous  $\text{TiO}_2$  film deposited on top of it, without potential difference between working electrode one ( $\text{WE}_1$ ) and working electrode two ( $\text{WE}_2$ ). (b) Cyclic voltammogram of the same electrode with a potential difference of 50 mV between  $\text{WE}_1$  and  $\text{WE}_2$ . The current is dominated by electron transport from  $\text{WE}_1$  into  $\text{WE}_2$  through the  $\text{TiO}_2$  film at applied potentials below -0.5 V. (c) Conductivity, derived from the current shown in (b) minus the respective current in (a). The solid line shows the conductivity, derived from the current which goes out of  $\text{WE}_1$  while the crosses show the conductivity, derived from the incoming current into  $\text{WE}_2$ .

The capacitive component charges the mesoporous structure (electrons fill up trap states) while the Faradaic component is due to electron transfer into the electrolyte when the potential is scanned towards negative potential. The capacitive current changes its sign when the scan direction is reversed, while the Faradaic current depends only on the applied potential and is independent of the scan direction. Because of that the total current differs as a function of the scan direction. A small Faradaic current is required to derive the absolute electron concentration inside the mesoporous  $\text{TiO}_2$  film as a function of the applied potential.

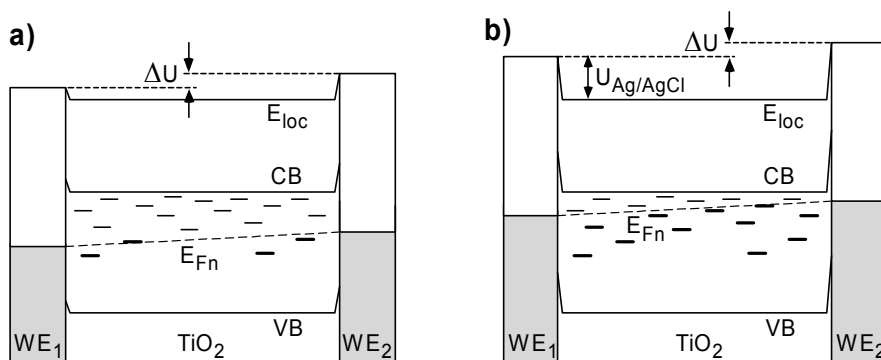


Figure 4.5: Energy band diagram of the working electrodes  $WE_1$  and  $WE_2$  with the mesoporous  $TiO_2$  film at zero potential (a) and negative applied potential  $U_{Ag/AgCl}$  (b). The potential difference  $\Delta U$  between  $WE_1$  and  $WE_2$  is kept constant during the voltage scan, where the potential is applied with respect to the Ag/AgCl reference electrode.

From Figure 4.4a one can see that the sign of the current didn't change when the scan direction is reversed, which clearly shows that a high Faradaic current was the dominant component. This was observed for all measurements, independent of the electrolyte composition, scan rate, potential range or electrode material. This made it impossible to determine the electron concentration inside the  $TiO_2$  film as a function of the applied potential, as was originally planned.

The second potential scan was recorded over the same potential range but with a constant potential difference  $\Delta U$  between the working electrodes (usually between 10 - 50 mV). An energy band diagram is shown in Figure 4.5 where trap levels in the  $TiO_2$  are shown as short horizontal lines (-) and the quasi-Fermi level,  $E_{Fn}$ , is depicted as a dashed line. Trap states below the  $E_{Fn}$  are filled (bold), while traps above  $E_{Fn}$  are empty. From the sign change of the current, shown in the potential scan in Figure 4.4b, one can see that the total current at potentials below -0.5 V is dominated by electron transport through the  $TiO_2$  film. The different signs represent electron injection from  $WE_1$  into the  $TiO_2$  film (negative current) and collection of electrons from the  $TiO_2$  into  $WE_2$  (positive current). At a potential of -0.7 V vs. Ag/AgCl the injection and collection current is approximately one order of magnitude larger than the capacitive and Faradaic current in the base line measurement.

To derive the current,  $I$ , from  $WE_1$  into  $WE_2$ , the base line measurements (Figure 4.4a) were subtracted from the scans shown in Figure 4.4b. From this current the conductivity was derived according to

$$\sigma = \frac{|I|A_g}{D_g L_{TiO_2} \Delta U} \quad (4.1)$$

where  $|I|$  is either the current from  $WE_1$  into the  $TiO_2$  or from the  $TiO_2$  into  $WE_2$ ,  $\Delta U$  is the applied potential difference between  $WE_1$  and  $WE_2$ ,  $A_g$  is the gap width of the interdigitated electrode,  $L_{TiO_2}$  is the  $TiO_2$  film thickness and  $D_g$  is the total gap length (see also section 3.2.1). From Figure 4.4c one can see that the conductivity data, derived from the current through  $WE_1$  (solid line) are in excellent agreement with the data derived from the current through  $WE_2$  (crosses). This means that, *if a potential difference is applied between  $WE_1$  and  $WE_2$* , most of the electrons that are injected into the  $TiO_2$  from  $WE_1$  are collected at  $WE_2$ . This, in turn, implies that under these conditions the loss current into the electrolyte is relatively small compared to the relatively high Faradaic current into the electrolyte *that is measured when no potential difference is applied between the electrodes.*<sup>c</sup>

#### 4.2.1 Molecular effect on the conductivity in mesoporous $TiO_2$ films

The effect of molecular modification of mesoporous  $TiO_2$  electrodes on the conductivity through the  $TiO_2$  between the two working electrodes,  $\sigma$  is shown in Figure 4.6. Molecular modification was carried out electrochemically with derivatives of benzenediazonium-tetrafluoroborate, as described in section 3.2.2. These compounds had the same functional groups as the benzoic and dicarboxylic acid derivatives. Figure 4.6 shows the conductivity as a function of the applied potential vs the Ag/AgCl reference electrode and one can distinguish two linear regimes (note that the conductivity is plotted on a logarithmic scale). In both regimes the conductivity increases exponentially with negative applied potential. The conductivity has to be

---

<sup>c</sup> “Relatively high” is meant with respect to the total current; the total current is on the order of  $10^{-5}$  A if  $\Delta U = 0V$  and is dominated by a loss current into the electrolyte while the total current is on the order of  $10^{-4}$  A when a potential difference  $\Delta U = 50$  mV is applied, and dominated by transport through the  $TiO_2$  film (see Figure 4.4a & b).

larger than  $\sim 3 \cdot 10^{-6} \Omega^{-1} \text{cm}^{-1}$  to exceed the noise level of the measurement. Therefore the low conductivity regime of the non-modified reference film ( $\text{TiO}_2$ ) cannot be seen from Figure 4.6. The conductivity in the first regime at potentials more positive than  $-0.4 \text{ V}$  has a smaller slope than at potentials more negative than  $-0.4 \text{ V}$  in the second regime. At potentials more negative than  $-0.6 \text{ V}$  the slope decreases again. This can be attributed to the series resistance of the interdigitated electrode that becomes relevant at this potential range: The total current at an applied potential of  $-0.6 \text{ V}$  is around  $0.2 \text{ mA}$  (see Figure 4.4b) and the series resistance of the interdigitated electrode is around  $50 \Omega$ , which results in a potential drop of  $10 \text{ mV}$  across the series resistor. This is already 20% of the total potential difference of  $50 \text{ mV}$  applied between  $WE_1$  and  $WE_2$  so that the real applied potential difference is significantly decreased.

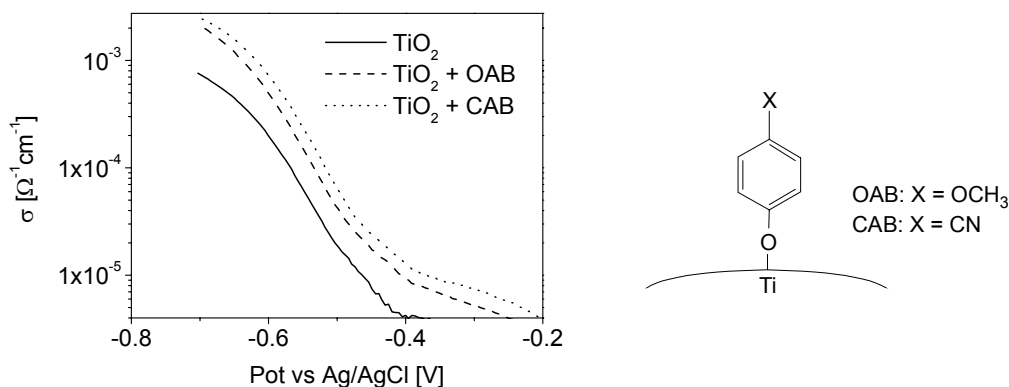
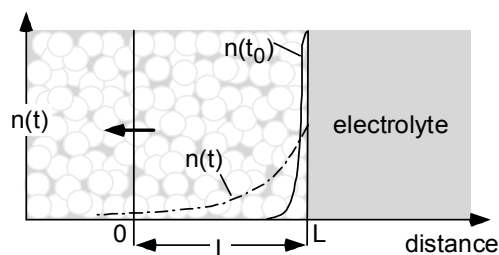


Figure 4.6: Conductivity plot (like in Figure 4.4c but on a logarithmic scale) of a bare, mesoporous  $\text{TiO}_2$  film and molecular modified films with electrochemical deposited 4-methoxy-benzenediazonium-tetrafluoroborate (OAB) and 4-cyano-benzenediazonium-tetrafluoroborate (CAB), schematically shown at the right side.

The high Faradaic current that dominated the base line measurements ( $\Delta U = 0 \text{ V}$ ) made it impossible to derive the electron density inside the  $\text{TiO}_2$  film, which is needed to derive electron mobilities. It was originally planned to investigate the molecular effect on the mobilities and to draw conclusions about the molecular effect on the electronic gap states, which act as electron traps and might be affected by molecular adsorption. Thus bipotentiostat measurements could not be used to the extent, as originally planned. To investigate the impact of electronic trap states on the electron transport in a more quantitative fashion I used time-resolved measurements (photocurrent transients) which are described in the next section.

### 4.3 Electron transport in mesoporous TiO<sub>2</sub> films II: Photocurrent transient measurements

Time resolved measurements on mesoporous TiO<sub>2</sub> and related systems have been widely presented in the literature to determine an effective diffusion constant for electrons, which includes trapping and detrapping events. Such measurements were done in the frequency domain as well as in the time domain.<sup>10,57-65</sup> In this chapter I present time domain measurements (photocurrent transient measurements) where I investigated in detail the effect of recombination and electron traps on the effective electron diffusion constant,  $D_e$ . The excess charge carrier profile was generated by UV light, absorbed in the TiO<sub>2</sub>. Photo-generated holes were injected into the electrolyte much faster than photo-generated electrons. In such way an excess electron density remained in the TiO<sub>2</sub>. This excess served to investigate the electron transport properties. The TiO<sub>2</sub> surface was modified by changing the pH of the electrolyte rather than by adsorbing organic molecules, to avoid photo-oxidation of organic molecules on the TiO<sub>2</sub> surface (by the photogenerated holes) which would lead to unstable experimental conditions.



*Figure 4.7: Schematic drawing of a semi-infinite mesoporous film, where the current is measured at a distance  $L$  from the electrolyte side, which is equivalent to film thickness in the measurement. The electron density,  $n$ , is shown immediately after laser excitation ( $n(t_0)$ ) and at a time  $t$  after the illumination.*

Recombination and dispersive transport, caused by trapping and detrapping events of electrons in electronic gap states, is usually neglected for the analysis of photocurrent transient measurements. Furthermore, the nature of the FTO/TiO<sub>2</sub> interface is neglected

in the analysis of such measurements. Rather, it was assumed that the mesoporous TiO<sub>2</sub> film extends semi-infinitely and that the current is detected at a distance  $L$  from the electrolyte side, equivalent to the film thickness, as shown schematically in Figure 4.7.

From an analytical solution of electron diffusion through the TiO<sub>2</sub> film one can derive an effective electron diffusion constant,  $D_e$ , from the transient time of the peak,  $t_p$  and the film thickness,  $L$ , via

$$D_e = \frac{L^2}{6t_p} \quad (4.2)$$

Different approaches to derive  $D_e$  from photocurrent transients are presented in the literature, (for example the exponential decay of the transient current can be used to derive  $D_e$ ), but these approaches will not be used as they are less straightforward to use than what will be presented here.

In the following, photocurrent transients are reported, which were measured as function of the applied potential, the laser intensity and the pH value of the electrolyte. Furthermore, measurements on samples with and without a compact TiO<sub>2</sub> underlayer between the FTO substrate and the mesoporous TiO<sub>2</sub> film are presented. In section 4.4 a numerical model to simulate photocurrent transients is given. In contrast to analytical solutions, the numerical model enables also the investigation of dispersive transport and recombination on the transport and the transient response. In chapter 5 the measured results will be compared to numerically simulated transients and discussed in terms of trap filling, recombination and the  $RC$  time constant of the measurement system. The effect of the  $RC$  constant on the transient response has been mentioned in the literature<sup>59</sup> but was never thoroughly investigated and discussed.

In the following the effective diffusion constant  $D_e$  will always be derived from the transient peak time  $t_p$  according to eq. (4.2). This will also be done for simulated transients, presented in section 4.4, in order to compare the input parameters of the simulations with the diffusion constant, that is derived from the simulated transient peak time.

### 4.3.1 Potential dependence of photocurrent transients

All measurements, presented in this section, were performed on mesoporous  $\text{TiO}_2$  films immersed into aqueous 0.5 M NaCl electrolyte solution where the surface area, exposed to the laser flash, was approximately  $0.6 \text{ cm}^2$ . Potential-dependent photocurrent transients are shown in Figure 4.8a & b, measured on a  $5 \mu\text{m}$  thick, mesoporous film, with (b) and without (a) compact  $\text{TiO}_2$  underlayer,. The potential was applied to the FTO substrate and measured with respect to a Ag/AgCl reference electrode, while the laser intensity was kept constant at 0.40 mJ per pulse. For samples without compact layer the onset of the transient signal shifts from 10 ms for applied potentials more positive than 0.29 V, down to 0.2 ms, when the potential is decreased to -0.25 V. A similar shift is observed for the transient peak time  $t_p$ , which also decreases by roughly one order of magnitude towards shorter times with negative applied potential. The (dark) open circuit potential (OCP) of the  $\text{TiO}_2$  working electrode in thermal equilibrium vs. Ag/AgCl was approximately 0.45 V. Thus, the transient onset and peak shift towards shorter times if an external potential, negative with respect to the OCP, is applied.

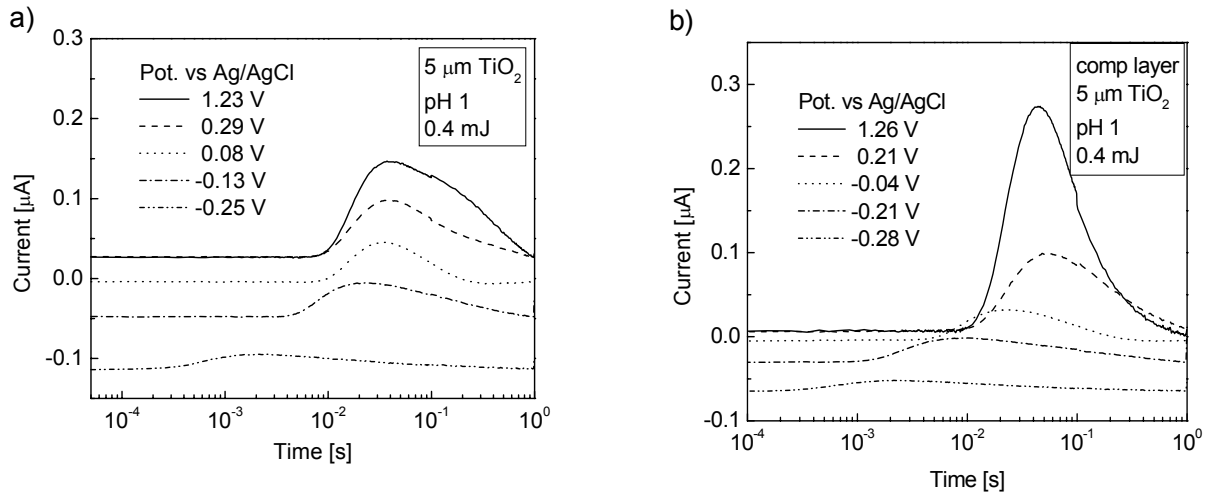


Figure 4.8: (a) Photocurrent transients of a  $5 \mu\text{m}$  thick, mesoporous  $\text{TiO}_2$  film, directly sintered onto FTO substrate, measured at different applied potentials between the FTO and a Ag/AgCl reference electrode in the electrolyte. (b) Photocurrent transients of a similar film but with an approximately 100 nm thick, compact  $\text{TiO}_2$  underlayer between the FTO substrate and the mesoporous film.

The results for samples with a compact  $\text{TiO}_2$  underlayer are qualitatively and quantitatively similar, as can be seen from Figure 4.8b. Furthermore, in both cases (with and without underlayer) the transients are superimposed on a background current which is caused by the bias applied to the FTO substrate. Electron transfer from the FTO into the electrolyte explains the negative background current at negative applied potentials. This negative current is smaller for samples that include a compact  $\text{TiO}_2$  layer than for those without, which indicates that electron transfer from the FTO substrate into the electrolyte is partly, but not completely blocked by the compact layer.

The transient peak time for samples with (filled circles) and without underlayer (empty circles) as a function of the applied potential is depicted in Figure 4.9a. Both systems show a linear potential dependence of  $t_p$  between -0.3 to 0.1 V. At more positive potentials the peak time reaches a plateau at around 40 ms for the mesoporous film without underlayer. In contrast, the linear increase for samples including a compact underlayer continues up to 0.3 V. At more positive potentials  $t_p$  decreases and converges towards the plateau value of the system without underlayer. Figure 4.9b shows the diffusion coefficient, which is derived from the data plotted in Figure 4.9a according to eq. (4.2). One can see that the diffusion coefficient increases by more than one order of magnitude at negative applied potential.

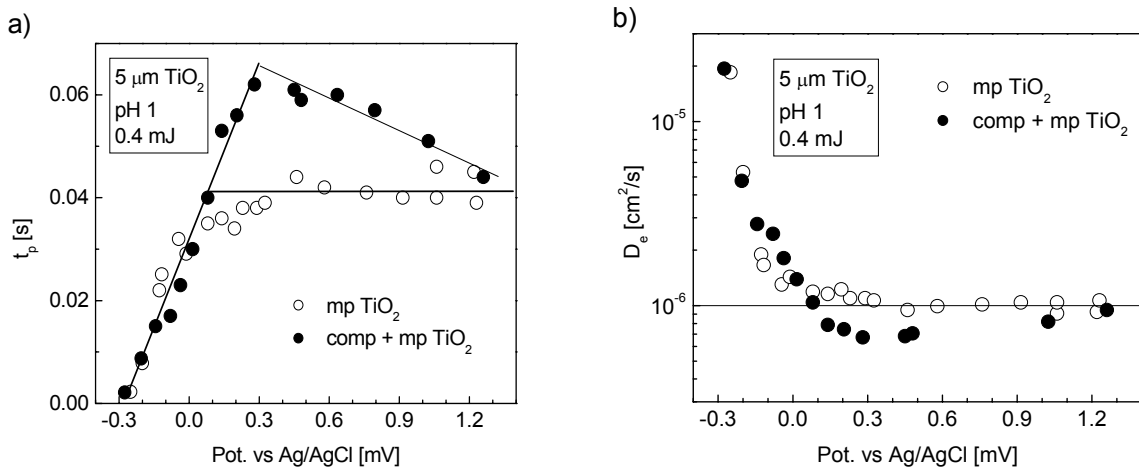


Figure 4.9: (a) Photocurrent transient peak time  $t_p$  for a 5 μm thick, mesoporous  $\text{TiO}_2$  film, with (filled circles) and without (empty circles) compact underlayer as a function of the external applied potential. (b) Diffusion coefficient derived from (a) according to eq. (4.2)

### 4.3.2 Light intensity dependence of photocurrent transients

Photocurrent transients as a function of the incident laser intensity were measured on 5, 10 and 15  $\mu\text{m}$  thick mesoporous  $\text{TiO}_2$  films at pH 1, where the intensity was varied from 0.11 mJ to 3.76 mJ per light pulse. The measurements shown in Figure 4.10a were performed with a 5  $\mu\text{m}$  thick  $\text{TiO}_2$  film. One can see that the onset of the transient response shifts by one order of magnitude towards shorter times with increasing light intensity - from approximately 25 to 2.5 ms. Furthermore,  $t_p$  shifts towards shorter transient times with increasing light intensity, similar to the shift observed at negative applied potential. The diffusion coefficient derived according to eq. (4.2) is plotted in Figure 4.10b for the 5  $\mu\text{m}$  (filled triangles), 10  $\mu\text{m}$  (filled squares) and 15  $\mu\text{m}$  thick  $\text{TiO}_2$  film (open circles). One observes a steady increase in the diffusion coefficient with increasing light intensity, which indicates that the transport is dispersive. i.e., the diffusion coefficient becomes a function of the electron concentration in the  $\text{TiO}_2$ . The observed increase of  $D_e$  resembles a square root or logarithmic dependence on the light intensity. In section 5.1.4 I will show that the dependence between  $D_e$  and  $I_{\text{Laser}}$  contains information about the energy distribution of electronic trap states in the  $\text{TiO}_2$ .

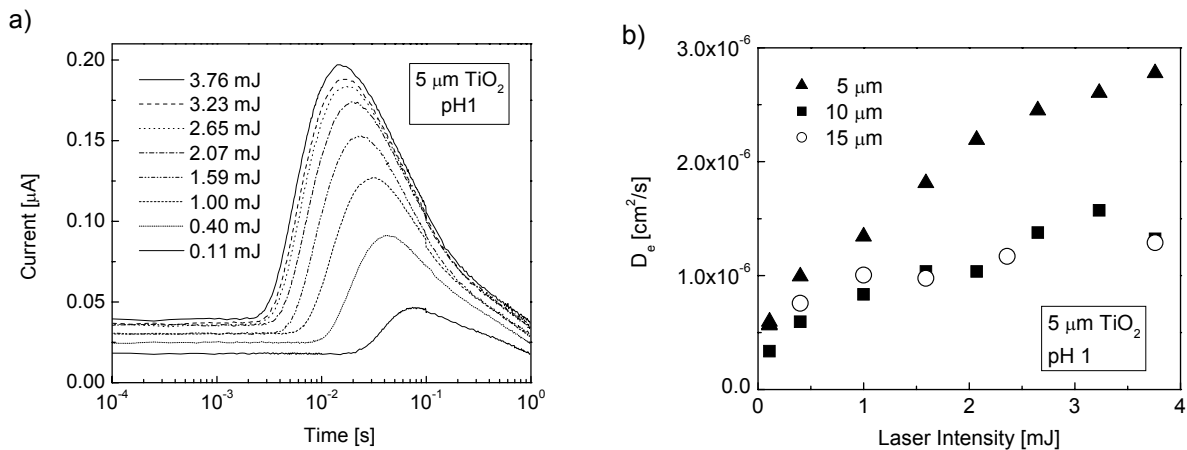


Figure 4.10: (a) Photocurrent transients measured on a 5  $\mu\text{m}$  thick, mesoporous  $\text{TiO}_2$  film, immersed in 0.5 M NaCl electrolyte (pH 1) as a function of the laser intensity. (b) Electron diffusion coefficient (calculated from  $t_p$  according to eq. 4.1) as a function of the laser intensity, measured for three different film thicknesses (without compact underlayer).

Furthermore, a constant background current, which depends on the laser intensity, can be seen at transient times shorter than 2 ms. The origin of this current is that there is a

non-equilibrium situation inside the mesoporous TiO<sub>2</sub> film, during the time interval between two laser excitation pulses. The laser repetition rate of 1 Hz did not allow the mesoporous system to reach thermal equilibrium. Therefore, the laser excitation served to increase the electron density inside the film, e.g. to fill up trap states. Prior to each measurement the film was exposed to 10 to 20 laser flashes in order to pump the system into a steady state. This pumping process can clearly be seen in Figure 4.11 where the first four transients were recorded at different applied potential.

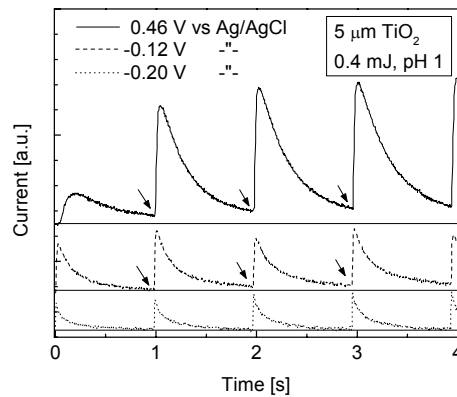


Figure 4.11: The initial four transients measured at different bias of the FTO substrate with respect to a Ag/AgCl reference electrode.

For a potential of 0.46 V vs Ag/AgCl one can see a weak first transient, followed by a stronger second transient. Between the third and the fourth transient there is no significant difference, so that the system can be considered to be in steady state after three laser excitations in this specific case. One can also see that the transient current does not decay to zero between two laser flashes, which results in an excess electron density in the steady state (see arrows in Figure 4.11). The dashed transient curve in Figure 4.11 was measured at an applied potential of -0.12 V vs Ag/AgCl. It can be seen that the first transient has already the maximum peak intensity while a slow increase in the steady state background current can be observed, which is also pointed out by arrows. At negative applied potential the electron density inside the TiO<sub>2</sub> film is increased so that a certain amount of trap states is already filled. The relative increase in the electron concentration due to laser excitation is significantly lower at negative applied potential so that the transient current decays almost back to the dark current. At an applied potential of -0.20 V vs. Ag/AgCl, shown as the dotted graph, the effect of

electron pumping due to laser excitation on the steady state is negligible. The first photocurrent transient does not differ significantly from the following ones and the current decays back to the steady state value before the measurement.

### 4.3.3 pH dependence of photocurrent transients

Photocurrent transients as a function of the pH of the electrolyte were performed on mesoporous  $\text{TiO}_2$  films with and without compact  $\text{TiO}_2$  underlayer at two different laser intensities (0.40 and 2.07 mJ/pulse). Photocurrent transients measured with an intensity of 2.07 mJ/cm<sup>2</sup> on a 5  $\mu\text{m}$  thick film are shown in Figure 4.12a. One can see that the transient intensities strongly depend on the pH value of the electrolyte (note that here the current is plotted on a logarithmic scale). The current strongly decreases with increasing pH value while the transient onset and the peak time increase with increasing pH. The background current is highest at low pH and decreases with increasing pH. At pH values higher than 6 it was not possible to monitor any transient current.

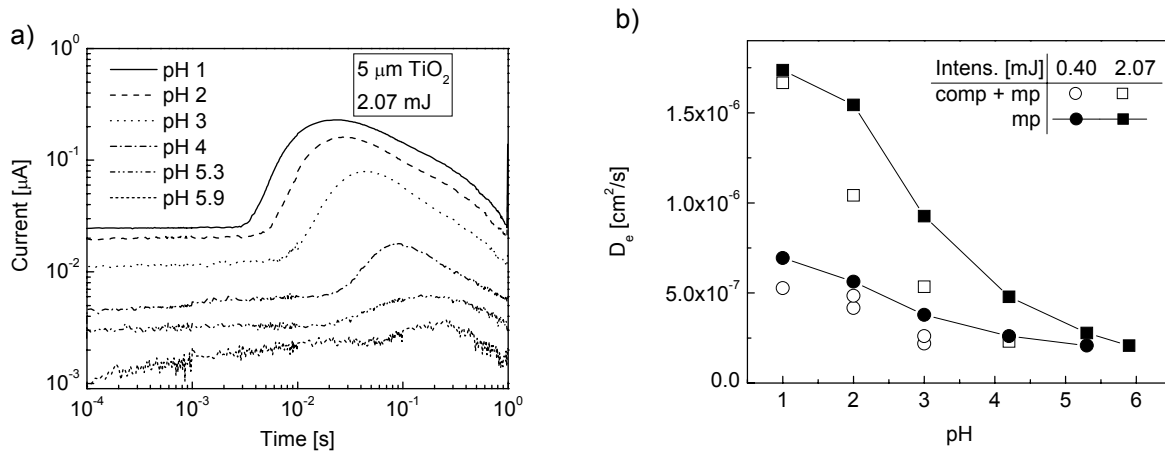


Figure 4.12: (a) Photocurrent transient measured on a 5  $\mu\text{m}$  thick, mesoporous  $\text{TiO}_2$  film, as a function of the solution pH (0.5 M NaCl). The laser intensity was 2.07 mJ for all curves. (b) The diffusion coefficient as a function of the solution pH for a 5  $\mu\text{m}$  thick, mesoporous  $\text{TiO}_2$  film, directly deposited onto FTO substrate (mp) or a substrate covered with a compact  $\text{TiO}_2$  underlayer (comp + mp). The solid circle and square symbols are results of measurements done at 0.40 mJ. The open symbols are results that were measured at 2.07 mJ.

Figure 4.12b shows the electron diffusion coefficients for a mesoporous film including underlayer (empty symbols) and a film without underlayer (filled symbols with lines), measured at 0.4 mJ (circles) and 2.07 mJ (squares), calculated from the transient peak time  $t_p$  according to eq. (4.2). One can see that the diffusion coefficient decreases roughly by a factor of three when the pH is raised from 1 to 6.

## 4.4 Electron transport in mesoporous TiO<sub>2</sub> films III: Numerical simulations

### 4.4.1 The SLICE model for numerical photo-transient simulations

To analyze photocurrent transients it is necessary to investigate the impact of recombination, trapping and detrapping and the FTO/TiO<sub>2</sub> contact. Analytical solutions require a non-dispersive transport and a negligible recombination. To overcome this restriction I developed a numerical model which allows a detailed investigation of photocurrent transients. The original design of the model included the mesoporous TiO<sub>2</sub> film as well as the electrolyte, such that the experimental system was divided into two parts:

- a) the mesoporous TiO<sub>2</sub> structure with the electrolyte in its pores.
- b) the electrolyte itself, which is present outside the TiO<sub>2</sub> film and the Pt counter electrode.

The experimental system was divided for numerical treatment into a discrete number of slices, which are the origin of the model's name.  $Z_{\text{TiO}_2}$  and  $Z_{\text{el}}$  are the number of slices in region a) and b), respectively, each with a constant thickness  $\delta z_{\text{TiO}_2}$  and  $\delta z_{\text{el}}$ . For the simulations it was assumed that light-generated electrons remain in the TiO<sub>2</sub> film while holes are immediately injected into the electrolyte. Electron-hole recombination inside the TiO<sub>2</sub> was neglected so that electron transfer into the electrolyte was the only recombination mechanism that was considered. For the calculations the TiO<sub>2</sub> film contained only excess electrons while excess positive charges were only present in the electrolyte. Electrostatic fields in the mesoporous film and in the electrolyte were

neglected due to the screening abilities of the electrolyte. Charge exchange between the slices was only possible by diffusion. Electron transfer from the  $\text{TiO}_2$  into the FTO was the only process considered at this interface, while the transfer of positive charges into the Pt was the only charge transfer mechanism considered at the Pt electrode. The transfer directions are depicted as arrows in a schematic drawing of the system, shown in Figure 4.13.

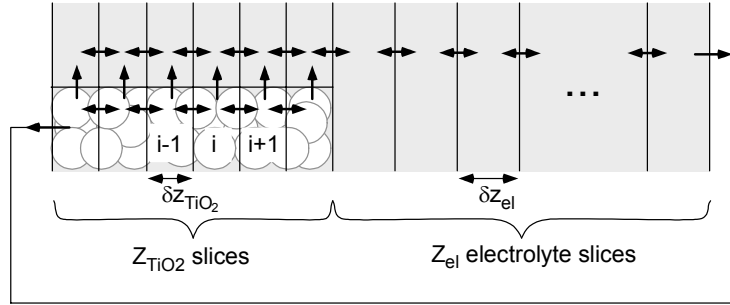


Figure 4.13: Schematic drawing of the discretized  $\text{TiO}_2$  film immersed into the electrolyte. The solid lines show how the system is divided into slices of width  $\delta z_{\text{TiO}_2}$  and  $\delta z_{\text{el}}$ .

#### 4.4.1.1 Photo generation

The generation of electrons and positive charges in the electrolyte, due to laser excitation in the  $i^{\text{th}}$  slice, is defined by the Lambert-Beer law

$$J_G(i) = -qB_G I_0 \exp(-\alpha(L - z(i))), \quad (4.3)$$

where  $I_0$  is the laser energy per area per flash,  $\alpha$  is the absorption coefficient,  $L$  the film thickness,  $z_i$  the distance of slice  $i$  from the FTO substrate and  $B_G$  is a normalization constant, which is defined as

$$B_G = \left( A \delta z_{\text{TiO}_2} \sum_{i=1}^{z_{\text{TiO}_2}} \exp(-\alpha(L - z(i))) \right)^{-1} \quad (4.4)$$

with the illuminated surface area  $A$ .

#### 4.4.1.2 Trap induced dispersive transport

The current density between slice  $i$  and  $i+1$  is given by

$$J_e(i + 1/2) = -qD_e \frac{n(i+1) - n(i)}{\delta z} \quad \text{and} \quad (4.5a)$$

$$J_h(i + 1/2) = qD_h \frac{p(i+1) - p(i)}{\delta z} \quad (4.5b)$$

for electrons and positive charges. The electron density in the  $i^{\text{th}}$  slice is defined as  $n_i$ , while the concentration of positive charges in the electrolyte is defined by  $p_i$ . In the electrolyte the diffusion coefficient  $D_h$  is a constant, while electron transport in the mesoporous  $\text{TiO}_2$  structure depends on an effective diffusion coefficient, which includes trapping and detrapping events. Numerically this can be expressed by a diffusion coefficient which depends on the electron concentration in the  $\text{TiO}_2$ , or, more precisely, on the electron concentration between two slices

$$D_e(i + 1/2) = D_e(n(i + 1/2)) \quad \text{with} \quad n(i + 1/2) = \frac{n(i) + n(i+1)}{2} \quad (4.6)$$

A reasonable first order approach is to assume that the diffusion coefficient depends linearly on the electron density  $n$  as proposed by Cao *et al.*<sup>65</sup> To include different trap state distributions in energy space, a more sophisticated approach was chosen for the simulations presented in sections 4.4.3, 4.4.4 and 4.4.6, where the diffusion coefficient depends on the electron density as well as on some dispersion parameter  $dp$  so that

$$D_e(i + 1/2) = \left( \frac{n(i + 1/2)}{N_{CB}} \right)^{dp} D_{e,0} \quad \text{for} \quad n(i + 1/2) < N_{CB} \quad (4.7a)$$

$$D_e(i + 1/2) = D_{e,0} \quad \text{for} \quad n(i + 1/2) \geq N_{CB} \quad (4.7b)$$

where  $N_{CB}$  is the effective density of electronic states at the bottom of the  $\text{TiO}_2$  CB (defined by eq. 2.2) and  $D_{e,0}$  is the diffusion constant, which describes the diffusion of CB electrons in the absence of electronic gap states. Equation 4.7a reduces to the regular (non-dispersive) diffusion constant when the dispersion parameter  $dp$  is zero or it describes a diffusion coefficient as proposed in ref. 65, if  $dp = 1$ .

#### 4.4.1.3 Recombination

The recombination in the most general case depends on the electron density in the TiO<sub>2</sub> and on density of positive charge in the electrolyte. However, experimentally it seems that the recombination is determined by the density of adsorbed OH groups to the TiO<sub>2</sub> surface rather than by positive charges in the electrolyte.<sup>66,67</sup> Therefore a recombination mechanism was used which depends only on the excess electron density in the TiO<sub>2</sub> and not on the density of positive charges such that the recombination current is defined as.

$$J_R(i) = -qK_n \frac{(n(i) - n_0)^{kp}}{N_k^{kp-1}} \quad (4.8)$$

where  $n_0$  is the thermal equilibrium electron density in the TiO<sub>2</sub> film

$$n_0 = N_{CB} \exp\left(\frac{E_F - E_{CB}^{TiO_2}}{k_B T}\right) \quad (4.9)$$

For the simulation of photocurrent transients presented in section 4.4.4 the recombination current was defined as a function of the excess electron density ( $n(i) - n_0$ ), a rate constant  $K_n$ , a recombination exponent  $kp$  and a normalization constant  $N_k$ . The normalization constant has no physical meaning and was chosen to be  $N_k = 10^{18} \text{ cm}^{-3}$  to keep the  $K_n$  values in the same order of magnitude for different recombination exponents  $kp$ . The recombination exponent  $kp$  defines the order of the recombination reaction. In the discussion in chapter 5 this rather mathematical approach will be related to the microscopic recombination mechanism.

This definition of the recombination mechanism does not consider specific interaction with positive species in the electrolyte such that the SLICE model reduces to a one type charge carrier model, which considers only electrons in the TiO<sub>2</sub> and doesn't deal with the transport properties of the electrolyte.

#### 4.4.1.4 Time evolution of the charge carrier densities

The carrier density was calculated according to the continuity equation for every time step,  $t_k$

$$n(i, t_k) = n(i, t_{k-1}) + \left( \frac{J_e(i + 1/2) - J_e(i - 1/2) + J_G(i) - J_R(i)}{-q\delta z} \right) (t_k - t_{k-1}) \quad (4.10a)$$

$$p(i, t_k) = p(i, t_{k-1}) + \left( \frac{-J_h(i + 1/2) + J_h(i - 1/2) + J_G(i) - J_R(i)}{-q\delta z} \right) (t_k - t_{k-1}) \quad (4.10b)$$

A schematic drawing of the sliced structure is shown in Figure 4.14, which depicts the current densities from the neighboring slices into the  $i^{\text{th}}$  slice.

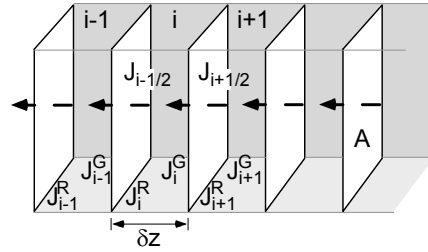


Figure 4.14: The density of charge carriers inside the  $i^{\text{th}}$  slice depends on the generation and recombination currents,  $J_R(i)$  and  $J_G(i)$ , as well as on the current which is entering and leaving the slice,  $J(i+1/2)$  and  $J(i-1/2)$ , respectively. The interface area between slices is denoted with  $A$ .

#### 4.4.1.5 Including the FTO/TiO<sub>2</sub> contact

There are several possibilities to include the FTO/TiO<sub>2</sub> contact into the model. The simplest approach is what will be called the numerical contact, where it is assumed that the electrostatic potential and the electron concentration of the FTO substrate remain unaffected during the transient measurement. Furthermore, simple diffusion into the contact is assumed.

From the experimental point of view one knows that the quality of transient response (the signal to noise ratio) as well as the transient shape<sup>10</sup> are dependent on the input resistance  $R_i$  of the oscilloscope or the measurement resistor  $R_m$  used to record the transient. Most of the published transient data on mesoporous TiO<sub>2</sub><sup>58,59,61</sup> or ZnO<sup>60</sup>

films were measured with an oscilloscope input resistance of 1 M $\Omega$ . The effect of the  $RC$  time constant on the transient measurement has been mentioned in the literature<sup>10,59</sup> but has never been investigated in detail. In section 4.4.6 the impact of the measurement resistor and the  $RC$  time constant will be shown and discussed in detail in chapter 5. It will be shown that this resistance affects the shape of photocurrent transients. A high input resistance (e.g. the 1 M $\Omega$  input resistance of the oscilloscope) changes the electrostatic potential of the FTO substrate during the transient measurement. Numerically this can be introduced into the model and such a contact will be called an  $RC$  contact.

Both contact types are depicted in Figure 4.15b & c, where the current from one slice to another is schematically depicted by resistors  $R_D$  and one has to note that these resistors represent diffusion currents. Figure 4.15b shows the numerical contact, which includes simple diffusion into the contact. Figure 4.15c shows the  $RC$  contact which includes the capacitance of the FTO contact, due to a Helmholtz layer at the FTO/electrolyte interface, and the measurements resistor  $R_m$ .

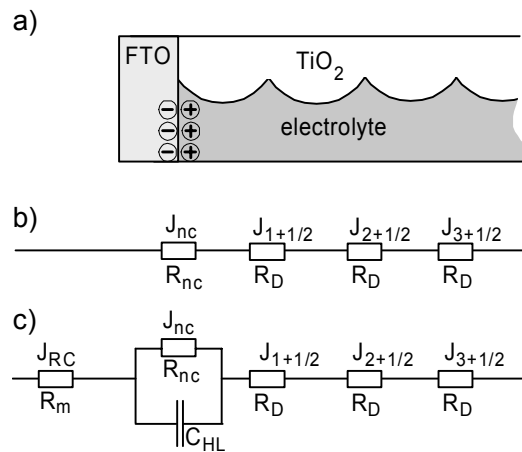


Figure 4.15: (a) Schematic picture of the FTO/TiO<sub>2</sub>/electrolyte interface, which shows the charges of a Helmholtz layer at the FTO/electrolyte interface. (b) Equivalent circuit for the contact region, with the contact considered as numerical contact. The numerically calculated transient current is  $J_{nc}$ . (c) Contact region for an RC contact which includes a Helmholtz capacitance  $C_{HL}$  and the measurement resistor  $R_m$  of the system.

#### 4.4.1.6 The numerical contact

The numerical contact is the simplest method to include the FTO contact into the system. The current into the contact is defined as

$$J_{nc} = -2qD_e \frac{n(1) - n_{FTO}}{\delta z} \quad (4.11)$$

and depends on the electron density  $n_l$  of the slice in contact with the substrate and on the electron density in the FTO substrate  $n_{FTO}$ , which remains constant during the measurement. The pre-factor 2 comes from the fact that the spatial extension of the contact is supposed to be negligible so that the distance from the middle of the slice in contact with the substrate to the substrate is  $\delta z/2$ . The current which is simulated as the photocurrent transient is  $J_{nc}$ .

#### 4.4.1.7 The RC contact

For the RC contact it is assumed that electrons leave the FTO substrate either through a measurement resistor  $R_m$ , which can be the input resistance of the scope or an external measurements resistor over which the transient is measured. Additionally electron can leave the FTO substrate by recombination into the electrolyte.

$$J_{RC} = \frac{U_{FTO}}{R_m} \quad \text{with} \quad U_{FTO} = -\frac{q(n_{FTO} - n_0)A\delta z_{FTO}}{C_{FTO}} \quad (4.12)$$

$U_{FTO}$  is the electrostatic potential of the FTO contact,  $n_0$  is the electron density in the FTO contact at thermal equilibrium,  $A$  is the surface area of the slices and  $\delta z_{FTO}$  is the thickness of the FTO slice. The capacitance of the FTO substrate is denoted with  $C_{FTO}$  and, for an experimental system where the FTO substrate is in direct contact with the electrolyte,  $C_{FTO}$  can be approximated by the Helmholtz capacitance at the FTO/electrolyte interface,  $C_{HL}$ . One can see that the calculated transient current  $J_{RC}$  depends on the RC constant,  $R_m \cdot C_{HL}$ , which is defined by the contact. In contrast to the numerical contact the electron concentration  $n_{FTO}$  does not remain constant during the measurement in the RC contact. The electron concentration inside the contact at time step  $t_k$  is defined as

$$n_{FTO}(t_k) = n_{FTO}(t_{k-1}) + \left( \frac{J_{nc}}{-q} - \frac{J_{RC} + J_{FTO}^R}{-qA\delta z_{FTO}} \right) (t_k - t_{k-1}) \quad (4.13)$$

where  $n_{FTO}(t_{k-1})$  is the concentration from the previous time step.  $J_{nc}$  is the current into the contact (eq. 4.11) while  $J_{RC}$  is the current leaving the contact.  $J_{FTO}^R$  is a recombination current from the FTO substrate into the electrolyte, which is a function of  $U_{FTO}$  and can, furthermore, be a function of the density of positive charges in the electrolyte in contact with the FTO substrate. For the simulations presented below the recombination current was defined as

$$J_{FTO}^R = -qk_{nc}U_{FTO} \quad (4.14)$$

where  $k_{nc}$  is the rate constant for electron transfer from the FTO substrate into the electrolyte. In contrast to the recombination current inside the  $TiO_2$  structure, defined by eq. (4.9), which depends on the excess electron concentration ( $n_i - n_0$ ), it seems to be more reasonable to link the contact recombination to the applied bias  $U_{FTO}$ , because the energy levels of the electronic states, which are relevant for the recombination, are shifted in energy space by  $U_{FTO}$ . In a more general approach  $k_{nc}$  might depend on  $n_{FTO}$  and  $U_{FTO}$ . However, a constant  $k_{nc}$  suffices to point out the importance of the contact properties.

The parameters which were used for the following calculations, such as  $TiO_2$  thickness, slice thickness, etc. are summarized in Appendix A. For all calculations an optical absorption constant of  $\alpha = 10^5 \text{ cm}^{-1}$  was taken to assure that nearly all charge carriers are generated within a narrow part of the mesoporous structure at the electrolyte side. To be able to compare simulated photocurrent transients, presented in the following sections, with the experimentally measured data, presented above, both sets are analyzed in the same way. This means that the transient peak time is extracted from the simulations, which is subsequently used to calculate an effective diffusion constant according to eq. (4.2). Differences between the value for the diffusion constant, used as input parameter for the simulations, and the values of  $D_e$ , derived from the calculated transients, are discussed in chapter 5.

#### 4.4.2 Simulations I: Dispersive transport without recombination

To investigate the origin of the experimentally observed shift of the transient peak time,  $t_p$ , as a function of the applied potential (section 4.3.1), of the illumination intensity (section 4.3.2) and of the pH value of the electrolyte (section 4.3.3), the corresponding photocurrent transients were simulated and compared to the results obtained from experiments. These results indicate that the diffusion becomes dispersive and this effect is investigated in a more quantitative fashion in this section. For the simulations it was assumed that recombination is negligible and that the effective diffusion coefficient can be described by eq. (4.7a & b). The FTO/TiO<sub>2</sub> interface was mathematically described by the numerical contact, eq. (4.11).

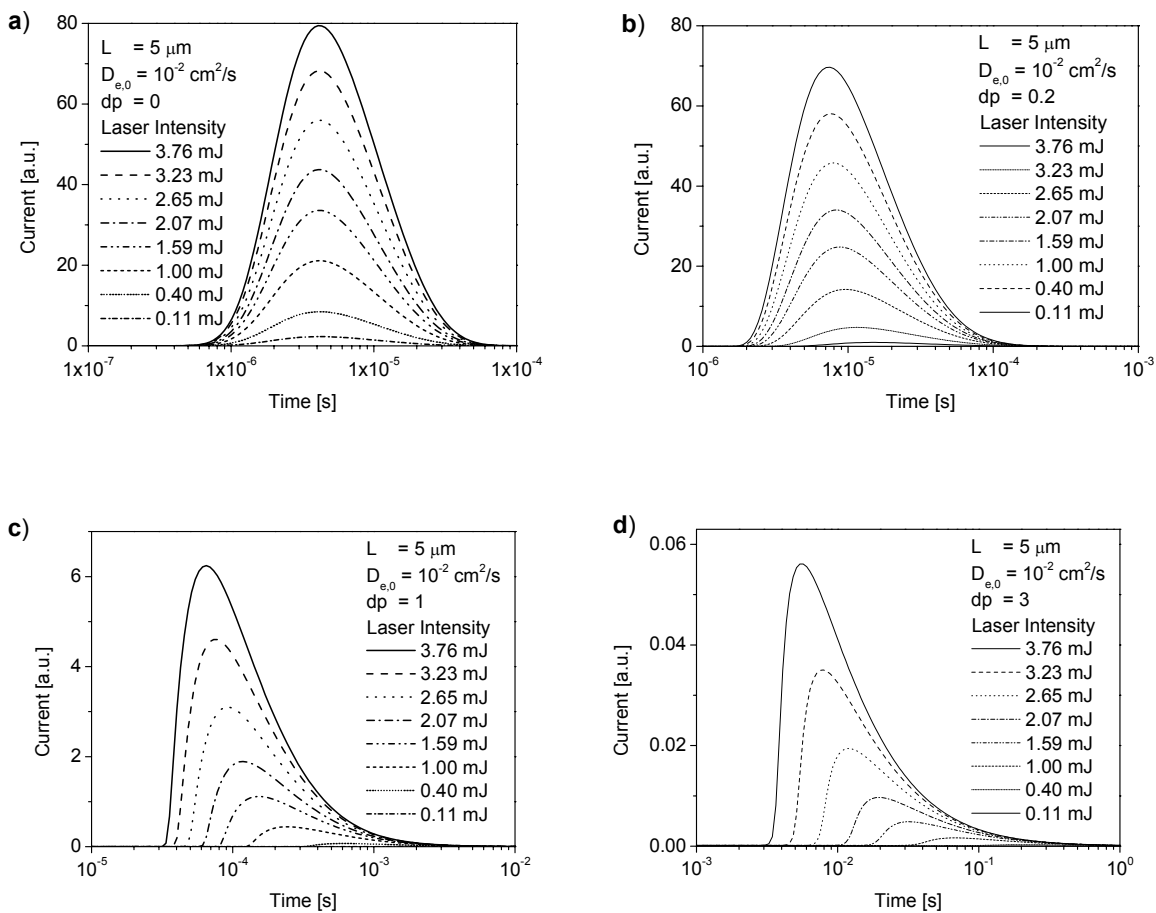


Figure 4.16: Simulated photocurrent transients calculated with the parameters given in the plot for different light intensities with (a) without dispersive transport ( $dp = 0$ ). (b) With a dispersion parameter ( $dp$ ) of 0.2, (c)  $dp = 1$  and (d)  $dp = 3$ . The complete set of input parameters, used for the simulations, is given in Appendix A.

Photocurrent transients for different dispersion parameters  $dp$  were simulated as a function of the incident laser intensity. Figure 4.16a shows a set of transients for a  $5\ \mu\text{m}$  thick film with a diffusion constant of conduction band electrons of  $10^{-2}\ \text{cm}^2/\text{s}$  without dispersion ( $dp = 0$ ) while Figure 4.16b show the same calculation with  $dp = 0.2$ . Recombination was not included into the simulations so that electrons were only able to leave the  $\text{TiO}_2$  film through the FTO substrate. From the plots one can see that  $t_p$  shifts slightly towards shorter times with increasing light intensity and that the photocurrent rises and decays between  $10^{-6}$  to  $10^{-4}$  seconds. Figure 4.16c & d show calculations with the same set of input parameters as in Figure 4.16a, but with a dispersion parameter of 1 and 3, respectively. One can see that the transients are more asymmetric and that the transient onset occurs around  $10^{-2}$  seconds while the decay tail extends up to 1 second. This is roughly 4 orders of magnitude slower than what results from the previous simulations, even though the same conduction band electron diffusion constant  $D_{e,0} = 10^{-2}\ \text{cm}^2/\text{s}$  was used. Simulated transients with  $dp = 0.5$  and 2 (not depicted) show a gradual increase in the peak asymmetry as well as a shift towards longer transient times with increasing  $dp$ .

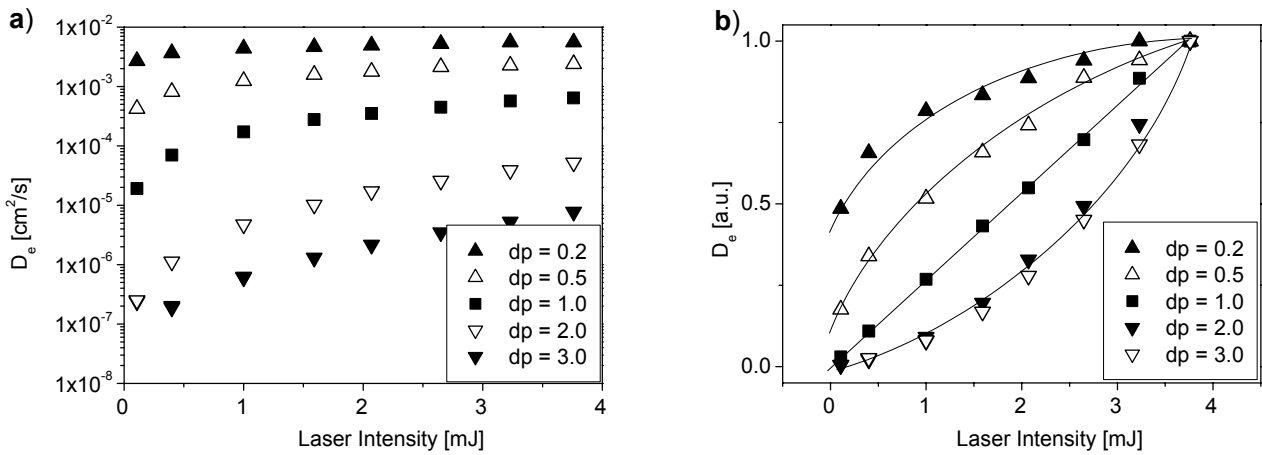


Figure 4.17: (a) Diffusion coefficients calculated from the transient peak time according to eq. (4.2) at different illumination intensities and for different dispersion parameters. (b) As (a) but on a linear scale with the diffusion coefficients normalized to the value at maximum light intensity (3.76 mJ/pulse for each  $dp$  value).

The transient peak time  $t_p$  was extracted from the simulations and the effective diffusion constant for each transient was calculated according to eq. (4.2). These diffusion coefficients are depicted on a logarithmic scale in Figure 4.17a as a function of illumination intensity for different dispersion parameters. One remarkable result is that the diffusion constant, as calculated from the transient peak time  $t_p$ , varies by 5 orders of magnitude, depending on the dispersion parameter. This shows that the trap distribution in energy space is of particular importance for the description of the time-resolved electron transport in mesoporous TiO<sub>2</sub> films. The diffusion constant furthermore increases with increasing laser intensity which is in agreement with experimental observations (Figure 4.10).

#### 4.4.3 Determination of $D_e$ from thickness-dependent measurements

The diffusion coefficient of electrons in mesoporous TiO<sub>2</sub> structures has been derived in the literature from photocurrent transients, which were measured as a function of the TiO<sub>2</sub> film thickness.<sup>59</sup> If the squared film thickness,  $L^2$ , is plotted versus  $6t_p$  one can derive the diffusion coefficient from a linear fit. To check the validity of the dispersive transport, as defined in eq. (4.7), it should be possible to derive a diffusion constant from simulated  $t_p$  data, which were calculated for different film thickness. The film thickness as function of  $t_p$ , which was derived from simulations for a dispersion coefficient of 0.2 and 1.0, are shown in Figure 4.18a & b, respectively. The first remarkable result is that the data are reasonably located on a straight line. Furthermore the diffusion coefficient, which is derived from the linear fit ( $3.8 \cdot 10^{-3}$  cm<sup>2</sup>/s for  $dp = 0.2$  and  $1.0 \cdot 10^{-4}$  cm<sup>2</sup>/s for  $dp = 1$ ), correlates fairly well with the coefficient derived from a single data point ( $4.9 \cdot 10^{-3}$  cm<sup>2</sup>/s for  $dp = 0.2$  and  $3.5 \cdot 10^{-4}$  cm<sup>2</sup>/s for  $dp = 1$ ). Note that the difference between the  $D_e$  calculated from a single point and from the linear fit is due to the fact that the data point is not located on the linear fit.

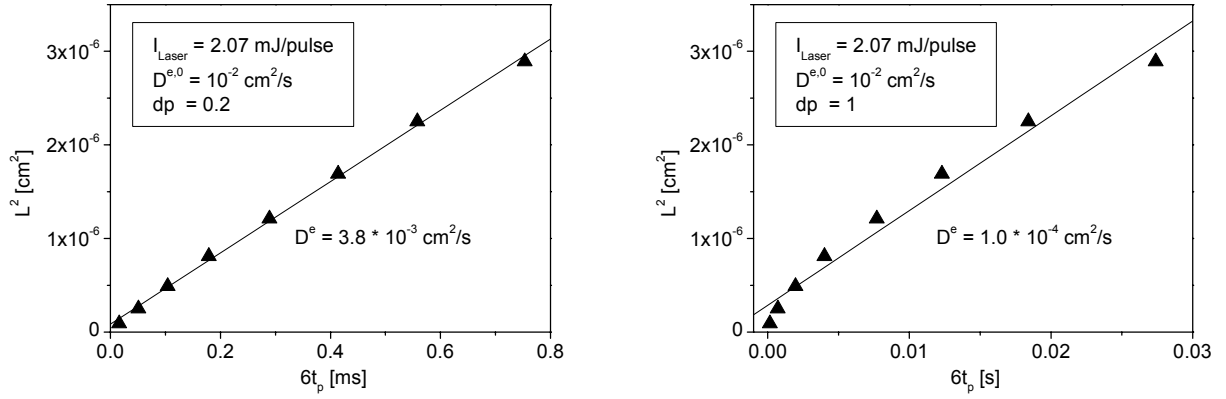


Figure 4.18: (a) Linear fit of the square of the TiO<sub>2</sub> film thickness,  $L^2$  vs.  $6t_p$ . The diffusion coefficient is derived from the slope. The parameters used to simulate the data are given inside the figure. (b) As (a) but with a dispersion parameter of 1, instead of 0.2.

So far all considerations were based on simulations which do not include recombination of electrons from the TiO<sub>2</sub> into the electrolyte. In the next section the influence of the recombination on the transient peak time and, subsequently, on the diffusion coefficient is discussed.

#### 4.4.4 Simulations II: Non-dispersive transport with recombination

Analytical solutions for photocurrent transients usually neglect recombination. The impact of recombination on  $t_p$  and  $D_e$  is investigated in this section, where the electron recombination current depends on the excess electron concentration in the conduction band ( $n_i - n_0$ ), a recombination rate constant  $K_n$  and a recombination parameter  $kp$  as defined by eq. (4.9).

A series of simulated photocurrent transients at different recombination currents in the absence of dispersive transport ( $dp=0$ ) is shown in Figure 4.19a. As the simplest approach it was assumed that the recombination rate depends linearly on the electron concentration ( $kp = 1$ ). One can see that the transient intensity decreases with increasing recombination and that the transient peak shifts towards shorter times.

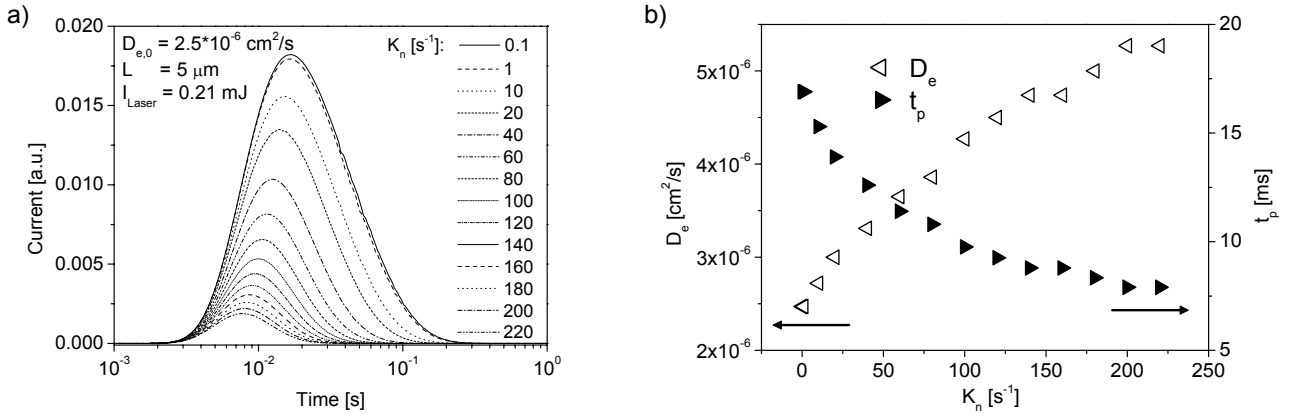


Figure 4.19: (a) Photocurrent transients for a system with a non-dispersive transport ( $dp=0$ ) where the recombination current depends linear on the excess electron density in the  $\text{TiO}_2$ . (b) Transient peak time  $t_p$  (filled triangles) and effective diffusion coefficient  $D_e$  (empty squares) as a function of the recombination rate constant  $K_n$ .

Figure 4.19b shows  $t_p$  and  $D_e$  (calculated according to eq. (4.2)) as a function of the recombination rate constant,  $K_n$ , for different values of the recombination parameter,  $kp$ . A remarkable result is that  $D_e$ , derived from the photocurrent peak time,  $t_p$ , using eq. (4.2), is larger than  $2.5 \cdot 10^{-6}$  cm $^2$ /s and, thus, larger than the ‘real’ diffusion coefficient which was used as an input parameter for the calculations. Only in the limit of very low recombination the derived diffusion coefficient coincides with the real value, which means that the diffusion coefficient is overestimated when eq. (4.2) is applied to experimental systems with strong recombination.

The experimentally observed shift of  $t_p$  with increasing laser intensity (cf. Figure 4.10) is well simulated when dispersive transport is assumed, as shown in the previous section. However the ratio of the simulated transient current maxima does not fit with the experimental observation where the transients seem to converge at high laser intensities. The simulated transients in Figure 4.20a were calculated for a recombination current, which is not linear dependent on the excess electron concentration but has a power law dependence ( $kp = 3$ ). One can see that the transients move closer together for higher illumination intensities. A slight shift of  $t_p$  towards shorter transient times is observed when the peak time  $t_p$  is plotted vs the light intensity (not shown), however this shift is significantly smaller than the experimentally observed shift (see Figure 4.10).

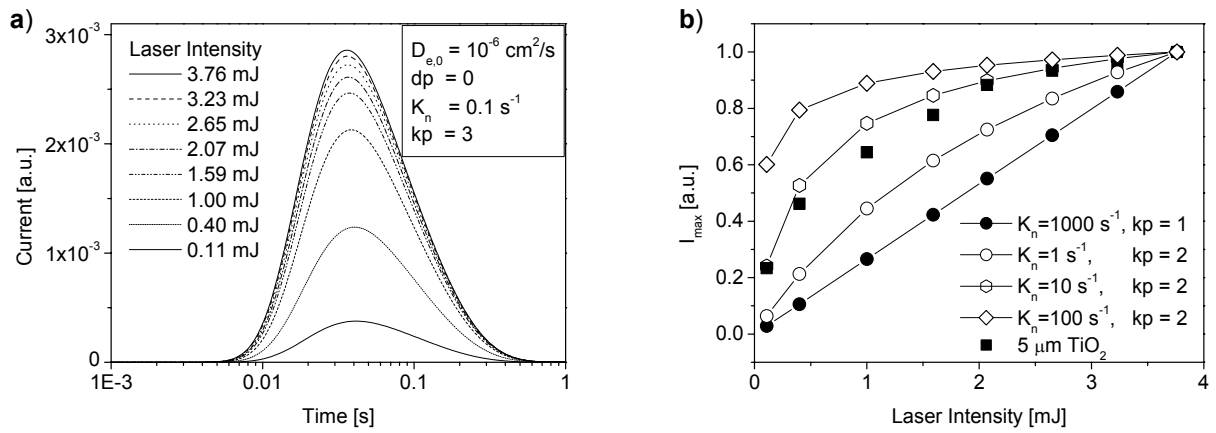


Figure 4.20 (a) Simulated transients for a non-dispersive system with a power law dependent recombination current. (b) Normalized transient current maxima  $I_{max}$  from the measurements shown in Figure 4.10a and calculated results for different recombination exponents  $kp$ .

Figure 4.20b shows the normalized transient current maximum from the measurements of a 5  $\mu\text{m}$  thick  $\text{TiO}_2$  film (shown in Figure 4.10a) and calculated values for different rate constants  $K_n$  and recombination exponents  $kp$ . The maximum current is linear dependent on the light intensity for  $kp = 1$ , independent of the recombination constant  $K_n$ . For  $kp > 1$  the maximum current shows a non-linear intensity dependence and the deviation from linearity increases with increasing  $K_n$ .

#### 4.4.5 Simulations III: Dispersive transport with recombination

In a real experimental system dispersion and recombination are present and Figure 4.21a & b intensity dependent transient series for different input parameters are shown. One can see that the diffusion coefficient  $D_{e,0}$ , the dispersion parameter  $dp$  as well as the recombination rate constant  $K_n$  together with the recombination exponent  $kp$  give more than one possible set of parameters to simulate experimental results.

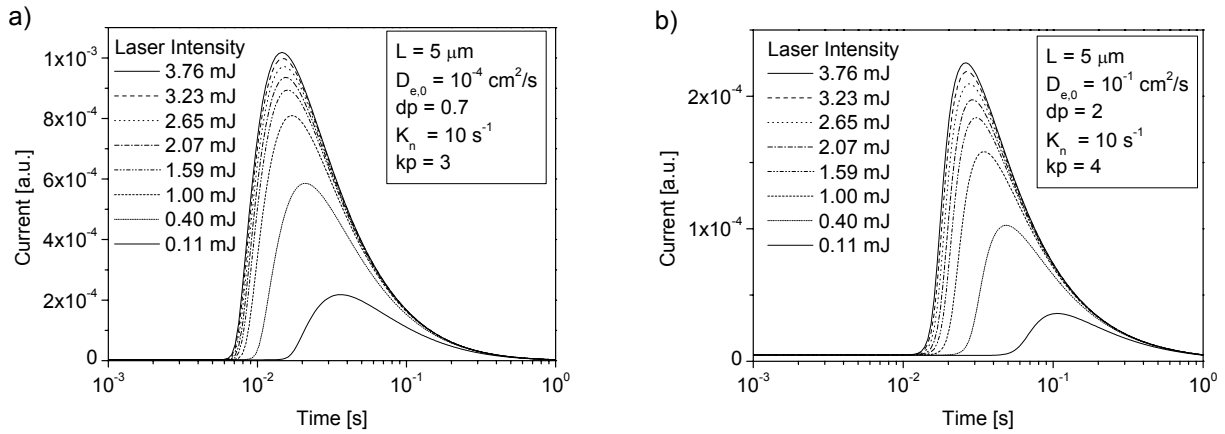


Figure 4.21: Simulated photocurrent transients for different laser intensities, (a) calculated with a dispersion parameter of 0.7, a recombination rate constant of  $10 \text{ s}^{-1}$  and a recombination parameter of 3, and (b) calculated with a dispersion parameter of 2, a recombination rate constant of  $10 \text{ s}^{-1}$  and a recombination parameter of 4.

The transients in Figure 4.21a were calculated with a dispersion parameter smaller than one and a diffusion constant of  $10^{-4} \text{ cm}^2/\text{s}$  while for the calculations in Figure 4.21b the dispersion parameter was chosen to be  $> 1$  with an unreasonable high diffusion constant  $10^{-1} \text{ cm}^2/\text{s}$  for untrapped CB electrons (note that the diffusion constant for bulk  $\text{TiO}_2$  is around  $10^{-2} \text{ cm}^2/\text{s}$ , when calculated from the electron mobility using the Einstein relation ( $\eta_e k_B T = q D_e$ )).<sup>65</sup> A non-linear recombination with a recombination exponent of 3 (Figure 4.21a) or 4 (Figure 4.21b) had to be used to get a reasonable dependence between the transient current and the illumination intensity.

The normalized effective diffusion constants, calculated according to eq. (4.2) from simulated transients (see Figure 4.21), are shown in Figure 4.22 together with the measured data (from transients shown in Figure 4.10). One can see that the curvature of the light dependent diffusion coefficient data points is stronger for the simulated data (triangles) than for the measured results (circles). Furthermore, both simulated curves show the same curvature, even though the dispersion parameter is  $> 1$  (filled triangles) for one set of simulated transients. This is in contrast to simulated results in the absence of recombination, where the diffusion coefficient shows a concave curvature for dispersion parameters  $> 1$  (see Figure 4.17b).

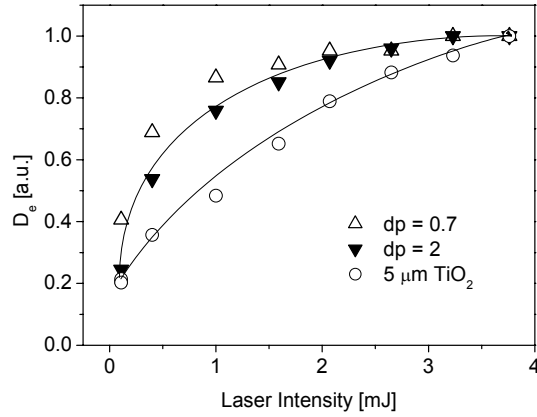


Figure 4.22: Normalized diffusion coefficient as a function of the illumination intensity. The triangles are the simulated data for two different dispersion parameters (for the same dataset like in Figure 4.21). The squares represent measured data on a 5  $\mu\text{m}$  thick TiO<sub>2</sub> film (same data like in Figure 4.10b)

The effect of the recombination rate constant on the transient shape and on  $t_p$  (and the effective diffusion constant  $D_e$ , calculated from  $t_p$  according to eq. (4.2)) is shown in Figure 4.23 for a dispersive diffusion current ( $dp = 1$ ) and a recombination current that depends linearly on the electron concentration ( $kp = 1$ ). One can see that the transient current decreases with increasing recombination rate but that it does not change significantly its shape. Figure 4.23b shows that the transient peak time increases with increasing  $K_n$  which is opposite to the results shown in Figure 4.19b for a system with non-dispersive transport. Simulations with a recombination exponent  $kp > 1$  lead also to an increase in  $t_p$  with increasing  $K_n$  (not shown).

The decrease of the effective diffusion coefficient  $D_e$  with increasing recombination explains the convex curvature of the filled triangles in Figure 4.22b. Electron recombination is much more pronounced at high light intensity, due to the non-linear recombination current which increases by the power of 4 with increasing electron concentration (as defined by eq. (4.9)). Thus, the net recombination is high at high light intensities which leads to an increase in  $t_p$  and, subsequently, to a decrease in  $D_e$  with increasing light intensity. This recombination-induced decrease in  $D_e$ , folded with the concave light intensity-dependent increase in  $D_e$  is the reason for the convex shape of the simulated  $D_e$  data points in Figure 4.22.

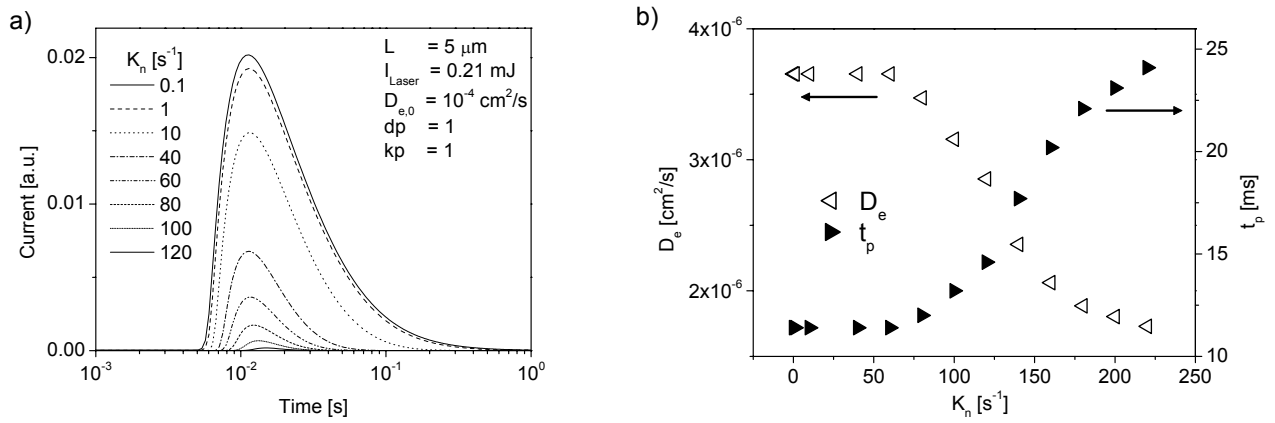


Figure 4.23: (a) Calculated transient current for different recombination rate constants  $K_n$ . (b) Transient peak time (filled triangles) and effective diffusion coefficient (empty triangles) as a function of  $K_n$ .

#### 4.4.6 Simulations IV: The impact of the RC-time constant

The impact of the RC constant on the transient current is shown in Figure 4.24 where transients were simulated with different RC-time constants of the system. Electron recombination as well as dispersive transport was not included into these calculations. One can see that the transients remain nearly unaffected for time constants smaller than 300  $\mu\text{s}$ . Larger time constants cause a decrease of the peak maximum and a shift towards longer transient peak times.

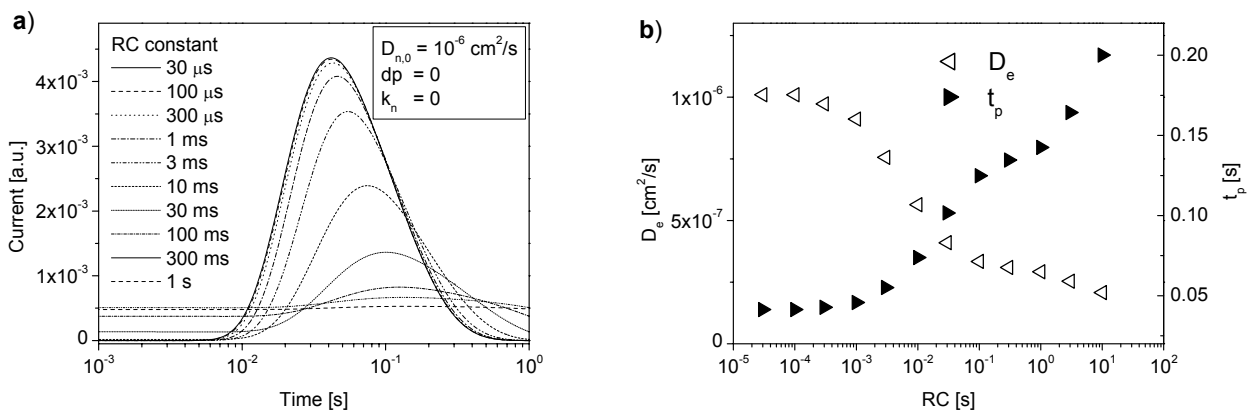


Figure 4.24: (a) Simulated photocurrent transients for different RC time constants, calculated for a system without recombination ( $K_n = 0$ ) and without dispersive transport ( $dp = 0$ ). (b) Transient peak time  $t_p$  and effective diffusion coefficient  $D_e$  as a function of the RC constant for the transients shown in (a).

Figure 4.24b shows the transient peak time  $t_p$  and the effective diffusion coefficient  $D_e$ , calculated from  $t_p$  according to eq. (4.2). One can see that the diffusion coefficient decreases approximately by a factor of five when the  $RC$  time constant goes up to one second. The impact of the  $RC$  time constant on the recorded measurement is reduced when electrons recombine from the  $\text{TiO}_2$  or from the FTO substrate into the electrolyte. Figure 4.25a shows simulated transients, where recombination from the mesoporous film into the electrolyte was included in the calculations. One can see that the shift of the transient peak towards longer transient time is significantly reduced, compared to the transients shown in Figure 4.24. The effective diffusion coefficient calculated from  $t_p$  according to eq. (4.2) is shown in b for a recombination parameter  $kp = 1$  and for two recombination rate constants,  $K_n = 10 \text{ s}^{-1}$  and  $K_n = 100 \text{ s}^{-1}$ . One can see that the derived effective diffusion coefficients remain nearly unaffected for  $RC < 300 \mu\text{s}$ . Above that  $D_e$  decreases until it saturates at  $RC > 100 \text{ ms}$ . A similar effect is observed when electron recombination from the FTO substrate into the electrolyte is introduced into the model (eq. (4.14)) while electron recombination from the  $\text{TiO}_2$  into the electrolyte is set to be zero (not shown).

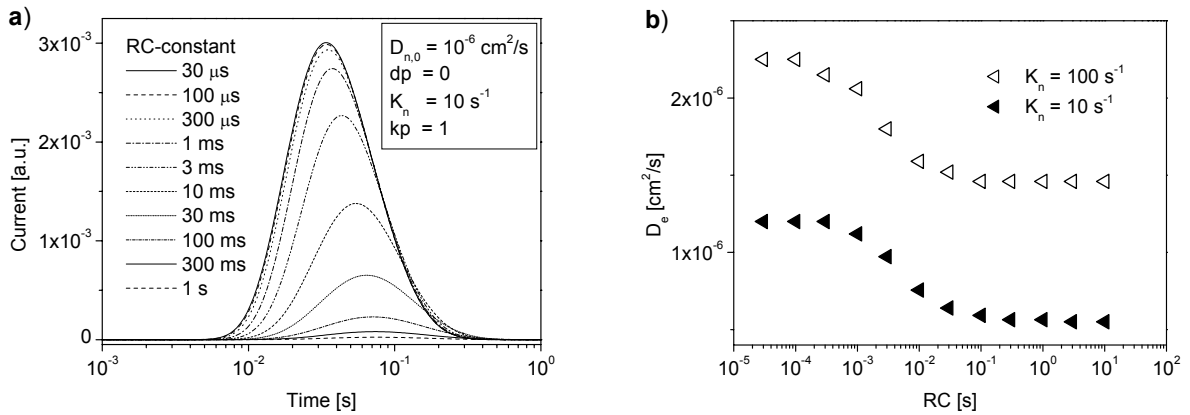


Figure 4.25: (a) Simulated photocurrent transients for different  $RC$  time constants calculated for a recombination rate constant  $K_n = 10 \text{ s}^{-1}$  and a recombination parameter  $kp = 1$ . (b) Effective diffusion coefficient calculated from  $t_p$  according to equation (4.2) for transients with a recombination rate constant  $K_n = 10 \text{ s}^{-1}$  and  $K_n = 100 \text{ s}^{-1}$ .

Comparison of Figure 4.25b with Figure 4.24b shows that the impact of the  $RC$  time constant on the transient response is reduced when recombination is present. The calculations were based on equations (4.12) to (4.14) which consider only a capacitive element of the FTO substrate. Electron accumulation inside the mesoporous  $\text{TiO}_2$  structure was not explicitly considered in terms of capacitive elements. Only the dispersive diffusion coefficient (eq. (4.7)) gave an implicit option to store electrons inside the  $\text{TiO}_2$  film. A second transient peak at very short transient times has been observed in the literature,<sup>59</sup> which was attributed to the  $RC$  response of the system. Such an effect is not supported by the simulations and will be discussed in detail in section 5.1.6, where an alternative explanation will be provided.

The simulations show that the effective diffusion constant which is derived from the transient peak time of the photocurrent transient is affected by recombination and by the  $RC$  time constant of the experimental configuration. Furthermore trap filling can result in dispersive transport which can be described by a diffusion coefficient that is a function of the local electron density, as defined by eq. (4.7). While the latter effect has been mentioned in the literature, the effect of recombination and the contact properties have not been addressed before. A thorough discussion of the results is presented in chapter 5.

## 4.5 Investigation of the $\text{TiO}_2$ /substrate interface

The second major question that was addressed in this thesis is the working principle of DSSCs. In chapter 2 it was pointed out that the electrostatic potential distribution at the FTO/ $\text{TiO}_2$  interface plays a critical role for the DSSC working principle. DSSCs with and without a compact  $\text{TiO}_2$  layer between the mesoporous  $\text{TiO}_2$  film and the FTO substrate are reported in the literature and it is not known how the electrostatic potential distribution looks like for both systems. In section 4.6 a model based on electron tunneling will be introduced for which the electrostatic potential distribution is of particular importance. In this section a detailed investigation of the electrostatic field at the FTO/compact  $\text{TiO}_2$  and FTO/mesoporous  $\text{TiO}_2$  interfaces is presented. To do so,

samples, with and without compact underlayer, were optically excited from the FTO substrate side and photocurrent transients were recorded. In this measurement configuration free carriers (electrons and holes) were generated directly at the FTO/TiO<sub>2</sub> interface and the drift component of the transient current was used to probe the electrostatic field.

#### 4.5.1 Potential-dependent transients

Figure 4.26 shows photocurrent transients at different potentials, measured in a system with a FTO/compact TiO<sub>2</sub> layer. The arrow in the figure marks the time of the laser excitation. At times shorter than 150 ns, the current is superimposed on a noise signal and will not be considered further. At longer times the photocurrent is negative at low and positive at high potentials. The photocurrent transients decay within about 1 ms. The decay is related to transport phenomena like trapping/detrapping as well as recombination. However, here the emphasis will be on the current response at short transient times and the major conclusions are drawn from the sign of the photocurrent. The insert shows the dependence of the current on the applied external potential measured at 200 ns. The slope of the linear fit corresponds to a resistance of 0.57 kΩ, a value that will be discussed in chapter 5.

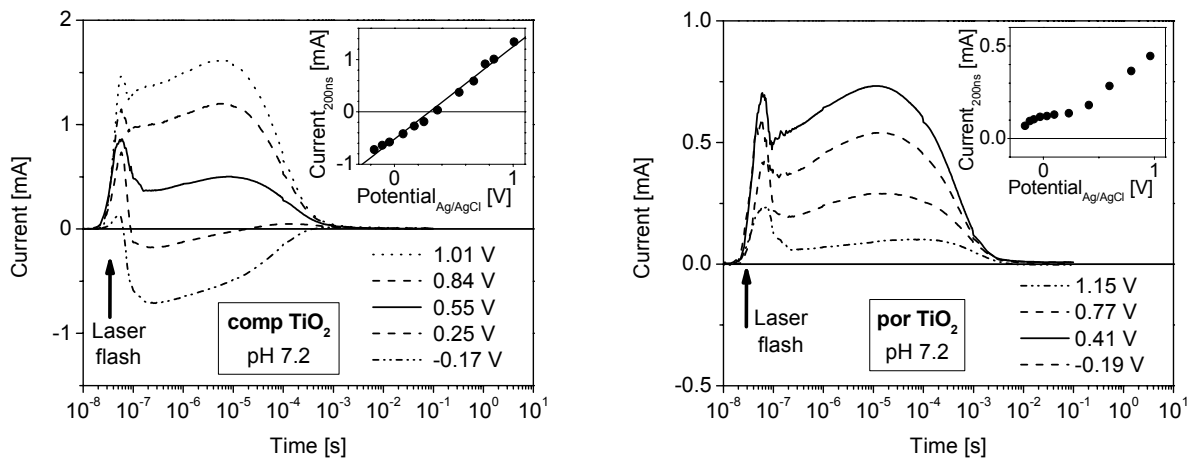


Figure 4.26: (a) Photocurrent transients measured on a compact TiO<sub>2</sub>/FTO sample as a function of an external applied potential vs an Ag/AgCl reference electrode. The insert shows the current, measured at 200 ns, as function of the applied potential. (b) As (a) but measured on a mesoporous TiO<sub>2</sub>/FTO sample.

Photocurrent transients measured on a porous  $\text{TiO}_2$  film at different potentials are presented in Figure 4.26b. In contrast to what is the case for the compact  $\text{TiO}_2$  film, it was impossible to get negative photocurrents. The insert of the figure shows the photocurrent at 200 ns, as function of the applied potential. This shows a linear regime for applied potentials higher than 0.4 V and a non-linear dependence below that.

#### 4.5.2 pH dependent transients

Figure 4.27a shows photocurrent transients, measured on a compact  $\text{TiO}_2$  film at different pH values of the electrolyte. The transients are very similar to those measured at different potentials. At the lowest pH value, a negative photocurrent is observed at 200 ns. The photocurrent increases with increasing pH, similar to the case of increasing applied potential, as shown before. The photocurrent measured at 200 ns depends linearly on the pH value (insert Figure 4.27a) with a slope of approximately 0.1 mA/pH.

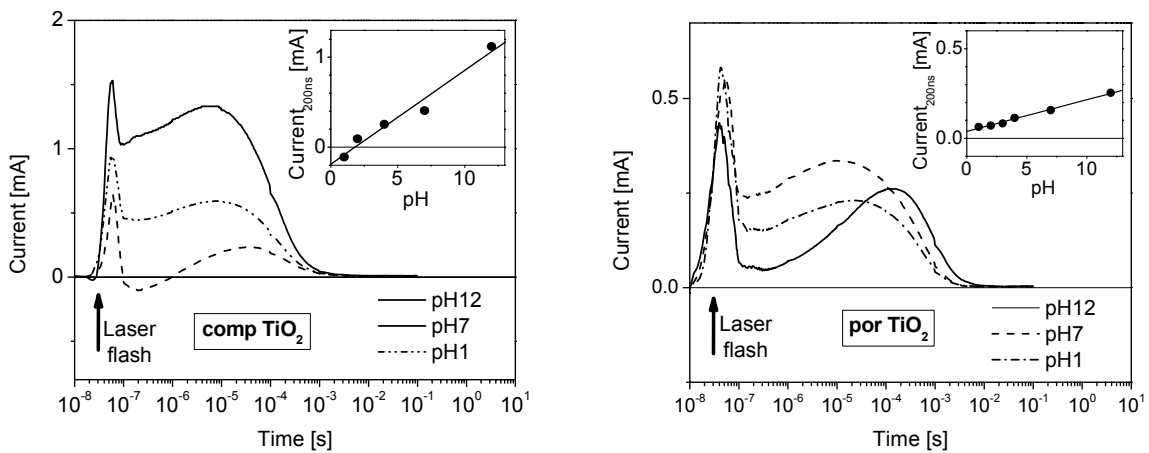


Figure 4.27: (a) Photocurrent transients measured on a compact  $\text{TiO}_2/\text{FTO}$  sample as a function of the solution pH. The insert shows the current, measured at 200 ns, as function of the applied potential. (b) As (a) but measured on a mesoporous  $\text{TiO}_2/\text{FTO}$  sample.

Photocurrent transients measured on a mesoporous  $\text{TiO}_2$  film at different solution pH values are shown in Figure 4.27b. The transient current does not change its sign even at low pH values, similar to potential-dependent measurements on porous films. In contrast to potential-dependent measurements, the transients have a different shape and a shift of the transient peak towards longer times is observed, when the pH value is

increased. The insert of Figure 4.27b shows that the transient current recorded at 200 ns depends linearly on the pH. The slope of the linear fit is 0.02 mA/pH, which is different from that found with a compact TiO<sub>2</sub> layer.

The transient measurements support the concept of electron tunnelling through a barrier at the mesoporous TiO<sub>2</sub>/FTO interface, which will be discussed in detail in chapter 5. This has important implications for the working principle of DSSCs. In contrast to the presented transient measurements, DSSCs are usually based on a non-aqueous electrolyte, so that the surface pH is defined by protons from the adsorbed dye-molecules.<sup>68</sup> Electron tunnelling through an electrostatic barrier at the FTO/TiO<sub>2</sub> interface has been mentioned in the literature<sup>7</sup> but it hasn't been demonstrated that such a barrier can leave the *I-V* characteristics of a DSSC unaffected. In the following section a complete model, based on tunnelling at the mesoporous TiO<sub>2</sub>/FTO interface is derived and in chapter 5 it will be discussed in how far this model can be applied to a DSSC which includes a compact TiO<sub>2</sub> underlayer between the FTO substrate and the mesoporous film.

## 4.6 The tunnel model for dye-sensitized solar cells

In this section a band diagram will be derived, based on CPD data of the FTO substrate and the redox electrolyte, which suggests that an energy barrier is present in the dark at the FTO/TiO<sub>2</sub> interface. This is in contrast to proposed energy band diagrams in the literature (which were reviewed in section 2.2.1, 2.2.2 and 2.2.3). The presence of such a barrier has important implications for the working principle of DSSCs. An analytical expression for electron tunnelling through this barrier will be derived, which is subsequently used for numerical calculations of DSSC *I-V* curves. The impact of the barrier width on the DSSC characteristics will be discussed.<sup>69</sup>

### 4.6.1 Work function and redox potential measurements

The two important parameters to derive an energy band diagram for the DSSC are the work function of the FTO substrate and the redox potential of the electrolyte. The electronic properties of the mesoporous TiO<sub>2</sub> film are not relevant for the derivation of

a band structure, as proposed by the junction model. The  $\text{TiO}_2$  particles are close to intrinsic, so that there are not enough free charge carriers to screen an external electric field. Furthermore, the small size of the nanoparticles results in a high capacitance of the film so that band edge movement can be neglected which will be shown in detail in section 4.6.2. So far it was difficult to get reliable data for the relevant energy levels (FTO work function and  $\text{I}^- / \text{I}_3^-$  redox potential) because the work function of a solid surface and the redox potential of a liquid electrolyte are measured with respect to different reference electrodes. Work functions are measured with respect to the local vacuum level (by UV photoelectron spectroscopy, UPS) or relative to that of a Kelvin probe reference (by contact potential difference measurements, CPD), while redox potentials are measured with respect to an electrochemical reference electrode that can be traced to the normal hydrogen electrode. Several attempts to link the energy scales are reported in the literature but the values scatter by several hundreds of mV.<sup>53,55,70-73</sup>

In this section it is shown that the redox potential of a liquid electrolyte can be measured with a Kelvin probe. To demonstrate the feasibility of the technique the redox potential of the  $\text{Fe}(\text{CN})_6^{3-} / \text{Fe}(\text{CN})_6^{4-}$  couple was measured at different concentration ratios. Figure 4.28 shows the CPD as a function of the decade of the concentration ratios. The solid line shows the linear fit, which has a slope of 54 mV/decade, in good agreement with the predicted slope of 59 mV/decade according to Nernst equation.

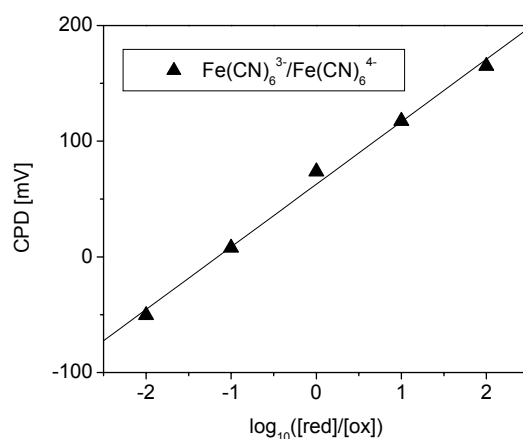


Figure 4.28: Contact potential difference of the  $\text{Fe}(\text{CN})_6^{3-} / \text{Fe}(\text{CN})_6^{4-}$  redox couple, measured in aqueous solution.

It might seem surprising that the Kelvin probe method is capable to measure electrochemical potentials.<sup>74</sup> In general the Kelvin probe measures the contact potential difference between a reference probe and the sample where the potential difference is an *electrostatic potential* difference. For the measurement of a *redox potential* geometric parameters are of particular importance. The measurement requires that the electrolyte is connected to a flat metal back electrode with a surface area as large as or larger than the Kelvin probe. The back electrode has to be in thermal equilibrium with the electrolyte so that the actually measured parameter is the *electrostatic potential* difference between the flat back electrode and the probe.

The Kelvin probe method has been used to measure the CPD between the  $I/I_3^-$  couple dissolved in ACN and the Au probe, as schematically shown in Figure 3.6. For a mixing ratio of 1:10 between the oxidized and the reduced species the CPD is -250 mV which corresponds to a redox potential of 4.75 eV on the solid state scale where the Au work function is taken to be 5.00 eV. The measured work function of the FTO substrate is around 4.85 eV. In the simplest approximation it is assumed that the FTO work function does not change significantly when it is brought into contact with the redox electrolyte (Anderson model).

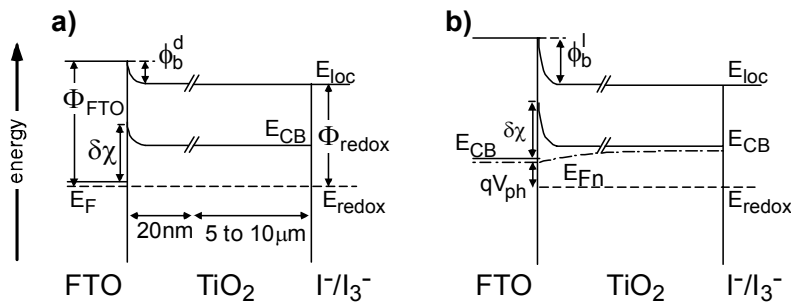


Figure 4.29: (a) Energy band of a DSSC in the dark based on the measured work function data for the FTO substrate ( $\Phi_{FTO}$ ) and the redox electrolyte ( $E_{redox}$ ). The electric field in the dark creates an energy barrier  $\phi_b^d$  at the FTO/TiO<sub>2</sub> interface. (b) Upon illumination the interface barrier  $\phi_b^l$  increases.

For DSSCs it follows that the built-in potential at the FTO/TiO<sub>2</sub> interface is -100 mV, which is in fact a barrier that impedes, rather than promotes electron collection at the FTO contact. An energy band diagram for DSSCs based on the Kelvin probe data is

shown in Figure 4.29 which includes a discontinuity  $\delta\chi$  of  $E_{CB}$  at the FTO/TiO<sub>2</sub> interface, caused by the difference in electron affinity between FTO and TiO<sub>2</sub>. The built-in barrier at the interface is denoted as  $\phi_b^d$ . This barrier actually will increase upon illumination, which is shown in a band diagram in Figure 4.29b at some photovoltage smaller than  $V_{oc}$ . For the derivation of both the band diagrams in the dark and under illumination, it was assumed that band edge movement could be neglected. In the following section it will be shown that this assumption is justified. Furthermore, the origin of the band bending in the mesoporous film at the FTO/TiO<sub>2</sub> interface will be explained.

#### 4.6.2 Band edge movement and band bending in mesoporous TiO<sub>2</sub> films

The band edges of a mesoporous TiO<sub>2</sub> film can move when a significant amount of charge is exchanged between the TiO<sub>2</sub> and the electrolyte to equilibrate the Fermi level with the redox potential. In such case the band edge shift is due to an electrostatic potential drop across a Helmholtz layer at the TiO<sub>2</sub>/electrolyte interface. Furthermore the Fermi level inside the TiO<sub>2</sub> particles shifts if the electron concentration inside the mesoporous structure is changed.

Band edge movement and a chemical potential shift are schematically depicted in Figure 4.30a – f. Figure 4.30a shows a nanoparticle surrounded by electrolyte were the nanoparticle is electrically neutral. The energy band diagram for that case is depicted in Figure 4.30b, where the electron affinity ( $\chi$ ), the chemical ( $\mu_n$ ) and the electrostatic potential ( $\varphi$ ) are depicted. The Fermi level  $E_F$  is in equilibrium with the redox potential  $E_{redox}$  and dipoles at the TiO<sub>2</sub>/electrolyte interface are neglected so that the local vacuum level is constant. Figure 4.30c & d show the situation when electrons are injected into the TiO<sub>2</sub> particle which increases the electron concentration in the CB and thus shifts up the quasi Fermi level. Figure 4.30e & f shows a similar situation with injected electrons located at the particle surface, which causes an electrostatic potential drop at the particle/electrolyte interface across a Helmholtz layer and shifts up the band edges.

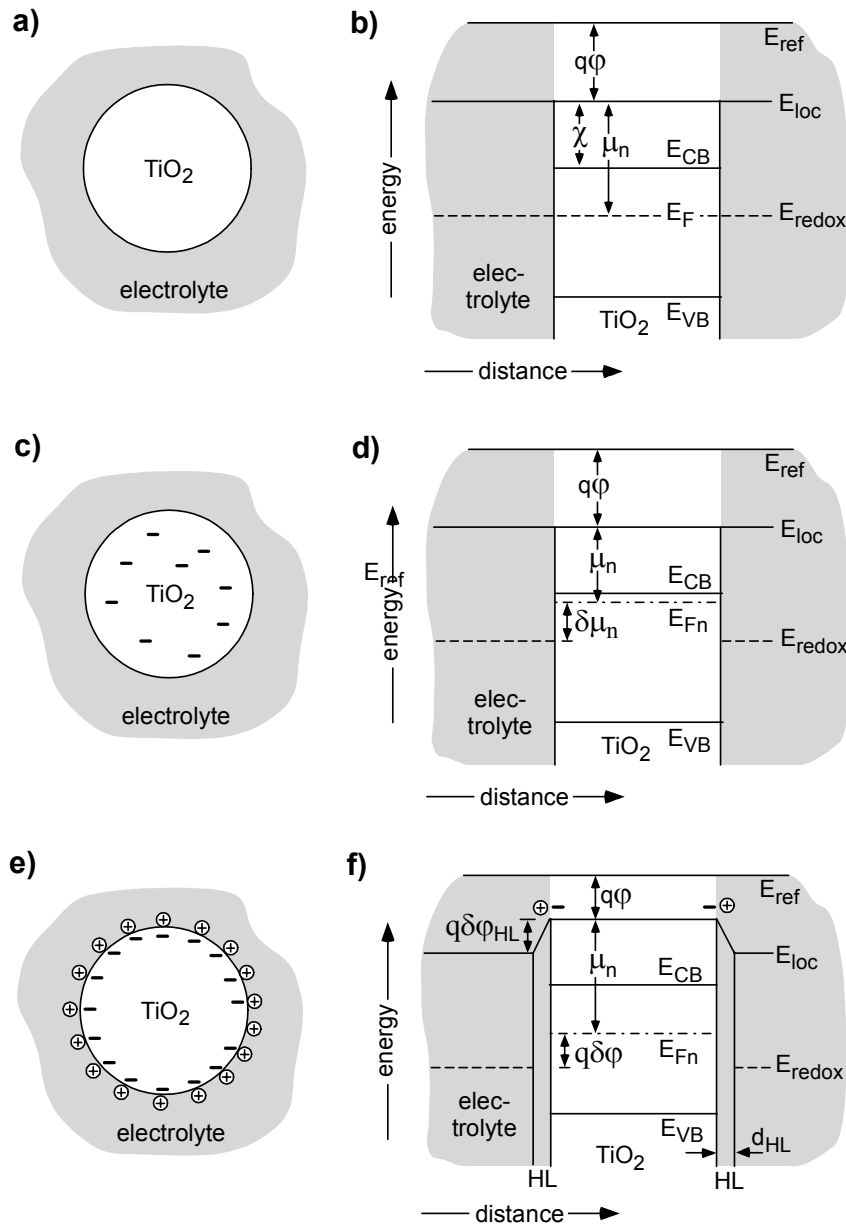


Figure 4.30: (a) Schematic drawing of a spherical  $\text{TiO}_2$  nano-crystal immersed into an electrolyte. (b) Energy band diagram for a nanoparticle in thermal equilibrium with the electrolyte, showing also the electron affinity  $\chi$ , the chemical ( $\mu_n$ ) and the electrostatic potentials ( $\phi$ ), each defined with respect to their reference potential,  $E_{loc}$  and  $E_{ref}$ . (c) Particle after photoinjection of electrons, which are homogeneously spread over the particle. (d) Band diagram, which shows the shift of  $E_{Fn}$  towards the CB, caused by a shift of the chemical potential,  $\delta\mu_n$ . (e) Electron accumulation at the particle surface results in a Helmholtz layer at the interface. (f) Band diagram which shows the band edge movement caused by the Helmholtz layer (HL), where it is assumed that the electrons accumulate in surface states at the quasi-Fermi level.  $d_{HL}$  is the width of the HL and  $\delta\phi_{HL}$  is the electrostatic potential drop across the Helmholtz layer.

In the following the band edge movement and the (quasi) Fermi level change will be estimated as a function of electrons per TiO<sub>2</sub> particle. It will be shown that the chemical potential shift is two orders of magnitude larger than any band edge movement, as long as the density of deep traps is negligible. The potentials, which will be used for the calculations, are defined in section 2.1.1.

### **Band edge movement of mesoporous TiO<sub>2</sub> films in electrolyte**

For the calculation it is assumed that the particle/electrolyte assembly can be approximated as a spherical capacitor, where the width of the Helmholtz layer defines the spacing between the capacitor spheres (Figure 4.30e & f). In reality the nanocrystals are interconnected such that the intersection of interconnected particles has to be subtracted from the capacitance. However, it can easily be shown that the error of this estimation is less than 15% for a mesoporous film with a porosity of ~50%, which is a typical value for films used in DSSCs.

The capacitance of a spherical capacitor is defined by the particle radius  $r$ , which represents the inner sphere, and the distance between the spheres  $d_{HL}$ , which is given by the Helmholtz layer width:

$$C_{HL} = 4\pi\epsilon_0\epsilon \frac{r(r + d_{HL})}{d_{HL}} \quad (4.15)$$

where  $\epsilon_0$  is the permittivity of the free space and  $\epsilon$  is the dielectric constant of the solvent molecules, inside the Helmholtz layer. The electrostatic potential drop across the Helmholtz layer per electron per particle is given by

$$\delta\varphi_{HL} = q/C_{HL} \quad (4.16)$$

with the elementary charge  $q$  on the capacitor spheres. The electrostatic potential drop at the TiO<sub>2</sub>/electrolyte interface is less than 0.3 mV per electron per particle for  $r = 12.5$  nm,  $d_{HL} = 0.14$  nm and  $\epsilon = 5$ . For a band edge shift (electrostatic potential drop at the

TiO<sub>2</sub>/electrolyte interface) of about 10 mV approximately 30 electrons have to be injected into each TiO<sub>2</sub> particle.

At the same time an increase of the electron density in the TiO<sub>2</sub> shifts the chemical potential of electrons towards the CB, which is schematically shown in Figure 4.30c & d. In the following it will be shown that this shift is much more dominant than the band edge movement.

### **The shift of the chemical potential inside the TiO<sub>2</sub>**

For the calculations it is assumed that the number of gap states can be neglected. The chemical potential shifts due to an increase of the electron concentration in the TiO<sub>2</sub>. The shift of the chemical potential per electron per nanoparticle can be calculated according to eq. (2.1). In thermal equilibrium the conduction band is around -4.0 eV on the solid state scale, so that the energy difference between the  $E_{CB}$  and the Fermi level (in the dark:  $E_F = E_{redox} = -4.85$  eV) is around 850 meV. The shift of the chemical potential as a function of the electron concentration in the TiO<sub>2</sub> was calculated for an effective electron mass of  $5.6 m_e$  ( $m_e$  is the mass of a free electron). For one photo-injected electron per TiO<sub>2</sub> particle, the energy difference between the chemical potential and  $E_{CB}$  reduces to 190 meV, which means that  $\delta\mu_e = 660$  meV. This result does not change significantly if gap states are considered which are energetically located close to the CB level

This shows that band edge movement in the dark as well as under cell operation is negligible as long as the number of injected electrons is in the order of 1 to 50 per particle, which is in agreement with experimental observations.<sup>30-32</sup> Furthermore it shows that the shift of the chemical potential is 2 – 3 orders of magnitude bigger than the band edge movement (electrostatic potential shift), such that the band edge shift can be neglected.

### **Band bending in mesoporous TiO<sub>2</sub> films**

Another phenomena caused by photo-induced charge redistribution is band bending. The bending can be simply estimated by the density of excess charge within in a single TiO<sub>2</sub> particle. For a quick estimate it can be assumed that this charge is homogeneously

spread, which leads to a band bending of 2.3 meV per excess electron per particle (taking  $\epsilon = 50$  [75] as a dielectric constant of  $\text{TiO}_2$ ). This shows that band bending due to charge accumulation within the mesoporous film is negligible.

Nevertheless, band bending of several hundreds of mV can occur even within a single  $\text{TiO}_2$  particle in the presence of an external field. External fields cannot be screened effectively inside the  $\text{TiO}_2$  because of an insufficient number of free carriers. Thus strong band bending exists at the FTO/ $\text{TiO}_2$  interface, where a strong electric field exists across the Helmholtz layer at the FTO/electrolyte interface. The spatial distribution of the electrostatic potential at the FTO/ $\text{TiO}_2$  interface is analyzed in the following section.

#### **4.6.3 The electrostatic potential distribution at the mesoporous $\text{TiO}_2$ /FTO interface**

The spatial distribution of the electrostatic potential inside the first layer of  $\text{TiO}_2$  particles in contact with the FTO substrate is of particular importance in the presence of an electrostatic barrier for electron transfer from the  $\text{TiO}_2$  into the FTO. When tunneling is considered, the barrier has to be sufficiently small. In contrast to the junction model (section 2.2.2) a somewhat more realistic structure was used (Figure 4.31a) and not the simplified  $\text{TiO}_2$  rod geometry which is shown in Figure 2.7a.<sup>6,25,34</sup> The Laplace equation inside the  $\text{TiO}_2$  nanocrystals was solved under the boundary conditions of a constant electrostatic potential at the  $\text{TiO}_2$  surface in contact with the electrolyte (a potential that differs from the constant potential of the FTO substrate), and a potential drop across the Helmholtz layer at the FTO/electrolyte interface. Figure 4.31a shows the electrostatic potential distribution (equi-potential lines) inside the first two layers of  $\text{TiO}_2$  particles in contact with the FTO substrate for a particle diameter of 25 nm, an interface diameter at the contact area with neighboring particles or the FTO substrate of 15 nm and a Helmholtz layer width of 1.4 Å (see Figure 4.31a, insert).

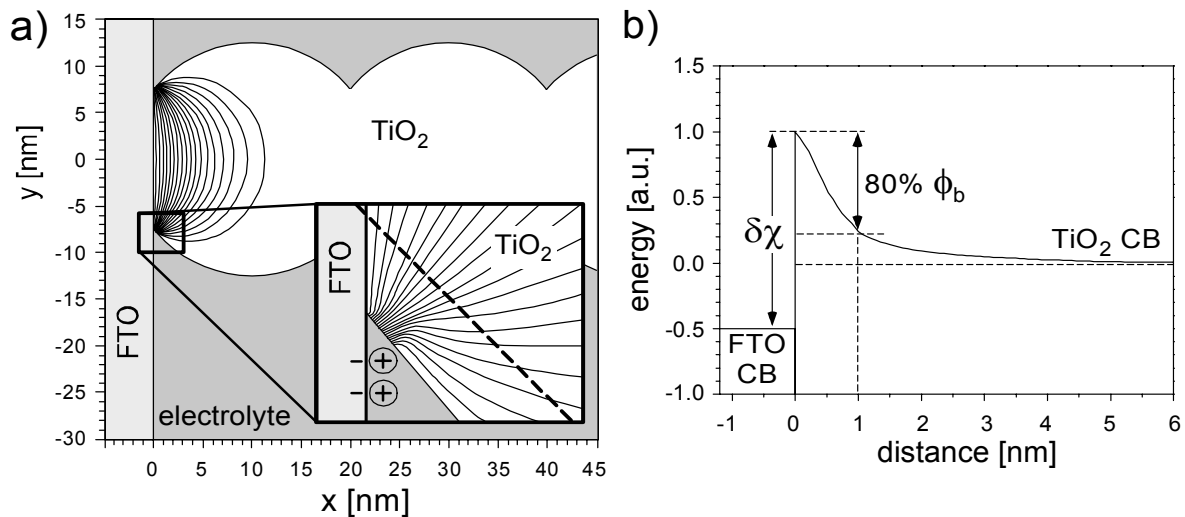


Figure 4.31: (a) Calculated electrostatic potential distribution at the FTO/TiO<sub>2</sub>/electrolyte interface, shown by equipotential lines within the first two layers of particles at the interface. The insert shows the magnification of the interface region including the Helmholtz layer at the FTO/electrolyte interface. (b) Calculated electrostatic potential distribution along the dotted line from the insert in (a) shown as bending of the CB.

From Figure 4.31a it can be seen that the entire potential drop appears within the first layer of TiO<sub>2</sub> particles in contact with the FTO substrate while, already all through the second layer of particles, the potential is that of the electrolyte. The electrostatic potential as a function of the distance from the FTO substrate along the dashed line, close to the three-component FTO/TiO<sub>2</sub>/electrolyte interface (see Figure 4.31a, insert), is plotted in Figure 4.31b. It shows that 80% of the potential drop appears over a distance of about 1 nm, while the potential drop in the center of the particle appears over several nm, as can be seen from the equi-potential lines in Figure 4.31a. Thus, efficient electron tunneling is only considered at that part of the FTO/TiO<sub>2</sub> interface that is close to the electrolyte, where the barrier width is sufficiently thin. In the calculations presented below this was taken into account by an effective interface area, smaller than the geometric interface area.

#### 4.6.4 Electron tunneling at the metal/barrier/TiO<sub>2</sub> interface

An analytical expression for tunneling through an asymmetric barrier between two metal contacts is used to derive an extended expression for the specific case of a semiconductor/barrier/metal interface. Even though the FTO substrate is a degenerate

semiconductor and not a metal, it will be treated in this context as a metal due to its high conductivity. The tunnel barrier is represented by that part of the TiO<sub>2</sub> film at the interface, where the bands are bent because of the electrostatic potential difference between the FTO substrate and the electrolyte. For the analysis the shape of the real tunnel barrier (shown in Figure 4.31b) is simplified to a triangular barrier of constant thickness, shown in Figure 4.32c.

For a trapezoidal barrier, connected between two metal contacts *M1* and *M2*, the tunnel current is given by:<sup>d,76,77</sup>

$$J_t = A \left[ \bar{\varphi}_1(U) \exp(B\sqrt{\bar{\varphi}_1(U)}) - \bar{\varphi}_2(U) \exp(B\sqrt{\bar{\varphi}_2(U)}) \right] \quad (4.17)$$

with constants  $A = \frac{q}{2\pi\hbar\beta s^2}$  and  $B = \frac{-4\pi\beta s\sqrt{2m_e^*}}{h}$ , which contain Planck's constant

$h$ , the elementary charge  $q$ , the barrier width  $s$ , the effective electron mass  $m_e^*$  and a correction factor  $\beta$ , which is close to one so that it will be neglected in the following. The first term in equation (4.17) contains an average barrier height  $\bar{\varphi}_1(U) = (\phi_1 + \phi_2 - qU)/2$  and describes the current from metal contact *M1* into *M2*, while the second term describes the current from *M2* into *M1* with an average barrier height  $\bar{\varphi}_2(U) = (\phi_1 + \phi_2 + qU)/2$ , which is schematically depicted in Figure 4.32a & b at thermal equilibrium and at applied bias, respectively. Equation (4.17) is based on the WKB approximation and the simplification of the real barrier shape by an average barrier height  $\bar{\varphi}$ .<sup>77</sup>

The TiO<sub>2</sub> band edge positions are introduced into the energy diagram to extend eq. (4.17) to the situation of an FTO/barrier/TiO<sub>2</sub> interface, where it is assumed that only CB electrons participate in the tunnel process. Electron transfer from TiO<sub>2</sub> gap states

---

<sup>d</sup> Eq. (4.17) was derived for  $T = 0$  K. A closed form expression for tunnel currents for  $T > 0$  has been presented in the literature for systems with thermally activated electrons, distributed closely around the Fermi level. The difference between the tunnel current at absolute zero and room temperature is less than 5 % for electron barrier widths of about one nanometer (ref. 76) which we consider, so that the tunnel current expression at absolute zero was used, for the sake of simplicity.

into the FTO or *vice versa* is neglected, as shown schematically by the crossed-out arrows in Figure 4.32c.

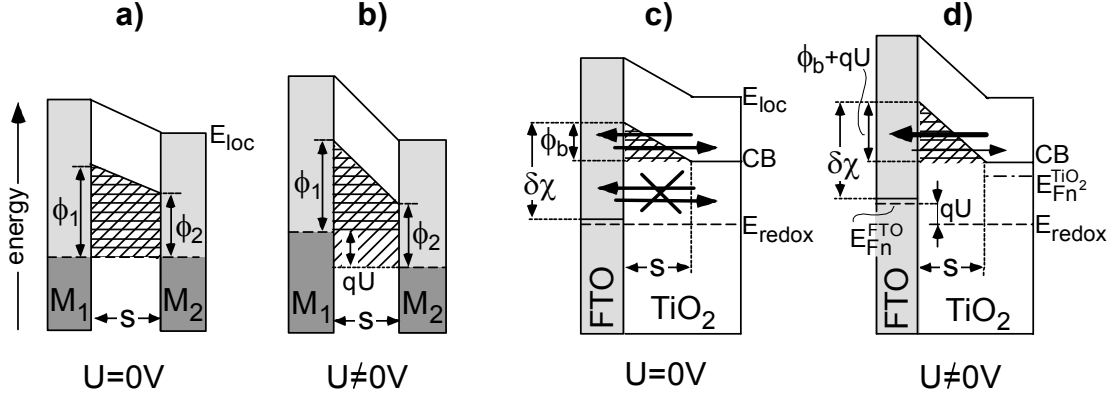


Figure 4.32: (a) Energy band diagram for a tunnel barrier of thickness  $s$  between two metal contacts  $M_1$  and  $M_2$  of different work function at zero bias. (b) Like (a) at negative applied bias to  $M_1$ . The diagonal hatched area shows the barrier for electron tunneling from  $M_2$  into  $M_1$  while the horizontal hatched area shows the barrier for electron tunneling in the reverse direction. (c) Triangular barrier for the FTO/ $\text{TiO}_2$  interface where conduction through electronic gap states is excluded (crossed-out arrows). (d) Like (c) upon cell operation. The tunnel barrier for electron injection into the FTO is equal to the barrier for electron transfer from the FTO into the  $\text{TiO}_2$ . A net current into the FTO is observed due to the difference in  $E_{Fn}$  of the  $\text{TiO}_2$  and the FTO substrate.

From Figure 4.32c & d one can see that the accessible barrier for electron tunneling reduces to a triangle so that the average barrier height for electron tunneling from the FTO into the  $\text{TiO}_2$  is identical with the barrier height for electron tunneling from the  $\text{TiO}_2$  into the FTO. The equation for the tunnel current through an FTO/barrier/ $\text{TiO}_2$  interface can be written as

$$J_t = C A \bar{\varphi}(U) \exp(B\sqrt{\bar{\varphi}(U)}) \left[ \exp\left(\frac{\delta\chi - \phi_b + qU}{k_B T}\right) - \exp\left(-\frac{E_{CB} - E_{Fn}}{k_B T}\right) \right] \quad (4.18)$$

where the potential-dependent average barrier height is given by  $\bar{\varphi}(U) = (\phi_b + qU)/2$  with the built-in potential barrier  $\phi_b$ , as shown in Figs. 4.31b and 4.32c & d. It is emphasized that this built-in field has a polarity opposite to that proposed by the junction model (section 2.2.2). The scaling factor  $C$  takes into account that electron tunneling is only relevant in that part of the FTO/ $\text{TiO}_2$  interface area close to the electrolyte, where the electrostatic barrier is relatively thin. The first term in the square

brackets is the Boltzmann factor that describes the probability to have thermally activated CB electrons in the FTO at the bottom of the barrier, while the second term describes the probability to find electrons in the TiO<sub>2</sub> CB. Upon cell operation the difference between the forward (from the TiO<sub>2</sub> into FTO) and backward current (from the FTO into the TiO<sub>2</sub>) is caused by the difference in the Boltzmann factors in the TiO<sub>2</sub> and the FTO, in contrast to what is the case for the tunnel current at metal/barrier/metal interfaces, where that difference is due to a difference between the tunnel barrier for back- and forward currents.

#### 4.6.5 Simulated $I$ - $V$ characteristics for DSSCs based on the tunnel model

$I$ - $V$  curves were calculated for the same equivalent circuit as the one that was used for the thermionic emission model, which is shown in Figure 2.9. The  $I$ - $V$  characteristics of the barrier diode ( $J_b$ ) are given by eq (4.18), in contrast to the thermionic emission model, with a Schottky diode as a barrier diode. The photo- and recombination currents in the TiO<sub>2</sub>, used for the calculations are defined as

$$J_R = J_0 \left[ \exp\left(\frac{E_{Fn} - E_{redox}}{n_{if} k_B T}\right) - 1 \right] - J_G \quad (4.5)$$

with the same ideality factor  $n_{if}$ , saturation current  $J_0$  and the generation current  $J_G$  as in ref. 26 (the current density at the FTO/TiO<sub>2</sub> junction was scaled according to the effective interface area, in contrast to what was done in ref. 26 where  $J_0$  and  $J_G$  values were chosen to take this area effect into account).

$J_0$	$4 \times 10^{-8} \text{ mA/cm}^2$	$E_{CB}(\text{TiO}_2)$	-4.00 eV
$n_{if}$	1.5	$E_{redox}$	-4.85 eV
$T$	300 K	$\delta\chi$	-0.95 eV
$J_G$	$10 \text{ mA/cm}^2$	$\phi_b^{dark}$	-0.10 eV
$R_S$	$0 \text{ }\Omega\text{cm}^2$	$m_e^*$	$5.6 m_e$

Table 4.2: Parameters used to calculate the  $I$ - $V$  curves shown in Figure 4.33.

$I$ - $V$  curves were calculated with the MATLAB<sup>®</sup> code with the parameters summarized in Table 4.2. The series resistance  $R_s$  was chosen to be infinitely small to emphasize the effect of the tunnel barrier on the  $I$ - $V$  characteristics. Dark and light  $I$ - $V$  characteristics are plotted in Figure 4.33. For the calculations it was assumed that 40% of the geometric FTO area is in contact with TiO<sub>2</sub> particles and 60% is in contact with the electrolyte. Furthermore electron tunneling was only considered at that part of the FTO/TiO<sub>2</sub> interface which is not more than 0.5 nm away from the electrolyte which means that the effective tunnel area per particle is ~13% of the real particle/FTO interface area, so that the scaling factor  $C$  was 0.052.

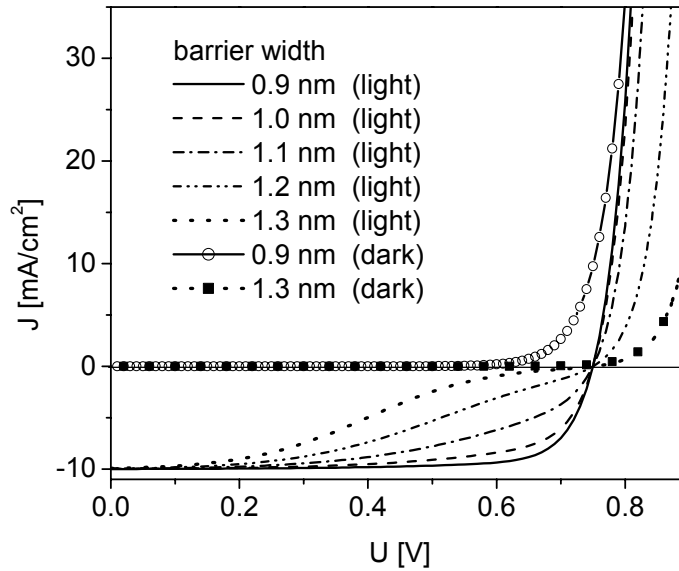


Figure 4.33: Calculated  $I$ - $V$  curves in the dark (line + symbol) and upon illumination (lines) for different tunnel barrier widths. Below a critical barrier thickness the  $I$ - $V$  curve is nearly unaffected and a very reasonable fill factor can be achieved. With increasing barrier width the fill factor decreases and the  $I$ - $V$  characteristics start to show some S-shape.

Figure 4.33 shows that the  $I$ - $V$  characteristics remain unaffected by the tunnel barrier if the CB offset between the TiO<sub>2</sub> and the FTO is 0.95 eV and the width of effective tunnel barrier is 0.9 nm or less. For thicker barriers a decrease in the fill factor is observed and the  $I$ - $V$  curves show some S-shape for barrier widths of 1.2 nm or more. It has to be mentioned that the input parameters for the calculations included estimations,

like the effective tunnel area at the FTO/TiO<sub>2</sub> interface, and that small variations of other parameters (like the energy level of the TiO<sub>2</sub> CB or the dark barrier height  $\phi_b^d$ ) have a strong effect on the tunnel current. It was the aim of the simulations to demonstrate that DSSCs without a built-in field can show high light to electric conversion efficiencies using a reasonable set of material parameters, when electron tunneling is introduced into the system.  $I$ - $V$  characteristics based on thermionic emission at the FTO/TiO<sub>2</sub> interface did not show any significant photocurrent in the external circuit, when calculated with the same set of input parameters (not shown). Therefore the thermionic emission model requires a built-in electric field, which promotes electron transfer from the TiO<sub>2</sub> into the FTO, in contrast to the tunnel-junction model.

## 5 Discussion

In this chapter the molecular effect on the DSSC performance is discussed in terms of a dipole induced band edge movement and molecular induced trap passivation (section 5.1). The effect of trap states and recombination on the electron transport was investigated in more detail with photocurrent transient measurements. Comparison of simulated with experimental data shows that photocurrent transients can be used to analyze the trap state distribution qualitatively (section 5.2). It is shown that the surface pH of the mesoporous TiO<sub>2</sub> structure has a huge impact on recombination and the effect of recombination on the transient current is discussed (section 5.3). The experimentally observed impact of the FTO/TiO<sub>2</sub> interface on the transient response gave rise for more detailed investigation of this interface. Analysis of the electrostatic potential distribution shows a significant difference between mesoporous TiO<sub>2</sub>/FTO and compact TiO<sub>2</sub>/FTO interfaces (section 5.4). Transient measurements with an inversed illumination direction (from the glass substrate side) indicate the existence of an electric field across the compact layer while the electrostatic potential drops on a very narrow scale when the mesoporous film is in direct contact with the FTO substrate. This affects the series resistance and contact capacitance of the experimental system which is expressed by the RC time constant (section 5.4). The electrostatic potential distribution at the TiO<sub>2</sub>/FTO interface is furthermore essential for the tunnel-junction model, which was developed for DSSCs without compact underlayer. An extension of this model to DSSC with compact layer is discussed in section 5.5.

### 5.1 Molecular modification and electron transport

Molecular modification of *p-n* and Schottky junctions, based on Si,<sup>43</sup> GaAs,<sup>45,46</sup> ZnO,<sup>42</sup> and TiO<sub>2</sub><sup>41</sup> is well known from the literature. It has been shown for *p-n* junction cells that the solar cell characteristics can be tuned by organic molecules grafted between the *p*-type and *n*-type material.<sup>40</sup> In this work the concept of molecular modification was applied to DSSCs. It was shown in the previous chapter that molecular modification has a significant impact on the performance of DSSCs, e.g. on the  $V_{oc}$  and  $I_{sc}$ .

Furthermore the resistivity of the mesoporous TiO<sub>2</sub> structure changes if the surface is covered by a molecular monolayer. In the following these effects will be discussed in terms of dipole-induced changes in the band structure and molecule-induced changes in the energy distribution of electronic surface states, which are present in the forbidden band gap of the semiconductor.

### 5.1.1 Solar cell measurements

The molecule-induced change of the  $V_{oc}$  can be explained by a dipole-dependent shift of the TiO<sub>2</sub> conduction band with respect to the redox potential of the electrolyte. Dipole-induced changes of the electron affinity and the work function have been reported in the literature for many semiconductor/molecule/air interfaces<sup>39,78-81</sup> and the dipole related  $V_{oc}$  shift indicates that this concept can be transferred to TiO<sub>2</sub>/molecule/electrolyte junctions. Figure 5.1a shows energy band diagrams for a TiO<sub>2</sub>/molecule/electrolyte interface where the molecular dipole moment is pointing towards the TiO<sub>2</sub> surface (e.g., the methoxy derivative of benzoic or dicarboxylic acid, which has been defined as a negative dipole moment). Figure 5.1b shows a TiO<sub>2</sub> electrolyte interface without interface dipole while Figure 5.1c shows an interface with a positive interface dipole.

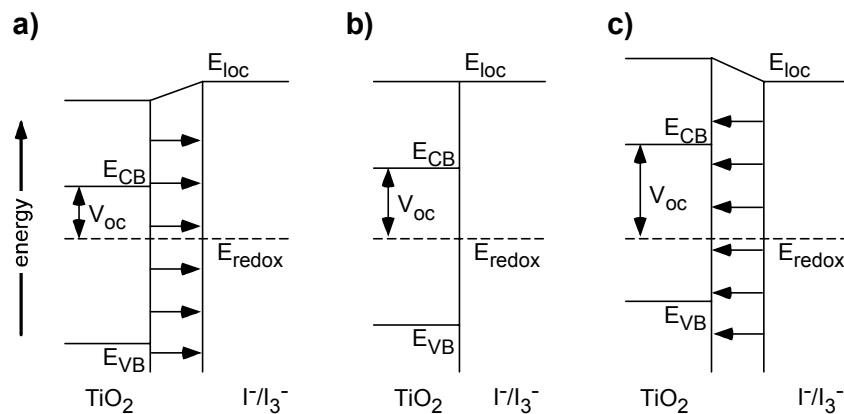


Figure 5.1: (a) Energy band diagram for a TiO<sub>2</sub>/molecule/electrolyte interface containing molecules with a negative dipole moment (e.g., methoxy derivative), which decreases the upper limit of the  $V_{oc}$ . (b) TiO<sub>2</sub>/electrolyte interface without interface dipole. (c) A positive dipole (e.g., cyanide derivative) at the semiconductor electrolyte interface increases the upper limit of the  $V_{oc}$ .

The  $V_{oc}$  is limited by the energy difference between the bottom of the conduction band ( $E_{CB}$ ) and the redox potential of the electrolyte as predicted by the kinetic,<sup>8,82</sup> thermionic emission (section 2.2.1 and 2.2.3, respectively)<sup>9,25,26</sup> and tunnel-junction (see later)<sup>69</sup> models, so that the  $V_{oc}$  decreases in the presence of a positive interface dipole and increases with a negative interface dipole. How efficient  $E_{CB}$  of the  $\text{TiO}_2$  is shifted by the molecular dipole moment can be estimated from the linear trend lines in Figure 4.3a. For the dicarboxylic acid derivatives  $E_{CB}$  is shifted by 5.6 mV per Debye while the benzoic acid derivatives shift  $E_{CB}$  by 8.6 mV/Debye. This difference can be attributed to partial screening of the electrolyte. Ions of the electrolyte penetrate partly into the molecular layer towards the  $\text{TiO}_2$  surface and screen the molecular dipole moment. The dicarboxylic acid derivatives are longer and bulkier and, thus, will pack less well than the smaller benzoic acids. Therefore, the dipole moment of the dicarboxylic acids can be screened better than those of the tighter packed benzoic acids.

An alternative explanation could be a difference in coverage of benzoic and dicarboxylic acid derivatives, due to the different molecular adsorption processes used. This possibility can be ruled out, because of the following argument:

Due to co-adsorption, dicarboxylic acid derivatives occupy binding sites of the dye. As a result dicarboxylic acid / dye molecules ratio is larger than the benzoic acid / dye one, because the benzoic acids primarily adsorb in voids between dye molecules, leaving the dye coverage nearly unaffected. Therefore one would expect the benzoic acid derivatives to have less of an effect than the dicarboxylic acid ones, which is in contrast to experimental observation, thus supporting the hypothesis of partial screening.

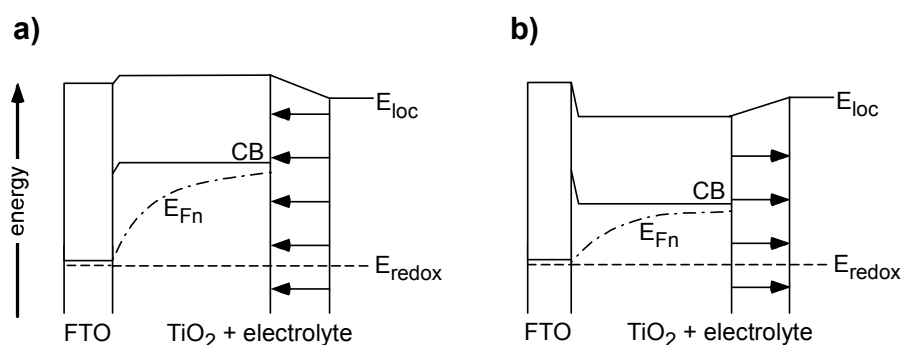


Figure 5.2: Energy band diagram for a DSSC at  $I_{sc}$  for co-adsorbed molecules with (a) a negative dipole moment and (b) a positive dipole moment.

While the effect on the  $V_{oc}$  can be explained by a dipole-dependent shift of  $E_{CB}$ , it is not so obvious why the short circuit current shows similar dipole dependence, as shown in Figure 4.3b. A shift of  $E_{CB}$  towards the local vacuum level, caused by a negative molecular dipole, might change the boundary conditions for the diffusion current in DSSCs at the FTO/TiO<sub>2</sub> interface and, subsequently, improve electron collection, as shown in Figure 5.2a. In contrast, a shift of  $E_{CB}$  towards  $E_{redox}$ , due to a negative molecular dipole at the TiO<sub>2</sub>/electrolyte interface, will decrease the driving force for electron transport towards the FTO substrate. This is schematically shown in Figure 5.2, where the gradient of  $E_{Fn}$  (which is proportional to the photocurrent) is smaller for a positive dipole adsorbed to the TiO<sub>2</sub> surface (Figure 5.2a) than for a negative dipole (Figure 5.2b). This explanation requires that the FTO substrate is significantly less affected by possible adsorption of benzoic or dicarboxylic acids than the TiO<sub>2</sub> surface.

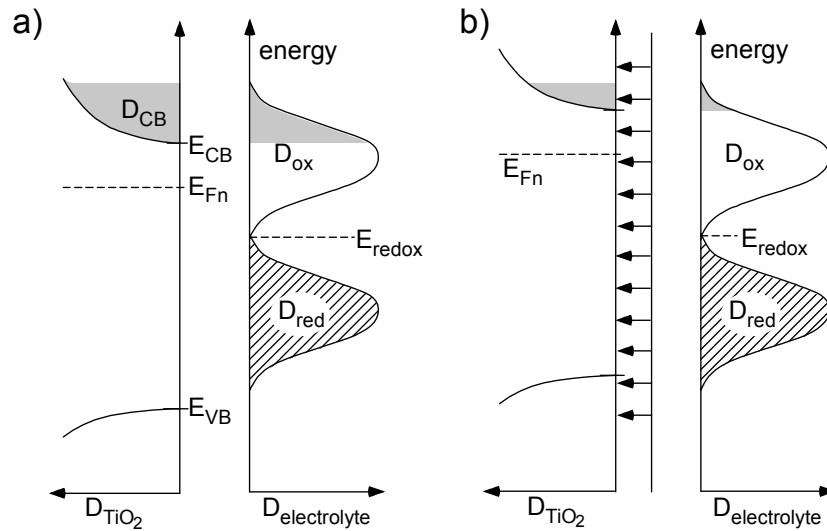


Figure 5.3: (a) Energy alignment of the energy distribution of oxidized ( $D_{ox}$ ) and reduced species ( $D_{red}$ ) of the electrolyte with the energy levels of the TiO<sub>2</sub> conduction band ( $D_{CB}$ ). The grey parts show the energy levels that overlap in energy space and contribute to electron transfer from the TiO<sub>2</sub> into the electrolyte. (b) Decreased recombination due to a smaller overlap of the oxidized species with electronic CB states, caused by the molecular dipole layer.

A different reason for the dipole dependence of the short circuit current might be a dipole-induced shift of the TiO<sub>2</sub> conduction band states with respect to the redox potential. Figure 5.3 shows schematically the density of electronic states at  $E_{CB}$  as a function of energy ( $D_{CB}$ ) and the density of states for the oxidized ( $D_{ox}$ ) and reduced

species ( $D_{red}$ ) of the electrolyte. The recombination current from the  $\text{TiO}_2$  into the electrolyte depends on the energetic overlap of electronic states in the  $\text{TiO}_2$  and the electrolyte,<sup>83-85</sup> shown as grey parts of the density distributions  $D_{CB}$  and  $D_{ox}$ , respectively. A dipole-dependent upward shift of the  $\text{TiO}_2$  energy levels with respect to the redox electrolyte is shown in Figure 5.3b. This decreases the overlap of electronic  $\text{TiO}_2$  states with states of the oxidized species of the electrolyte (again marked in grey), which results in a decreased recombination and, thus, in an increased photocurrent.

Finally it is possible that surface states, which act usually as traps, are passivated or shifted in energy space by adsorbed benzoic or dicarboxylic acids. If this shift of the trap levels depends on the molecular dipole moment it results in a dipole dependent trap distribution and, subsequently, in a dipole-dependent effective diffusion coefficient. Therefore, steady state transport measurements using the bipotentiostat were used to investigate the impact of the molecular dipole moment on the conductivity, as presented in section 4.2.

### 5.1.2 Molecular effect on the conductivity

The measurements presented in section 4.2.1 were performed on mesoporous  $\text{TiO}_2$  films deposited onto interdigitated micro-electrodes. Approaches to perform these measurements with the molecules used for the solar cell modification did not give any trend related to the dipole moment. This was most likely due to experimental problems as will be explained now.

The conductivity measurement technique that I used consisted of two separate potential scans as described in section 4.2, which in turn required a high stability of the experimental system. This could only be achieved in acidic electrolyte of pH 3 or below due to a high parasitic current from the  $\text{TiO}_2$  into the electrolyte. Electron transfer occurs via surface-adsorbed OH groups which trap electrons so that  $\text{OH}^-$  ions are subsequently released into the electrolyte.<sup>66,67</sup> It is likely that at moderate pH values (above pH 3 and below pH 11) this transfer mechanism changes the surface pH and, thus, the energy level of the CB, which finally leads to unstable experimental

conditions during the potential scan. It seemed that in the acid environment the benzoic and dicarboxylic acid derivatives desorbed at negative applied potentials. To circumvent this problem, the mesoporous  $\text{TiO}_2$  structure was electrochemically modified with benzenediazonium-tetrafluoroborate derivatives, which gave a modified  $\text{TiO}_2$  surface that was stable also under the experimental conditions of the measurements. The likely reason is the stronger bond with the surface ( $\text{Ti-O-C}_6\text{H}_6\text{-X}$  vs.  $\text{Ti-O-CO-C}_6\text{H}_6\text{-X}$ ).<sup>49</sup> The functional groups were identical to those of the benzoic and dicarboxylic acid derivatives. Solar cells could not be produced with these pre-modified electrodes because the way they were prepared led to complete surface coverage by the benzenediazonium-tetrafluoroborate molecules, leaving no binding sites for the N3 dye.

In Figure 4.6 one can see that the potential-dependent increase in conductivity has a smaller slope at potentials more positive than  $-0.4$  V compared to more negative potentials. This can be explained by electronic trap states that are present at potentials more positive than  $-0.4$  V. Electron trapping slows down the diffusion process and is mainly responsible for the low conductivity at this potential range. At potentials more negative than  $-0.4$  V these traps are filled and the conductivity increases stronger with negative applied potential, due to the injection of conduction band electrons, which are more mobile than electrons in gap states that move by trapping/detrapping or hopping.

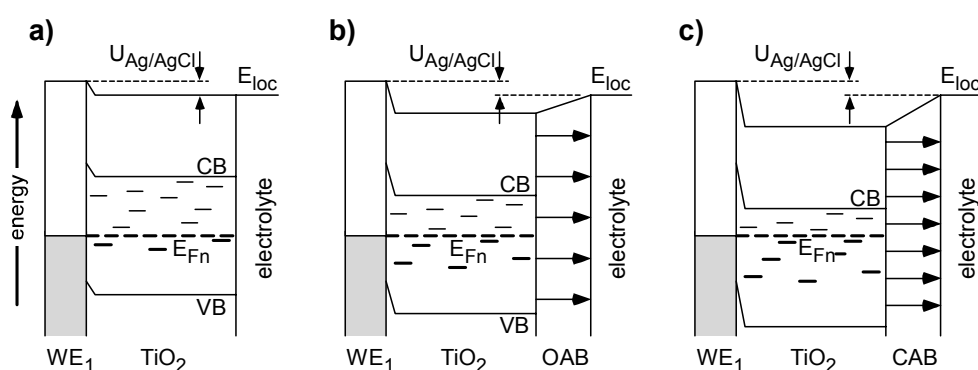


Figure 5.4: Energy band diagrams to explain the dipole related change in the conductivity, shown in Figure 4.6. Diagrams are shown for (a) the unmodified  $\text{TiO}_2$  film in contact with  $\text{WE}_1$  and the electrolyte at a negative applied potential  $U_{\text{Ag/AgCl}}$ . (b) The molecular modified electrode with OAB molecules at the same applied potential. (c) like (b) but with molecules with a more positive dipole moment (CAB).

Figure 4.6 shows furthermore the molecular dipole effect on the conductivity. One can see that molecular modification improves the conductivity, irrespective of the direction of the molecular dipole (CAB, positive; OAB, negative). One possible explanation is the passivation of trap states by the molecules,<sup>38</sup> which furthermore hints that these trap states are located at the TiO<sub>2</sub> particle surface, because this is the place where the molecules interact with the TiO<sub>2</sub>.

An alternative / additional explanation is a shift of the TiO<sub>2</sub> bands with respect to the electrolyte potential, which is depicted in an energy diagram in Figure 5.4. The energy levels of the TiO<sub>2</sub> bands are adjusted with respect to the potential of the electrolyte, which penetrates into the pores of the mesoporous structure of the film. This band alignment depends on the interface dipole at the TiO<sub>2</sub>/electrolyte interface, as shown in Figure 5.4, and, thus, on the molecular dipole moment. The conductivity data shown in Figure 4.6 suggest that the TiO<sub>2</sub> CB is closer to the vacuum level without molecular surface modification than with the modified TiO<sub>2</sub>, if the data are interpreted by a pure band shift. The conduction band is shifted more towards  $E_{redox}$  if the TiO<sub>2</sub> surface is modified with CAB (Figure 5.4b) than is the case with OAB molecules (Figure 5.4c). More traps are filled for the CAB-modified electrode than for the OAB- or unmodified one at the same negative applied potential  $U_{Ag/AgCl}$ , which results in higher conductivity of the CAB modified electrode due to a higher number of saturated traps.

The results from the conductivity measurements are opposite to the results from the results from the solar cell measurements, where higher currents were achieved when the TiO<sub>2</sub> surface was molecularly modified with negative dipoles and lower currents were measured for co-adsorbed molecules with a positive dipole moment. While there is some difference in the chemical binding (Ti-O-CO-R vs. Ti-O-R) the main difference is that in one case the system is optically excited (solar cell measurements) while in the other case the system is measured in the dark (bipotentiostat measurements). In the latter case the quasi-Fermi level is defined by the applied electrostatic potential to  $WE_1$  and  $WE_2$ . For DSSC measurements  $E_{Fn}$  in the TiO<sub>2</sub> is only in equilibrium with  $E_{Fn}$  of the FTO substrate at  $V_{oc}$ ; below  $V_{oc}$  the quasi Fermi level depends on the electron injection rate, the recombination rate and the current into

the FTO substrate, which in turn depends on the gradient of  $E_{Fn}$ . The beneficial effect of an increased  $E_{Fn}$ -gradient has been discussed above for  $I_{sc}$  and is shown in Figure 5.2. These considerations can be extended to voltages below  $V_{oc}$  and, thus, qualitatively explain the trend in the  $I$ - $V$  curves, shown in Figure 4.2. The results from DSSC and bipotentiostat measurements indicate that the gradient effect of  $E_{Fn}$  is more dominant for DSSC operation than the molecule-induced change in the  $\text{TiO}_2$  conductivity.

Because of the high Faradaic current in the baseline scan (without applied potential difference between  $WE_1$  and  $WE_2$ ,  $\Delta U = 0\text{V}$ ) it was not possible to determine the electron concentration inside the mesoporous  $\text{TiO}_2$  structure so that it was impossible to derive a diffusion coefficient from the bipotentiostat measurements. The major reason for the high current seemed to be the fabrication method of the micro-structured gap electrodes. A thin adhesion layer of  $Cr$  or  $Ti$  had to be deposited before evaporation of the electrode metal. Parts of the adhesion layer diffused into the metal electrode and formed an alloy during the sintering step of the mesoporous  $\text{TiO}_2$  film.  $Cr$  and  $Ti$  atoms at the surface were oxidized. The presence of these oxidized metal species increases the catalytic behaviour of the electrode surface.<sup>86,87</sup> As a consequence the loss current into the electrolyte greatly increased for all these measurements, in contrast to what is the case, for example, in the DSSC, where an FTO electrode is used.

## 5.2 Dispersive transport and trap filling

To investigate the impact of electronic trap states on the electron transport in more detail, I performed photocurrent transient measurements. The shift of the transient peak time,  $t_p$ , as a function of the applied bias (Figs. 4.8 and 4.9a), the light intensity (Figure 4.10) or the solution pH (Figure 4.12), strongly indicates that electron transport inside the mesoporous  $\text{TiO}_2$  film is dispersive. The strong dispersive transport character has been reported in the literature and various experimental methods to investigate the transport properties of mesoporous metal oxide films are reported, e.g., intensity-modulated photovoltage or photocurrent spectroscopy,<sup>31,88-91</sup> photocurrent transient measurements with and without background illumination<sup>57-64,92</sup> and impedance

spectroscopy.<sup>93-95</sup> Such measurements were performed on dye sensitized electrodes as well as on bare TiO<sub>2</sub> electrodes in organic and aqueous electrolytes, with and without redox species. With this method it was possible to derive effective electron diffusion constants, and this was done as a function of saturated (filled) and unsaturated (unfilled) trap states. To do this, analytical expressions for the current decay were fitted to the experimental data or the transient peak time was used to calculate the diffusion constant as mentioned in section 4.3.

The analytical expressions, used in the literature to derive the diffusion constant, are based on the assumption that

- a) recombination can be neglected on the time scale of the measurement and
- b) the TiO<sub>2</sub> film can be approximated by a semi-infinite medium, as shown in Figure 4.7 of the previous chapter.

In contrast to that I measured photocurrent transient under various conditions including high recombination.

Simple numerical analysis of photocurrent transients has been presented in the literature, but these programs did either not include an electron intensity dependent diffusion coefficient<sup>61</sup> or were restricted to a very simple diffusion coefficient<sup>65</sup> (see also section 4.4.1.2). To investigate dispersive transport in more detail than what has been reported in the literature, I used the numerical model that was presented in section 4.5. Simulated and experimental measured photocurrent transients were analyzed in the same way in order to compare them. This means that an effective diffusion constant was derived from the transient peak time, according to eq. (4.2), for measured as well as for simulated transients. In the latter case comparison between the diffusion constant derived from  $t_p$  and the diffusion constant which was used as an input parameter for the calculation indicated if eq. (4.2) was applicable for a correct derivation of  $D_e$ .

In the following, experimental results are qualitatively explained in terms of trapping and detrapping which is the origin for dispersive transport. The impact of the trap state distribution in energy space is discussed in detail in section 5.2.2. In section 5.3 it is

shown that eq. (4.2) is not appropriate to derive diffusion constants from photocurrent transient measurements when the recombination current is high.

### 5.2.1 Dispersive transport: Qualitative analysis

Potential dependent measurements show a shift of  $t_p$  which results in an increase of the effective diffusion constant  $D_e$  (calculated using eq. (4.2); see Fig. 4.9b) by more than one order of magnitude. This increase at negative applied potential can qualitatively be explained by trap filling, which is schematically depicted in Figure 5.5a & b. The Fermi levels of the FTO substrate and the TiO<sub>2</sub> film are in thermal equilibrium if no external bias is applied (shown in Figure 5.5a). At negative applied potential electrons are injected into the TiO<sub>2</sub> film so that  $E_{Fn}$  shifts towards the CB edge. Electronic gap states below  $E_{Fn}$  are filled up and cannot trap photo-generated electrons, which results in a higher effective diffusion constant and, subsequently, in a shorter peak time.

At positive external applied potentials the situation is different because hole transport in the TiO<sub>2</sub> is a rather slow processes. Furthermore hole transfer from the TiO<sub>2</sub> into the electrolyte is a fast process so that it is not possible to equilibrate the quasi-Fermi level of the mesoporous TiO<sub>2</sub> film with that of the FTO substrate, as shown in Figure 5.5c. Thus, the applied positive potential does not affect the level of filled and unfilled trap states inside the porous film, which explains the constancy in  $t_p$  at positive applied external potential for samples without compact underlayer (fig. 4.9a). Samples with a compact TiO<sub>2</sub> layer might have an additional potential-dependent series resistance due to a sufficiently depleted compact layer at positive bias (fig. 4.9b). Furthermore a capacitive element might be introduced into the measurement circuit due to the space charge capacitance of the compact layer. The series resistance and the space charge capacitance can affect the  $RC$ -time constant of the measurement circuit, which will be discussed in more detail in section 5.4.1.

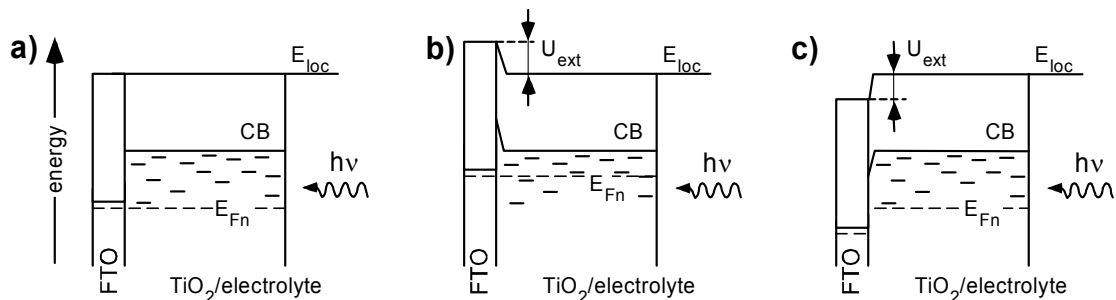


Figure 5.5: (a) Energy band diagram of a mesoporous  $\text{TiO}_2$  film immersed into an electrolyte at zero applied potential. The lines below the  $\text{TiO}_2$  CB represent electronic states inside the band gap. (b) As (a) but at negative applied potential ( $U_{\text{ext}}$ ) so that the gap states below  $E_{F_n}$  are filled. (c) As (a) but at positive applied potential.

Even though the positive applied potential does not change the quasi-Fermi level in the  $\text{TiO}_2$  film, it affects the intensity and shape of the transient current, which can be seen from Figure 4.8a & b. This indicates that the potential distribution at the FTO/ $\text{TiO}_2$  interface changes the boundary conditions for electron transport at this interface. The electrostatic field at this interface has been investigated separately by photocurrent transient measurements, where the samples were illuminated from the glass substrate side (section 4.5), and these results are discussed in more detail in section 5.4.

Intensity dependent transient measurements show a shift of  $t_p$  towards shorter times with increasing light intensity (Figure 4.10). The frequency of subsequent laser flashes was 1 Hz and the mesoporous  $\text{TiO}_2$  film was not able to reach thermal equilibrium within one second. In that way the electron concentration in the  $\text{TiO}_2$  film and, thus,  $E_{F_n}$  could be raised above the thermal equilibrium value without external applied potential or bias light. Traps below  $E_{F_n}$  remained filled which led to an intensity-dependent increase of the effective diffusion constant, shown in Figure 4.10b.

Trap filling and optical pumping of the  $\text{TiO}_2$  film is schematically shown in Figure 5.6a for the first laser excitation, which increases  $E_{F_n}$  at the electrolyte side of the film. Immediately before the second flash the  $\text{TiO}_2$  film is still not in thermal equilibrium, as shown in Figure 5.6b, so that trap states below  $E_{F_n}$  remain filled. At the second flash some traps are still saturated, so that electron transport is enhanced (Figure 5.6c).

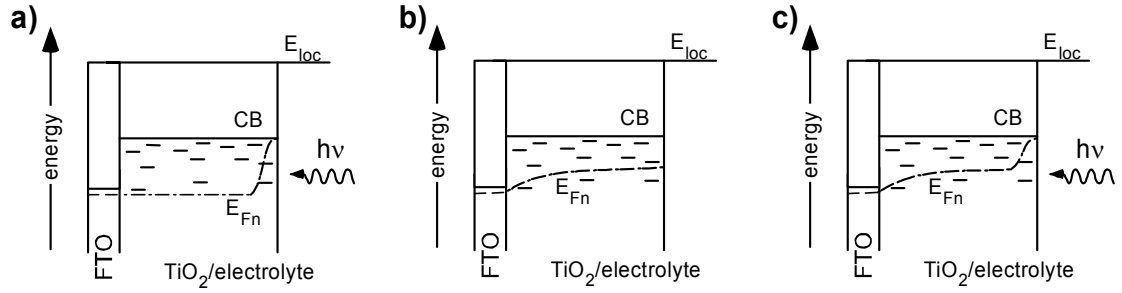


Figure 5.6: (a) First laser excitation. (b) Just before the second excitation the  $\text{TiO}_2$  film did not reach thermal equilibrium. (c) Second laser excitation.

While potential and intensity dependent measurements are qualitatively well explained by trap filling, numerical analysis is required to interpret the experimentally observed shift of  $t_p$  towards longer times with increasing pH value. This effect will be discussed in section 5.3.

## 5.2.2 Dispersive transport: Numerical analysis

The strong experimentally observed asymmetry of the light intensity dependent photocurrent transients (Figure 4.10a) can be simulated if an electron density dependent diffusion coefficient, as defined by eq. (4.7), is used for the calculations. The asymmetry of the transient current is expressed by a shift of  $t_p$  towards shorter times with increasing illumination intensity and by an extended current decay. Ideal photocurrent transients without dispersive transport ( $dp = 0$ ) should show an almost symmetric current with respect to  $t_p$ , when plotted on a logarithmic time scale, as shown in Figure 4.16a. This asymmetry and the shift of  $t_p$  are increasing with increasing dispersion coefficient  $dp$ , which can be seen from Figure 4.16b-d. The transient peak time of the simulated curves was used to calculate an effective diffusion constant according to eq. (4.2), which is shown in Figure 4.17a. I found that the normalized diffusion coefficient, shown in Figure 4.17b, has a characteristic convex (decreasing slope with increasing light intensity), linear (constant slope), or concave shape (increasing slope with increasing light intensity).

Figure 5.7 shows the calculated diffusion coefficients (using eq. (4.7)) as a function of the normalized electron density,  $n(i)/N_{CB}$ , for different dispersion parameters  $dp$ . The

normalized diffusion coefficient shows the convex, linear or concave shape due to the way  $D_e$  was defined in eq. (4.7). However, it is not obvious at all that the characteristic intensity dependent shape of  $D_e$  is conserved when it is derived from a simulated transient. Note that  $D_e$  is defined *locally* (as a function of the *local* electron concentration) and in each time step of the calculation  $D_e$  is different between each neighboring pair of slices.

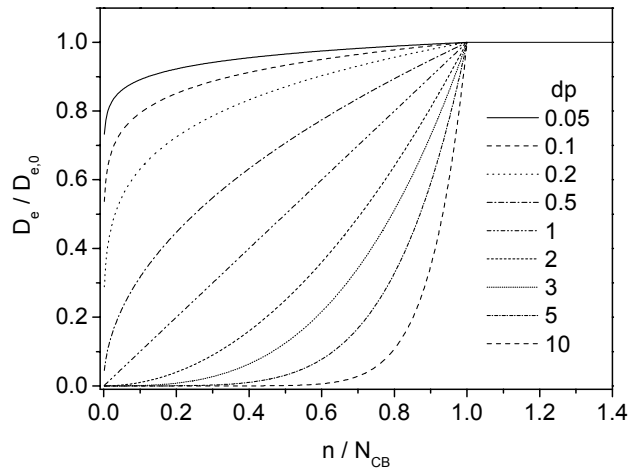


Figure 5.7: Normalized diffusion coefficient ( $D_e/D_{e,0}$ ) as a function of the normalized electron density ( $n/N_{CB}$ ), calculated for different values of the dispersion parameter,  $dp$ , using eq. (4.7)

Comparison between Figure 4.17b and Figure 5.7 shows furthermore that only the convex or concave shape is conserved and not the exact functional dependence from eq. (4.7). Figure 4.17b shows, for example, no significant difference for the normalized  $D_e$  values which were simulated with  $dp = 2$  and  $dp = 3$ , in contrast to the calculated local diffusion coefficient  $D_e(i + 1/2)$  shown in Figure 5.7.

The mathematical approach chosen to introduce dispersive transport by an electron concentration dependent diffusion coefficient is only meaningful if it can be related to a certain trap distribution. More sophisticated effective diffusion coefficients as a function of the trap distribution and the local electron density have been proposed in the literature<sup>96,97</sup> but were not used for the simulations because they require more input parameters. These parameters are not exactly known and rough estimates as input

parameters do not lead to more precise quantitative results compared to the relatively simple approach that I chose. The relation between the diffusion coefficient defined by equation (4.7) and the trap distribution is schematically depicted in Figure 5.8. The magnitude of  $D_e$  depends on the density, cross section and the energy level (more precisely on the energy difference between  $E_{CB}$  and  $E_{Fn}$ <sup>36</sup>), of filled and unfilled trap states. A dispersion parameter  $> 1$  can be used to describe localized traps, as shown in Figure 5.8a-c. The energy difference between  $E_{CB}$  and  $E_{Fn}$  does not change significantly if most of the traps are filled, due to the high trap state density around  $E_t$ . Only if the electron density is getting close to the value of the total trap state density,  $E_{Fn}$  moves significantly towards  $E_{CB}$  (Figure 5.8c). The total number of trap states is given by the normalization constant. For all simulations presented in this work, the density of electronic states at the bottom of the CB,  $N_{CB}$ , was taken as normalization constant. A more homogeneous trap distribution in energy space can be described by a dispersion parameter  $\sim 1$ , as shown in Figure 5.8d-f. At moderate trap occupation the quasi-Fermi level shifts more towards  $E_{CB}$  as the number of trapped electrons increases (Figure 5.8e).

A dispersion parameter significantly smaller than 1 describes a trap state distribution with a low density of deep traps and an increasing density of shallow traps towards the bottom of the CB, as shown in Figure 5.8g-i. A small increase of the number of trapped electrons shifts  $E_{Fn}$  strongly towards  $E_{CB}$ , while a further increase leaves  $D^e$  almost unchanged. This shows that the chosen description of the effective diffusion coefficient (eq. 4.7) gives the possibility to introduce different types of electronic trap distributions into the numerical model or to draw conclusions about the trap distribution in experimental systems, when intensity dependent measurements are performed.

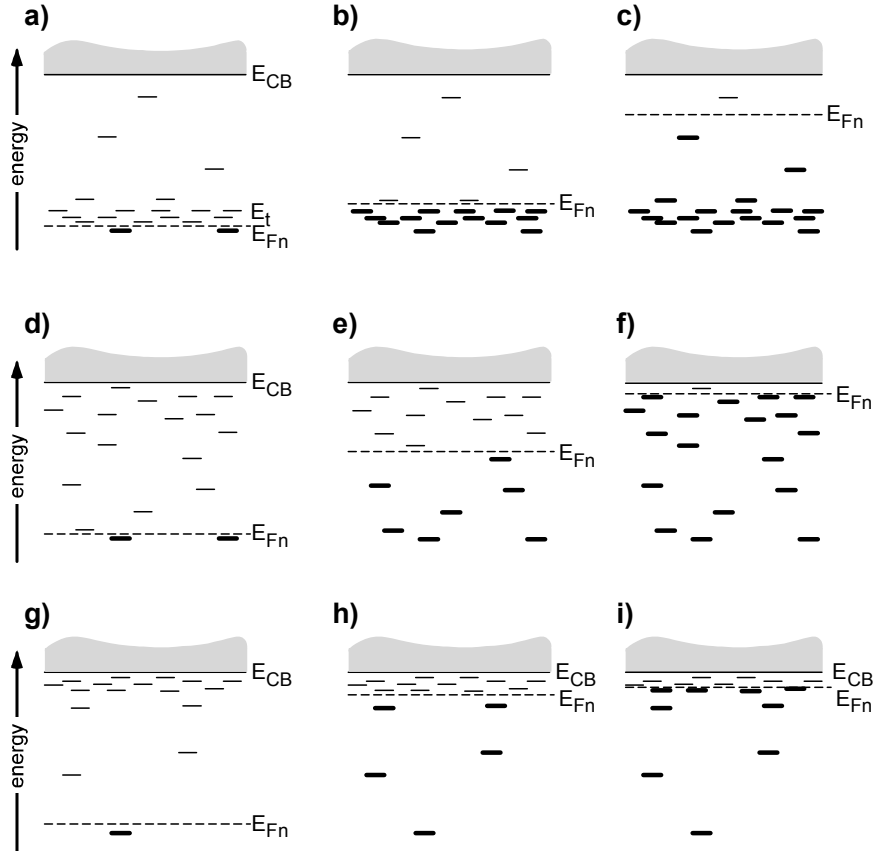


Figure 5.8: (a) Localized trap states ( $dp > 1$ ) around  $E_t$  at low density of trapped electrons; (b) as (a) at higher trapped electron density; (c) as (b) at high occupation level of trap states. (d) Homogeneously spread trap distribution ( $dp \approx 1$ ) at low electron density; (e) as (d) at medium trapped electron density, which causes a shift of  $E_{Fn}$ ; (f) as (e) at high trapped electron density. (g) Trap state distribution with a high density of trap states close the CB ( $dp < 1$ ); (h) as (g) but with a slightly increased density of trapped electrons which shifts  $E_{Fn}$  strongly; (i) as (h) at high trapped electron density.

To check if the chosen definition of the diffusion coefficient (eq. (4.7)) is applicable to the experimental system, it should be possible to simulate experimental results measured by myself, but also results which are reported in the literature.<sup>59</sup> Experimentally diffusion coefficients have been derived from measurements of  $t_p$  on mesoporous films with different film thickness  $L$ .<sup>59</sup> Simulated results of  $t_p$ , presented in section 4.4.4, show the required linear behavior between  $t_p$  and the squared film thickness,  $L^2$ , which shows that the definition of  $D_e$ , according to eq (4.7), is a suitable approach to describe experimental results for mesoporous  $\text{TiO}_2$  films. It is furthermore remarkable that the deviation of the simulated data points from the linear fit is in good qualitative agreement with published data from ref. 59, shown in Figure 5.9.

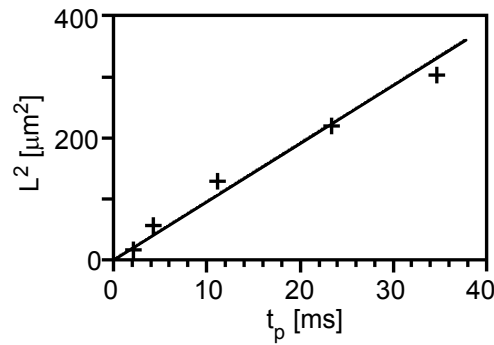


Figure 5.9: Transient peak times  $t_p$  (taken from ref. 59), measured on samples of different thickness, show the same deviation from linearity as simulated results shown in Figure 4.18b.

In summary I have shown that dispersive transport of electrons in mesoporous  $\text{TiO}_2$  films can be well described by a diffusion coefficient as defined by eq. (4.7). From the intensity dependent convex shape of the diffusion coefficient, shown in Figure 4.10b, I conclude that the investigated  $\text{TiO}_2$  films have a trap density that increase towards  $E_{CB}$ . This conclusion can be made because recombination was low at measurement conditions of pH 1.

### 5.3 Numerical simulations including recombination

The simulations in Figure 4.19 show the impact of electron recombination (defined by eq. (4.8)) on the transient current and the transient peak time. These transients were calculated for a recombination current that depends linearly on the excess electron density ( $n(i) - n_0$ ), in the absence of dispersive transport ( $dp = 0$ ). From Figure 4.19b one can see that an increasing recombination constant ( $K_n$ ) shifts the transient peak towards shorter times which results in a bigger diffusion constant, when eq. (4.2) is used (shown in Figure 4.19b). As a result the diffusion constant is overestimated, when it is calculated from the transient peak time according to eq. (4.2), as already mentioned in section 4.4.4. It shows that photocurrent transients, measured on experimental systems with strong recombination, require a more sophisticated analysis.

Another output parameter, which is strongly influenced by the recombination rate  $K_n$  and the recombination parameter  $kp$  is the current  $I_p$  at the transient peak. Intensity

dependent transients (Figure 4.10) show a transient peak current  $I_p$  which seems to converge towards some limiting value with increasing laser energy. Figure 4.20b shows the  $I_p$  values from the measurements of Figure 4.10 together with simulated  $I_p$  values for different recombination rate constants  $K_n$  and recombination parameters  $kp$ . Figure 4.20b shows that the experimentally observed dependence of  $I_p$  on the laser intensity can be well simulated if a non-linear recombination mechanism is used, meaning that the recombination current depends on the excess electron density to the power  $kp$ ,  $(n_i - n_0)^{kp}$ , where  $kp > 1$ .

From Figure 4.12a a strong decrease of the transient current with increasing pH value can be seen, which shows that the recombination increases strongly when the pH becomes less acetic. This can be explained by adsorbed OH groups to the TiO<sub>2</sub> surface which are involved in electron transfer into the electrolyte,<sup>66,67</sup> as already discussed above (5.1.2). The measurements show an increase of  $t_p$  with increasing recombination (Figure 4.12a) in contrast to a  $t_p$  decrease, which would be expected for a system without dispersive transport (Figure 4.19b).

When dispersive transport is included in the simulations the effect of the recombination constant  $K_n$  and the recombination parameter  $kp$  become strongly coupled with the diffusion constant  $D_{e,0}$  and the dispersion coefficient  $dp$ . Simulations in Figure 4.21a & b show this effect strongly using two substantial different parameter sets which lead to very similar transients. However it turned out that in the presence of dispersive transport a recombination parameter  $kp > 2$  is required to describe the experimentally observed laser intensity dependence of  $I_p$ . *This shows that the recombination mechanism in mesoporous TiO<sub>2</sub> electrodes, immersed into electrolyte, is strongly non-linear dependent on the excess electron density  $(n_i - n_0)$  and is thus fundamentally different from electron-hole recombination in semiconductors, which is described by Shockley-Read-Hall, Auger or radiative recombination.*<sup>3</sup>

In the previous section it was discussed that intensity dependent photocurrent transient measurements can be used to investigate the electron trap distribution in experimental systems, when the recombination current in the experimental system is negligible. This

was shown in terms of a concave or convex shape of the electron density dependent diffusion coefficient, which is conserved, when  $D_e$  is derived from the transient peak time. *Figure 4.22 shows that this is not longer true when recombination is introduced into the calculations.*  $D_e$  as a function of the laser intensity has a convex shape for  $dp$  values  $> 1$  and  $< 1$ . These simulations show the limitations of photocurrent transient measurements for a quantitative investigation of electronic trap states in energy space in the presence of strong recombination. Comparison of the shape of the transient decay between Figure 4.10a and Figure 4.21 furthermore reveals that the two sets of simulation parameters lead only to a rough agreement between the simulations and the measurements. This might be due to a more complex recombination and/or diffusion process, which cannot be satisfactory described by eqs. (4.7) & (4.8). On the other hand it is also possible that I did not find the best set of input parameters for the simulations, due to the infinite number of possible parameter combinations.

All simulations presented here were based on recombination mechanisms that depend only on the excess electron density inside the porous  $\text{TiO}_2$  ( $n_i - n_0$ ) and not on the density of positive charges inside the electrolyte, even though the program was designed to keep track of the positive charges as well. The huge pH dependence of the photocurrent transients indicates that the concentration of surface adsorbed OH groups has a much stronger impact on the recombination than positive charges, which are transferred into the electrolyte. For the simulations it was assumed that the OH concentrations during the transient measurement remains constant so that the recombination current was only a function of ( $n_i - n_0$ ). If the laser intensity is orders of magnitudes stronger than the one used in this work, the effect of charging the electrolyte might become important and a more sophisticated recombination has to be used.

## 5.4 Investigation of the FTO/TiO<sub>2</sub> interface

Photocurrent transients measured on systems with and without a compact TiO<sub>2</sub> underlayer between the mesoporous TiO<sub>2</sub> films and the FTO substrate showed a different behavior of  $t_p$  at positive applied bias (shown in Figure 4.8 and 4.9 and discussed above) even though electrons are generated far away from the FTO/TiO<sub>2</sub> interface. It is furthermore expected that most of the mesoporous film remains unaffected at applied potential more positive than the OCP, as discussed in section 5.2.1. Thus it is rather surprising that an effect of the underlayer on the current response was observed. To investigate the FTO/TiO<sub>2</sub> interface in more detail, photocurrent transients were recorded, where the illumination direction was changed such that the laser light entered the system from the side of the glass substrate. A thorough investigation of the FTO/TiO<sub>2</sub> interface is furthermore *essential* for the understanding of DSSCs, as pointed out in chapter 2.

The transient current as a function of an external applied potential for an FTO/compact TiO<sub>2</sub> interface is shown in Figure 4.26a. Immediately after excitation the current signal is dominated by charge displacement while charge collection at the contacts is a slower process.<sup>98</sup> Therefore the photo-response at 200 ns can be attributed to a dominant drift current component,<sup>99</sup>

$$\vec{J}^d = q(n\eta_e + p\eta_h)\vec{E} \quad (5.1)$$

with the elementary charge  $q$ , the electron and hole densities  $n$  and  $p$  and the respective mobilities  $\eta_e$  and  $\eta_h$ . The linear dependence of the transient current (see insert of Figure 4.26a) indicates that the  $\vec{E}$ -field depends linearly on the potential difference between the FTO substrate and the electrolyte. Figure 5.10a & b show the  $\vec{E}$ -field for positive and negative applied potential. Energy band diagrams can be derived as shown in Figure 5.10c & d where band bending, as proposed in ref. 100 is neglected. It has to be mentioned that some band bending across the compact layer might be superimposed on the depicted band structure, but this will not change the following analysis. The drift direction of electrons and holes is depicted by arrows underneath the charges in Figure 5.10c & d.

The shown discontinuity in the CB at the FTO/TiO<sub>2</sub> interface<sup>8</sup> is beneficial for electron transfer from the TiO<sub>2</sub> into the FTO substrate. In contrast the VB discontinuity creates an energy barrier for hole transfer in the same direction. At the TiO<sub>2</sub>/electrolyte interface hole injection into the electrolyte is the kinetically dominant process.<sup>59</sup> The dominant currents are depicted as arrows at the respective interfaces. The drift component dominates the transient response at short times while the kinetics at the FTO/TiO<sub>2</sub> and TiO<sub>2</sub>/electrolyte interface dominate the current response at longer transient times, which results in a change of the current sign with time.

Photocurrent transients measured on compact TiO<sub>2</sub> layers as a function of the electrolyte pH show also a linear behavior of the transient current at 200 ns. In oxide semiconductors, the energy levels of the band edges depend on the surface pH due to specific adsorption of OH<sup>-</sup> and H<sup>+</sup> ions. The energy bands shift towards the vacuum level with increasing pH by 59 mV/pH, if specific adsorption of other ions from the solution is negligible.<sup>67</sup> The compact nature of the TiO<sub>2</sub> layer prevents interaction of the electrolyte with the FTO/TiO<sub>2</sub> interface so that the intrinsic TiO<sub>2</sub> and FTO properties define the band alignment. In contrast, the energy levels of the TiO<sub>2</sub> bands at the liquid interface are defined by the pH value of the electrolyte. If the slope of the linear fit from the insert of Figure 4.27a of 0.10 mA/pH is converted into a resistivity (using a band shift of 59 mV/pH) one gets a value of 0.58 kΩ, which is in excellent agreement with the value of 0.57 kΩ from the potential-dependent measurements (cf. section 4.5.1). *This shows that an electrostatic field can be introduced into a compact TiO<sub>2</sub> layer with a polarity, defined by the pH of the electrolyte.* Band diagrams for pH-dependent measurements are similar to the diagrams depicted in Figure 5.10c & d.

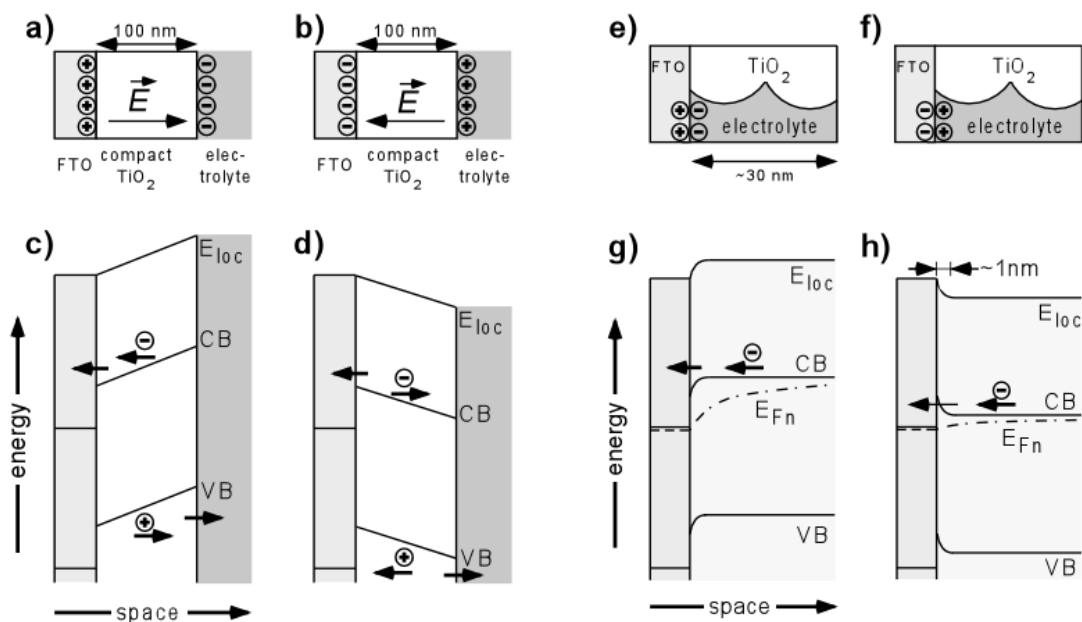


Figure 5.10: (a) Schematic drawing of the electrostatic field in the compact  $\text{TiO}_2$  layer for a positive potential, applied with respect to a reference electrode. (b) As (a) for negative applied potential. (c) Energy band diagram for positive applied potential. Photo-generated electrons (in the CB) and holes (in the VB) migrate in the electric field. The arrows at the interface show the kinetically favorable current (hole injection into the electrolyte, electron collection at the FTO substrate). (d) As (c) but for negative applied potential. Note that the drift current (which dominates at short transient times) has a direction opposite to that of the interface current (which dominates the signal at long transient times). (e) Schematic drawing of two  $\text{TiO}_2$  particles next to the FTO/mesoporous  $\text{TiO}_2$  interface for positive applied potential. The potential drops across a Helmholtz layer at the FTO/electrolyte interface. (f) As (e) for negative applied potential. (g) Energy band diagram for the FTO/mesoporous  $\text{TiO}_2$  interface at positive applied potential. The screening of the electrolyte keeps the  $\text{TiO}_2$  bands flat. Band bending occurs only very close to the interface on a scale of 1-2 nm. (h) As (g) for negative applied potential so that a barrier for electron transport is created at the interface.

Photocurrent transients of the porous  $\text{TiO}_2$  / FTO electrolyte system do not show any change in the sign of the current response. This can be interpreted by the absence of a drift current component and leads to the conclusion that most of the excess charge carriers are generated in a region which is field free. In the mesoporous  $\text{TiO}_2$  system, the applied electrostatic potential difference between the FTO substrate and the electrolyte drops across a Helmholtz layer at the FTO/electrolyte interface, which is schematically shown in Figure 5.10e & f and in Figure 4.31a. The electrostatic potential distribution inside the  $\text{TiO}_2$  particles is determined by the potential of the FTO and the electrolyte and drops very close to the interface, as shown from calculations, in section 4.6.3. Energy band diagrams for the first two layers of  $\text{TiO}_2$  particles in contact

with the FTO are depicted in Figure 5.10g & h. They show a sharp electrostatic potential drop at the FTO/TiO<sub>2</sub> interface for positive (Figure 5.10g) and negative applied potential (Figure 5.10h). The positive transient current at negative applied potentials indicates that the electrostatic barrier does not completely block electron transfer into the FTO. Hole Transport of holes in the mesoporous system, is not considered because holes are injected much faster into the electrolyte than are electrons.<sup>59</sup>

The potential dependence of the current transients can be explained by a difference in the gradient of the electron quasi-Fermi level  $E_{Fn}$ , also shown in Figure 5.10g & h. The gradient of  $E_{Fn}$  at positive applied potential is stronger than at negative applied potential, which results in a weaker current response and is consistent with the experimental results (Figure 4.26b).

Transient measurements on porous TiO<sub>2</sub> samples as a function of the pH value (Figure 4.27b) have to be interpreted differently. H<sup>+</sup> and OH<sup>-</sup> ions affect the levels of the energy bands of the TiO<sub>2</sub> and the FTO in a similar fashion. Therefore, the electrostatic field at the FTO/TiO<sub>2</sub> interface is not expected to change significantly as function of the pH. The observed pH dependence can be attributed to a difference in the recombination current into the electrolyte, which changes the effective diffusion constant.

The investigation of the FTO/TiO<sub>2</sub> interface shows a fundamental difference in the electrostatic potential distribution. *In compact TiO<sub>2</sub>/FTO interfaces an electrostatic field is present throughout the compact layer. Upon negative applied bias no change in the transient sign is observed for mesoporous TiO<sub>2</sub>/FTO interfaces which indicates that electron tunnel through a barrier at this interface.* Based on this observation the tunnel-junction model was derived for DSSCs with a mesoporous TiO<sub>2</sub>/FTO interface. Extension of the tunnel-model to FTO/compact/ mesoporous TiO<sub>2</sub> based DSSCs is discussed in section 5.5.

The previously observed increase in the transient current with increased potential, shown in Figure 4.8, can be explained by the improved boundary conditions without barrier for electron collection at the FTO/TiO<sub>2</sub> interface, when a positive potential is applied to the FTO substrate (see Figure 5.5c and 5.10g). An additional impact due to a difference of a series resistance caused by the compact layer and a different capacitance, due to a space charge capacitance in the compact layer, are discussed in the following section in the context of an  $RC$  time constant of the experimental system. Before that the origin of the  $RC$  element is clarified.

#### **5.4.1 The impact of the $RC$ contact on photocurrent transients**

The impact of the system resistance  $R_{TiO_2}$ , the measurement resistor  $R_m$  and the capacitance of the experimental system  $C$  is a subject that has been addressed in the literature<sup>59</sup> but it was never clarified what really defines the capacitor and the resistor. Solbrand *et al*<sup>59</sup> proposed that the  $RC$  constant has an impact on the transient response at short transient times. They observed an immediate transient current at immediate after laser excitation, followed by a decay before the transient peak due to diffusion of electrons through the mesoporous film appeared. Their measured transients looked similar to the simulated transient, shown in Figure 5.11. It was argued that electron-electron repulsion at short transient times inside the nanoparticles gives rise to the observed initial transient current. However, this requires that the electrolyte is not capable to screen the electric signal, which seems to be unlikely. In contrast I observed similar photocurrents if measurements were performed under high laser intensity on low quality films with small cracks. Solbrand *et al.* used a laser intensity of 200 mJ, which is approximately 60 times more than the strongest and 1000 times more than the weakest laser intensities used in this work.

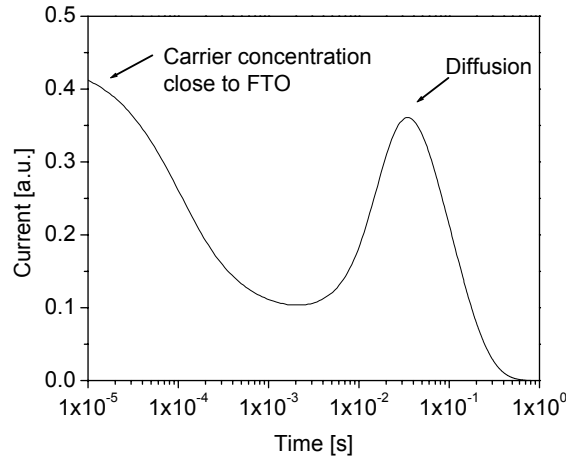


Figure 5.11: Simulated photocurrent transient for a 10  $\mu\text{m}$  thick  $\text{TiO}_2$  film. The initial transient current is due to photo-generated electrons close to the FTO contact while the second peak is related to electron diffusion through the  $\text{TiO}_2$  film.

I will discuss the possibility of an immediate photocurrent response, caused by weak electron generation close to the FTO interface due to a high laser intensity and residual crack. The photocurrent transient in Figure 5.11 was simulated for a laser pulse energy of 200 mJ, a wavelength of  $\lambda = 308 \text{ nm}$  and an absorption coefficient  $\alpha = 1300 \text{ cm}^{-1}$ . The absorption coefficient is relatively low to include electron generation throughout the cracks deep into the film. Electrostatic repulsion was not included into the simulation and one can see that the initial peak can be explained by a small excess electron density, which is generated close to the FTO/ $\text{TiO}_2$  interface by the incident laser light, due to its high intensity. This excess electron density gives rise to an immediate current, which decays before additional electrons reach the contact by diffusion through the film. This alternative interpretation of an additional transient current peak before the main diffusion peak seems to be more reasonable than the postulated displacement current,<sup>59</sup> which is supposed to be measured through the electrolyte with its screening abilities.

The derivation of the  $RC$ -contact (section 4.4.1.7) shows that the  $RC$  time constant of the system is defined by the resistance of the contact, the measurement resistor  $R_m$ ,

which was the internal resistor of the scope ( $1 \text{ M}\Omega^e$ ), and the capacitance of the FTO contact. The contact capacitance can be due to a Helmholtz layer, if the FTO substrate is in direct contact with the electrolyte and to a space charge layer of the FTO substrate. Figure 4.24 shows simulated photocurrent transients as a function of the  $RC$  time constant. One can see that the shape and the peak position of the transient remains nearly unchanged if  $RC < 30 \text{ ms}$ . Further increase of the time constant flattens the transient and increases the transient time, which is shown in Figure 4.24b. Furthermore, one can see that the effective diffusion coefficient (derived from  $t_p$  according to eq. (4.2)) increases by a factor of five with increasing time constant. The simulations shown in Figure 4.24 were done in the absence of dispersive transport ( $dp = 0$ ) and electron recombination ( $K_n = 0$ ) to emphasize the effect of the contact. One can also see that no new features appear at short transient times such as those proposed by Solbrand *et al.*

*The physical origin of the shift towards longer transient times (see in Figure 4.24) is the charging of the capacitor, i.e., the Helmholtz capacitor or the space charge capacitance of the FTO.* The impact of the  $RC$  time constant on the transient current decreases if recombination is introduced into the numerical system, which can be seen from Figure 4.26. The recombination causes a faster discharge of the capacitor, which reduced the integrating character of the contact, the cause for the delay of the transient peak. The simulations in Figure 4.25 include only recombination from the  $\text{TiO}_2$  into the electrolyte, while recombination current from the FTO substrate into the electrolyte was neglected. The impact of the  $RC$ -constant is further decreased if that recombination path is included in the simulations (not shown).

The effect of an additional series resistance can furthermore explain the difference in the potential-dependent transient peak time measured on systems with and without a compact  $\text{TiO}_2$  layer between the FTO substrate and the mesoporous film, shown in Figure 4.8 and 4.9a. At positive applied potential (larger than the OCP)  $t_p$  is larger for a system that includes a compact layer. This layer is depleted at these potentials and, therefore, has a high resistance, which has to be added to the total resistance of the

---

<sup>e</sup> The  $50 \text{ }\Omega$  input resistor of the oscilloscope could only be used when the samples were optically excited from the glass side, as explained in section 3.3.1.

system. As a result the  $RC$  constant is larger and the transient peak is shifted towards longer times. Furthermore the compact layer suppresses electron recombination from the FTO into the electrolyte, which brings out the effect of the  $RC$  constant on the transient current, as discussed above. The blocking character of the compact layer might be furthermore potential-dependent, which then can explain the decrease of  $t_p$  at positive applied potentials  $>0.3$  V vs. Ag/AgCl (see Figure 4.9a).

It has been shown here (Figure 4.24 and 4.25) that the derivation of an effective diffusion coefficient from photocurrent transient measurements according to eq. (4.2) requires a small  $RC$ -constant of the measurement system. This was up to now neglected in the discussion and interpretation of photocurrent transient measurements and has to be addressed because many of the reported measurements were performed with a high measurement resistor of  $1\text{ M}\Omega$ . The  $RC$  constant is defined by the FTO/TiO<sub>2</sub> contact and the measurement resistor  $R_m$  and the laser induced charges are generated outside the capacitive element, which is in contrast to time of flight measurements.

*Photocurrent transient measurements show a potential-dependent diffusion coefficient, which has been interpreted in terms of trap filling. Furthermore, they show a laser intensity-dependent shift of the transient peak time  $t_p$ , which can be simulated if dispersive transport is introduced into the system. A decrease of the diffusion coefficient by a factor of three with increasing pH has been interpreted in terms of increased recombination. Simulations with an increasing recombination rate constant show a decrease of the effective diffusion coefficient by roughly the same factor, when dispersive transport is included. Without dispersive transport the effective diffusion coefficient increases with increasing recombination constant. As an artifact the effective diffusion constant decreases due to an increasing  $RC$  constant. It was derived in eq. (4.12) that the  $RC$  constant is defined by the contact capacitance and a series resistance of the system and not by the mesoporous TiO<sub>2</sub> film.*

*Photocurrent transients were furthermore used to investigate the electrostatic potential distribution at the FTO/TiO<sub>2</sub> interface, when the illumination direction was changed from the electrolyte to the substrate side, as presented in chapter 4.5. Based on these measurements the tunnel junction model was developed to explain DSSC operation.*

## 5.5 The tunnel model

At the mesoporous TiO<sub>2</sub>/FTO interface electron tunneling does explain the observed photocurrent transients. Based on these findings the tunnel model, presented in chapter 4.6, was derived.

The tunnel model basically shows that the DSSCs can work without an electrostatic built-in field. It was discussed in chapter 2.1.5 that a conduction band discontinuity is sufficient to generate a photovoltage. However it is not obvious how the photocurrent depends on the photovoltage in case of a cell without built-in field. The tunnel model presented in section 4.6 shows that for sufficiently thin barriers  $I$ - $V$  curves with a high fill factor can be achieved. The solid  $I$ - $V$  curve in Figure 4.33 does not differ significantly from that of an ideal solar cell without a barrier. This might lead to the wrong conclusion that there is no difference between the tunnel-junction model and the kinetic model as presented in ref. 33. It has to be emphasized that the model from ref. 33 assumes that the chemical potential is converted without any losses into an electrostatic potential at the FTO/TiO<sub>2</sub> interface *at any voltage*. This is not the case in the presence of a barrier for electron transfer from the TiO<sub>2</sub> into the FTO, even though the  $I$ - $V$  curves are similar. *For a fundamental understanding of the working principle of the cells this is essential because it demonstrates that DSSCs can work perfectly well without any built-in field. A CB discontinuity caused by different electron affinities of the FTO and the TiO<sub>2</sub> is sufficient for efficient DSSC operation. In this they differ fundamentally from p-n junction cells, which is the main conclusion from the tunnel-junction model.*

It is mentioned again that the potential distribution shown in Figure 4.31 was calculated for a system *without* underlayer. In contrast to what is the case for the mesoporous TiO<sub>2</sub>/FTO interface, a light-induced electrostatic barrier, which drops across the 50 to 100 nm thick compact layer, is too thick for efficient electron tunneling. However electron tunneling in systems with underlayer might be possible if the electrostatic potential barrier drops over a very narrow region inside the compact underlayer. This could be the case if Li<sup>+</sup> ions (most electrolytes that are used contain Li<sup>+</sup>) intercalate into the compact layer,<sup>101</sup> get sufficiently close to the FTO substrate and are charge-

compensated by electrons in the FTO substrate. A schematic drawing is shown in Figure 5.12a where the positive charges in the compact  $\text{TiO}_2$  layer are intercalated  $\text{Li}^+$  cations. The energy band diagram in Figure 5.12b shows the sharp electrostatic potential drop inside the compact layer.  $\text{Li}^+$  intercalation might also change the electrostatic potential distribution at the mesoporous  $\text{TiO}_2$ /FTO interface and thus increase the effective interface area for electron tunneling. In this way electron tunneling can be improved in the compact  $\text{TiO}_2$ /FTO and in the mesoporous  $\text{TiO}_2$ /FTO junction.

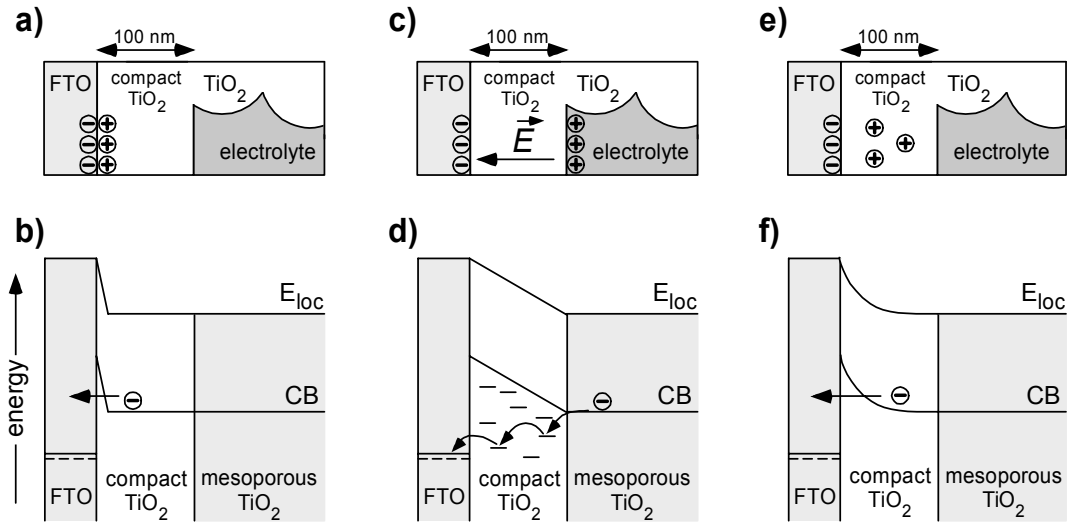


Figure 5.12: (a) Schematic drawing of an FTO/compact/mesoporous  $\text{TiO}_2$  interface at negative applied potential to the FTO substrate, w.r.t. the electrolyte redox potential. The positive charges in the compact  $\text{TiO}_2$  layer are  $\text{Li}^+$  cations intercalated into the oxide lattice, charge compensated by electrons in the FTO substrate. (b) Energy band diagram of the compact  $\text{TiO}_2$ /FTO interface which shows the sharp electrostatic potential drop in the compact layer which may be thin enough to allow for efficient electron tunneling. (c) Schematic drawing of the compact layer without charge accumulation. (d) Electron hopping through electronic states in the  $\text{TiO}_2$  band gap. (e) Charge accumulation in the compact layer, caused by ionized gap states. (f) Band diagram including band bending due to the space charge in the electronic gap states.

Including electronic states in the  $\text{TiO}_2$  band gap is another possibility to explain DSSC operation for devices with a barrier across the compact  $\text{TiO}_2$  underlayer. The tunnel junction model does not include gap states. Such states might be involved in electron hopping through the barrier, as shown in Figure 5.12c and d. Electron hopping through

gap states in the barrier might be the dominant transport mechanism in DSSCs with a compact TiO<sub>2</sub> layer. Additionally, charge accumulation in the gap states might cause band bending in the compact layer and thus narrow the barrier which would be beneficial for electron tunneling. However this would require a rather high density of gap states. Figure 5.12e shows a schematic picture of positive charged gap states in the compact layer while the energy band diagram in Figure 5.12f shows the band bending caused by the space charge region in the compact layer. Thermionic emission over all these barriers is a possible transport mechanism, but the total current across a barrier height of 0.5 eV and more is too low for a reasonable performing DSSC.

The photocurrent transient measurements in sections 4.5.1 and 4.5.2 indicate that an electric field is present across the entire compact layer, which rules out the proposed band structure in Figure 5.12b, so that hopping seems to be the most likely transport mechanism across the compact layer in the presence of an energy barrier.

## 6 Conclusions

Molecular surface modification was shown to be able to change the energy level alignment of a nanocrystalline, mesoporous TiO<sub>2</sub> films with respect to a redox potential of an electrolyte. The TiO<sub>2</sub> films were modified with benzoic and dicarboxylic acid derivatives with different molecular dipole moments, due to different functional groups. Co-adsorption of these molecules with the N3 dye was used to tune the  $V_{oc}$  and  $I_{sc}$  of DSSCs in a systematic fashion. The observed linear change of the  $V_{oc}$  with the molecular dipole moment was explained by a dipole-induced shift of the TiO<sub>2</sub> CB with respect to the redox potential. This is consistent with predictions of the kinetic and the thermionic emission models, known from the literature,<sup>8,26</sup> as well as with the tunnel contact model which was developed here. In all three models the maximum achievable photovoltage in DSSCs is limited by the potential difference between the TiO<sub>2</sub> CB and the redox potential of the electrolyte. A dipole-dependent change of  $E_{CB}$  results in a change of the  $V_{oc}$  according to the models, which is in agreement with experimental observation.

While the interpretation of the molecule-induced  $V_{oc}$  shift can be understood easily by the band level alignment, it is not obvious why the photocurrent shows a similar trend. Conductivity measurements were carried out to investigate electron transport through mesoporous TiO<sub>2</sub> films in more detail. From bipotentiostat measurements it was concluded that the most pronounced change in conductivity is caused by a shift of the TiO<sub>2</sub> CB. A change in the energy distribution of electron traps was not detectable with this measurement method due to a high Faradaic current in the baseline measurement. The dipole moment dependence of the photocurrent was explained by a different overlap of electronic states in the TiO<sub>2</sub> with electronic states of the oxidized species of the electrolyte and by an enhanced  $E_{Fn}$  gradient below  $V_{oc}$ , due to the CB shift.

Time resolved photocurrent measurements were used to investigate the impact of traps. It was found that the transients shift towards shorter times if the light intensity is increased or if a negative potential is applied to the film. This is consistent with the filling of electron traps which are the origin of dispersive electron transport in

mesoporous TiO<sub>2</sub> films. Transient measurements as function of the electrolyte pH show a strong increase of the recombination rate with increasing pH value

Photocurrent transients can be modeled with a simple analytical expression, but it is not possible to include recombination or dispersive transport into such expressions. To overcome these restrictions a numerical program was developed and simulations showed that the experimentally observed shift of the transient peak can be attributed to dispersive transport. Comparison of simulated results (without recombination) with measured data indicates that the number of trap states increases, the nearer they are in energy to  $E_{CB}$ . The intensity-dependent transient current can be simulated by a recombination mechanism which is non-linear in the electron recombination (which was introduced into the model by a recombination exponent  $kp > 1$ ). To simulate experimental results a recombination exponent  $> 2$  was needed, independent of the transport parameters  $D_e$  and  $dp$ . This indicates that the overlap of electronic states of the TiO<sub>2</sub> and the electrolyte strongly increases with increasing electron density inside the TiO<sub>2</sub>. This result gives further support for a trap state density that increases, the closer the traps are in energy to  $E_{CB}$ . Strong recombination can, furthermore, shift the transient peak towards shorter times, so that an effective diffusion constant is derived, which is larger than the real diffusion constant. The inverse effect is observed when the  $RC$  time constant of the system is introduced into the simulation. An increasing time constant shifts the transient peak towards longer transient times so that diffusion coefficients, smaller than the real diffusion coefficient, are derived from the measured spectra. Both aspects, the effect of recombination and of the  $RC$  constant, are usually neglected in the literature even though they influence the photocurrent transient and the diffusion coefficient, derived from the transient measurements.

In summary the model was used to investigate photocurrent transients in detail and to investigate possible sources for artifacts. Admittedly, it was not possible to find one unique set of input parameters to simulate measured results. Thus increasing dispersive transport behavior can be compensated by increasing recombination so that several combinations of input parameters can be found to simulate the similar results. However it was shown that simulations of experimental results require a recombination

parameter  $>2$  and a dispersion parameter  $> 0.5$  which show that recombination is strongly non-linear and transport is dispersive.

Photocurrent transient measurements were used to investigate the  $\text{TiO}_2/\text{FTO}$  contact. Reviewing proposed models in the literature reveals that the major disagreement is the electrostatic potential distribution at the  $\text{FTO}/\text{TiO}_2$  interface. Furthermore, DSSC configurations with and without compact  $\text{TiO}_2$  layer between the FTO substrate and the mesoporous  $\text{TiO}_2$  film are reported in the literature. Potential-dependent photocurrent transient measurements of  $\text{FTO}/\text{mesoporous TiO}_2$  and  $\text{FTO}/\text{compact TiO}_2$  interfaces indicate that the electrostatic potential drops on a very short distance at the mesoporous  $\text{TiO}_2/\text{FTO}$  interface. This potential drop seems to occur across the entire compact layer at the compact  $\text{TiO}_2/\text{FTO}$  interface.

Kelvin probe measurements were used to determine the FTO work function as well as the  $\text{I}^- / \text{I}_3^-$  redox potential. Both energy levels were measured with respect to the same reference, a significant advantage of this measurement method compared to work function and redox potential measurements with respect to two different reference systems. Thus, the huge conversion uncertainty of approximately 0.4 eV between the solid state energy scale and the electrochemical scale could be neglected. The data suggest that an energy barrier is already present at the  $\text{FTO}/\text{TiO}_2$  interface in thermal equilibrium. This barrier further increases with applied photovoltage. The calculated potential distribution for the mesoporous  $\text{TiO}_2/\text{FTO}$  interface shows that the potential barrier is narrow enough for efficient electron tunneling through it. Thus the tunnel junction model was developed which is based on an analytical expression for electron tunneling through an asymmetric barrier. This expression was modified for the specific case of an  $\text{FTO}/\text{TiO}_2$  interface, where electronic gap states were not considered for the tunnel process. The modified analytical tunnel expression was implemented into a program to simulate  $I$ - $V$  characteristics of DSSCs. The calculated curves show a strong decrease in the fill factor with increasing barrier width. The advantage of the tunnel contact model is the ability to simulate both dark and light  $I$ - $V$  curves that fit with experimental data. This is in contrast to the thermionic emission model, which cannot simulate the dark  $I$ - $V$ s with a reasonable set of physical parameters. *The tunnel-junction model demonstrates for the first time that DSSCs can work entirely without a built-in*

*electrostatic field to promote electron collection at the FTO substrate.* The operation of DSSCs with a compact TiO<sub>2</sub> layer can be explained when electronic gap states are included which are involved in electron hopping through the barrier across the compact layer.

## Appendix A: Simulation input parameters

Figure:	4.16a	4.16b	4.18a	4.18b	4.19a	4.20a	4.21a	4.21b	4.23a	4.24a	4.25a
File name:	ndepD-02-p-03.txt	ndepD-3-p-08.txt	tknT2-02-p-04.txt	tknT2-1-p-08.txt	kn-0-i70-25m7-p-10.txt	i-Dn1-6-dp0-kn1-37-kp3-p-05.txt	i-Dn1-1-dp2-kn1-53-kp4-p-08.txt	i-Dn1-4-dp07-kn1-35-kp3-p-06.txt	kn-1-p-13.txt	RC-dz1-4-kc0-R-Dn1-6-dp0-kn0-p-07.txt	RC-dz1-4-kc0-R-Dn1-6-dp0-kn10-kp1-p-01.txt
contact type	Num.	Num.	Num.	Num.	Num.	Num.	Num.	Num.	Num.	RC	RC
$D_{e,0}$	1.0E-2	1.0E-2	1.0E-2	1.0E-2	2.5E-6	1.0E-6	1.0E-1	1.0E-4	1.0E-4	1.0E-6	1.0E-6
$dp$	0.2	3.0	0.2	1.0	0.0	0.0	2.0	0.7	1.0	0.0	0.0
$K_n$	0	0	0	0	variable	0.1	10	10	variable	0	10
$K_p$	0	0	0	0	1.0	3.0	4.0	3.0	1.0	0.0	1.0
$\alpha$ [ $\text{cm}^{-1}$ ]	1.0E+5	1.0E+5	1.0E+5	1.0E+5	1.0E+5	1.0E+5	1.0E+5	1.0E+5	1.0E+5	1.0E+5	1.0E+5
$T$	300	300	300	300	300	300	300	300	300	300	300
$R_i$	N/A	N/A	N/A	N/A	N/A	N/A	N/A	N/A	N/A	variable	variable
surface area A [ $\text{cm}^2$ ]	0.6	0.6	0.6	0.6	0.6	0.6	0.6	0.6	0.6	0.6	0.6
$d_{HL}$ (nm)	N/A	N/A	N/A	N/A	N/A	N/A	N/A	N/A	N/A	0.20	0.20
$\varepsilon_{HL}$	N/A	N/A	N/A	N/A	N/A	N/A	N/A	N/A	N/A	3.77	3.77
$L_{TiO2}$ [ $\mu\text{m}$ ]	5.0	5.0	5.0	5.0	5.0	5.0	5.0	5.0	5.0	5.0	5.0
$\tilde{\alpha}_{TiO2}$ [nm]	167	167	variable	variable	167	167	167	167	167	167	167
$\tilde{\alpha}_{el}$ [nm]	2000	2000	2000	2000	2000	2000	2000	2000	2000	2000	2000
$Z_{TiO2}$	30	30	30	30	30	30	30	30	30	30	30
$Z_{el}$	100	100	100	100	100	100	100	100	100	100	100
$I_{Laser}$ [mJ]	variable	variable	2.07	2.07	2.07	variable	variable	variable	2.07	2.07	2.07
$\lambda$ [nm]	355	355	355	355	355	355	355	355	355	355	355
$t_{flash}$ [ps]	120	120	120	120	120	120	120	120	120	120	120

The width of the Helmholtz layer at the FTO/electrolyte interface is not needed (not applicable, N/A) if the calculations are performed with a numerical contact (*Num.*). The number of generated charge carriers per laser flash was calculated from the energy and the wavelength of the laser flash.

## **Appendix B: Contact-free photovoltage measurements**

During extensive work with the Kelvin probe I found that the photovoltage of an arbitrary absorber material can be measured accurately in the absence of an electric back contact (floating mode method). This can be explained by standard electrostatics (Poisson equation) and the feasibility of this measurement method was demonstrated on two different model systems, which were measured in floating mode and in a standard configuration with an electrical back contact. This method was published in the Journal of Applied Physics (see Appendix C: List of Publications) and the abstract is given below.

### **Abstract:**

A contact-free method to measure the photovoltage that can be generated by an absorber, upon illumination, is presented. The measurement is based on Kelvin's well-known capacitor method which measures the contact potential difference that builds up between two sufficiently conducting materials of different work function that are electrically connected. We show that the photovoltage of an absorber, which is introduced into the Kelvin capacitor, can be measured accurately, even though it is not in electrical contact to any of the capacitor plates. Comparative measurements of the surface photovoltage of an n-type Si semiconductor surface in grounded and non-grounded mode as well as the interface photovoltage of mesoporous TiO<sub>2</sub>, deposited onto conducting substrate, are presented to demonstrate the feasibility of the concept. This approach enables to measure the photovoltage of complete solar cells and also its single components (absorber, absorber + buffer layer, absorber + buffer layer + electron and/or hole conductor), a matter that is of particular importance for a better understanding of photovoltaic devices like extreme thin absorber cells, dye sensitized solar cells or organic (so-called plastic) solar cells.

## Appendix C: List of publications

- 1) **S. Rühle**, D. Cahen, "*Contact-free Photovoltage Measurements of Photo-Absorbers Using a Kelvin Probe*", J. Appl. Phys., 96 (3), 1556
- 2) **S. Rühle**, D. Cahen, "*Electron Tunneling at the TiO<sub>2</sub>/Substrate Interface Can Determine Dye-sensitized Solar Cell Performance*", J. Phys. Chem. B, 108, 17946.
- 3) F. Lenzmann, J. Krüger, S. Burnside, K. Brooks, M. Grätzel, D. Gal, **S. Rühle**, D. Cahen, "*Surface Photovoltage Spectroscopy of Dye-Sensitized Solar Cells with TiO<sub>2</sub>, Nb<sub>2</sub>O<sub>5</sub>, and SrTiO<sub>3</sub> Nanocrystalline Photoanodes: Indication for Electron Injection from Higher Excited Dye States*", J. Phys. Chem. B, 105 (27): 6347, 2001
- 4) J. Bisquert, D. Cahen, G. Hodes, **S. Rühle**, A. Zaban, "*Physical Chemical Principles of Photovoltaic Conversion with Nanoparticulate, Mesoporous Dye-Sensitized Solar Cells*", J. Phys. Chem. B, 108 (24): 8106, 2004
- 5) **S. Rühle**, Th. Dittrich, "*Investigation of the Electric Field in TiO<sub>2</sub>/FTO Junctions Used in Dye-Sensitized Solar Cells by Photocurrent Transients*", J. Phys. Chem. B, submitted
- 6) **S. Rühle**, M. Greenshtein, S.G. Chen, H. Pizem, H. S. Sukenik, D. Cahen, A. Zaban, "*Molecular Adjustment of the Electronic Properties of Nanoporous Electrodes in Dye Sensitized Solar Cells*", Manuscript in preparation
- 7) **S. Rühle**, K. Fredin, C. Grasso, Th. Dittrich, "*The Impact of Recombination, Dispersive Transport and the FTO/TiO<sub>2</sub> Interface on Photocurrent Transient Measurements*", Manuscript in preparation

### **My contribution and collaborations**

I hereby declare that the thesis summarizes my independent work in the subject. Paper number (2) describes the tunnel-junction model for DSSCs and number (4) the investigation of the FTO/TiO<sub>2</sub> interface. Molecular modification and transport measurements are subject of papers number (6) and (7). The contact free floating mode measurements is presented in paper (1). Paper (3) contains some Kelvin probe measurements that I did at an early stage of my PhD. Fundamental theoretical aspects of the working principle of solar cells, especially DSSCs, is presented in paper (4), where I was involved as equal partner in the scientific discussion and preparation of the manuscript.

The numerical model for photocurrent transients was developed together with Kristofer Fredin (Uppsala University, Sweden) and Catelijne Grasso (University of Gent, Belgium) in a young researcher project, which was imbedded in the work of an European Union research training network (RTN). The rough design of the program was developed during project meetings while the programming was entirely done by myself.

## References

- [1] B. O'Regan and M. Grätzel, *Nature* **353**, 737 (1991).
- [2] M. K. Nazeeruddin, P. Péchy, T. Renouard, S. M. Zakeeruddin, R. Humphry-Baker, P. Comte, L. Cevey, E. Costa, V. Shklover, L. Spiccia, G. Deacon, C. A. Bignozzi, and M. Grätzel, *J. Am. Chem. Soc.* **123**, 1613 (2001).
- [3] J. S. Fonash, *Solar Cell Device Physics* (Academic Press, Belton, Texas, 1981).
- [4] M. A. Green, *Physica E* **14**, 11 (2002).
- [5] A. L. Fahrenbruch and R. H. Bube, *Fundamentals of Solar Cells - Photovoltaic Solar Energy Conversion* (Academic Press, New York, London, 1983).
- [6] K. Schwarzburg and F. Willig, *J. Phys. Chem. B* **103**, 5743 (1999).
- [7] F. Pichot and B. A. Gregg, *J. Phys. Chem. B* **104**, 6 (1999).
- [8] D. Cahen, G. Hodes, M. Grätzel, J. F. Guillemoles, and I. Riess, *J. Phys. Chem. B* **104**, 2053 (2000).
- [9] G. Kron, U. Rau, and J. H. Werner, *J. Phys. Chem. B* **107**, 13258 (2003).
- [10] K. Schwarzburg and F. Willig, *J. Phys. Chem. B* **107** (2003).
- [11] J. Bisquert, *J. Phys. Chem. B* **107**, 13541 (2003).
- [12] B. A. Gregg, *J. Phys. Chem. B* **107**, 13540 (2003).
- [13] J. Augustynski, *J. Phys. Chem. B* **107**, 13544 (2003).
- [14] K. Schwarzburg and F. Willig, *J. Phys. Chem. B* **107**, 13546 (2003).
- [15] U. Rau, G. Kron, and J. H. Werner, *J. Phys. Chem. B* **107**, 13547 (2003).
- [16] G. Hodes, I. D. J. Howell, and L. M. Peter, *J. Electroch. Soc.* **139**, 3136 (1992).
- [17] J. S. Fonash and S. Ashok, *Appl. Phys. Letters* **35**, 535 (1979).
- [18] M. Grätzel, *Journal of Photochemistry and Photobiology A* **164**, 3 (2004).
- [19] X. T. Zhang, H. W. Liu, T. Taguchi, Q. B. Meng, O. Sato, and A. Fujishima, *Sol. Energy Mat. Sol. Cells* **81**, 197 (2004).
- [20] G. R. A. Kumara, S. Kaneko, M. Okuya, and K. Tennakone, *Langmuir* **18**, 10493 (2002).
- [21] G. R. A. Kumara, A. Konno, K. Shiratsuchi, J. Tsukahara, and K. Tennakone, *Chem. Mater.* **14**, 954 (2002).
- [22] S. Rühle, J. Bisquert, D. Cahen, G. Hodes, and A. Zaban, *Conference Proceedings, Quantsol 2003*, Bad Gastein.

- [23] G. K. Boschloo, A. Goossens, and J. Schoonman, *J. Electroanal. Chem.* **428**, 25 (1997).
- [24] M. Turrión, B. Macht, H. Tributsch, and P. Salvador, *J. Phys. Chem. B* **105**, 9732 (2001).
- [25] J. Ferber and J. Luther, *J. Phys. Chem. B* **105**, 4895 (2000).
- [26] G. Kron, T. Egerter, J. H. Werner, and U. Rau, *J. Phys. Chem. B* **107**, 3556 (2003).
- [27] J. B. Asbury, E. Hao, Y. Wang, H. N. Ghosh, and T. Lian, *J. Phys. Chem. B* **105**, 4545 (2001).
- [28] A. Hagfeldt and M. Grätzel, *Chem. Rev.* **95**, 49 (1995).
- [29] D. Vanmaekelbergh and P. E. de Jongh, *J. Phys. Chem. B* **103**, 747 (1999).
- [30] B. van der Zanden and A. Goossens, *J. Phys. Chem. B* **104**, 7171 (2000).
- [31] A. Goossens, B. van der Zanden, and J. Schoonman, *Chem. Phys. Lett.* **331**, 1 (2000).
- [32] G. Schlichthörl, S. Y. Huang, J. Sprague, and A. J. Frank, *J. Phys. Chem. B* **101**, 8141 (1997).
- [33] S. Södergren, A. Hagfeldt, J. Olsson, and S. E. Lindquist, *J. Phys. Chem.* **98**, 5552 (1994).
- [34] J. Bisquert, G. Garcia-Belmonte, and F. Fabregat-Santiago, *J. Solid State Electrochem.* **3**, 337 (1999).
- [35] J. Bisquert, D. Cahen, G. Hodes, S. Rühle, and A. Zaban, *J. Phys. Chem. B* **108**, 8106 (2004).
- [36] J. Nelson, *Phys. Rev. B* **59**, 15374 (1999).
- [37] V. I. Arkhipov, P. Heremans, E. V. Emelianova, G. J. Adriaenssens, and H. Bassler, *J. Non-Crystalline Solids* **338**, 603 (2004).
- [38] R. Cohen, S. Bastide, D. Cahen, J. Libman, A. Shanzer, and Y. Rosenwaks, *Adv. Mat.* **9**, 746 (1997).
- [39] R. Cohen, L. Kronik, A. Shanzer, D. Cahen, A. Liu, Y. Rosenwaks, J. K. Lorenz, and A. B. Ellis, *J. Am. Chem. Soc.* **121**, 10545 (1999).
- [40] D. Gal, E. Sone, R. Cohen, G. Hodes, J. Libman, A. Shanzer, H. W. Schock, and D. Cahen, *Proceedings of the indian academy of sciences - chemical sciences* **109**, 487 (1997).

- [41] J. Krüger, U. Bach, and M. Grätzel, *Adv. Materials* **12**, 447 (2000).
- [42] A. Salomon, D. Berkovich, and D. Cahen, *Appl. Phys. Letters* **82**, 1051 (2003).
- [43] Y. Selzer and D. Cahen, *Adv. Materials* **13**, 508 (2001).
- [44] Y. Selzer, A. Salomon, J. Ghabboun, and D. Cahen, *Ang. Chem. Int. Ed.* **41**, 827 (2002).
- [45] A. Vilan, J. Ghabboun, and D. Cahen, *J. Phys. Chem. B* **107**, 6360 (2003).
- [46] A. Vilan, A. Shanzer, and D. Cahen, *Nature* **404**, 166 (2000).
- [47] O. Gershevit, C. Sukenik, J. Ghabboun, and D. Cahen, *J. Am. Chem. Soc.* **125**, 4730 (2003).
- [48] L. Kavan and M. Grätzel, *Electrochimica Acta* **40**, 643 (1995).
- [49] A. Merson, T. Dittrich, Y. Zidon, J. Rappich, and Y. Shapira, *Appl. Phys. Letters* **85**, 1075 (2004).
- [50] I. Abayev, A. Zaban, F. Fabregat-Santiago, and J. Bisquert, *Phys. Stat. Sol. (a)* **196**, R4 (2003).
- [51] A. L. Roest, J. J. Kelly, D. Vanmaekelbergh, and E. A. Meulenkaamp, *Phys. Rev. Letters* **89** (2002).
- [52] E. A. Meulenkaamp, *J. Phys. Chem. B* **103**, 7831 (1999).
- [53] R. Gomer and G. Tryson, *J. Chem. Phys.* **66**, 4413 (1977).
- [54] Z. Samec, B. W. Johnson, and K. Doblhofer, *Surface Science* **264**, 440 (1992).
- [55] S. Trasatti, *Electrochimica Acta* **35**, 269 (1990).
- [56] S. Bastide, D. Gal, D. Cahen, and L. Kronik, *Review of Scientific Instruments* **70**, 4032 (1999).
- [57] S. Nakade, W. Kubo, Y. Saito, T. Kanzaki, T. Kitamura, Y. Wada, and S. Yanagida, *J. Phys. Chem. B* **107**, 14244 (2003).
- [58] S. Nakade, Y. Saito, W. Kubo, T. Kitamura, Y. Wada, and S. Yanagida, *J. Phys. Chem. B* **107**, 8607 (2003).
- [59] A. Solbrand, H. Lindström, H. Rensmo, A. Hagfeldt, S. E. Lindquist, and S. Södergren, *J. Phys. Chem. B* **101**, 2514 (1997).
- [60] A. Solbrand, K. Keis, S. Södergren, H. Lindström, S.-E. Lindquist, and A. Hagfeldt, *Solar Energy Materials and Solar Cells* **60**, 181 (2000).
- [61] A. Solbrand, A. Henningsson, S. Södergren, H. Lindström, A. Hagfeldt, and S. E. Lindquist, *J. Phys. Chem. B* **103**, 1078 (1999).

- [62] N. Kopidakis, E. A. Schiff, N.-G. Park, J. van de Lagemaat, and A. J. Frank, *J. Phys. Chem. B* **104**, 3930 (2000).
- [63] N. W. Duffy, L. M. Peter, and K. G. U. Wijayantha, *Electrochem. Com.* **2**, 262 (2000).
- [64] J. Nelson, S. A. Haque, D. R. Klug, and J. R. Durrant, *Phys. Rev. B* **63**, 205321 (2001).
- [65] F. Cao, G. Oskam, G. J. Meyer, and P. C. Searson, *J. Phys. Chem. B* **100**, 17021 (1996).
- [66] Y. Du and J. Rabani, *J. Phys. Chem. B* **107**, 11970 (2003).
- [67] H. Gerischer, *Electrochimica Acta* **34**, 1005 (1989).
- [68] M. K. Nazeeruddin, R. Humphry-Baker, P. Liska, and M. Grätzel, *J. Phys. Chem. B* **107**, 8981 (2003).
- [69] S. Rühle and D. Cahen, *J. Phys. Chem. B* **108**, 17946 (2004).
- [70] J. E. B. Randles, *Trans. Faraday Soc.* **52**, 1573 (1956).
- [71] J. R. Farrell and P. McTigue, *J. Electroanal. Chem.* **139**, 37 (1982).
- [72] N. W. Hansen and D. M. Kolb, *J. Electroanal. Chem.* **100** (1979).
- [73] E. R. Kötz, H. Neff, and K. Müller, *J. Electroanal. Chem.* **215**, 331 (1986).
- [74] J. O. M. Bockris and A. K. N. Reddy, (Plenum Press, New York, 1973), p. 841.
- [75] R. van de Krol, A. Goossens, and J. Schoonman, *J. Electrochem. Soc.* **144**, 1723 (1997).
- [76] J. G. Simmons, *J. Appl. Physics* **35**, 2655 (1964).
- [77] J. G. Simmons, *J. Appl. Physics* **34**, 2581 (1963).
- [78] D. Cahen and A. Kahn, *Adv. Materials* **15**, 271 (2003).
- [79] G. Ashkenasy, D. Cahen, R. Cohen, A. Shanzer, and A. Vilan, *Accounts of Chem. Research* **35**, 121 (2002).
- [80] D. Bonifazi, A. Salomon, O. Enger, F. Diederich, and D. Cahen, *Adv. Materials* **14**, 802 (2002).
- [81] N. Zenou, A. Zelichenok, S. Yitzchaik, R. Cohen, and D. Cahen, *Org. Thin Films ACS Sym. Ser.* **695** (1998).
- [82] F. Lenzmann, J. Krüger, S. Burnside, K. Brooks, M. Grätzel, D. Gal, S. Rühle, and D. Cahen, *J. Phys. Chem. B* **105**, 6347 (2001).
- [83] H. Gerischer, *Z. Physik. Chem. N. F.* **26**, 325 (1960).

- [84] S. R. Morrison, *Electrochemistry at semiconductor and oxidized metal electrodes* (Plenum Press, New York, London, 1980).
- [85] A. J. Nozik and R. Memming, *J. Phys. Chem. B* **100**, 13061 (1996).
- [86] Z. P. Liu, X. Q. Gong, J. Kohanoff, C. Sanchez, and P. Hu, *Phys. Rev. Letters* **91**, 266102 (2003).
- [87] G. Y. Wang, W. X. Zhang, D. Z. Jiang, and T. H. Wu, *Acta chimica sinica* **58**, 1557 (2000).
- [88] J. Krüger, R. Plass, M. Grätzel, P. J. Cameron, and L. M. Peter, *J. phys. Chem. B* **107**, 7536 (2003).
- [89] T. Oekermann, D. Zhang, T. Yoshida, and H. Minoura, *J. Phys. Chem. B* **108**, 2227 (2004).
- [90] N.-G. Park, J. van de Lagemaat, and A. J. Frank, *J. Phys. Chem. B* **104**, 8989 (2000).
- [91] L. M. Peter, E. A. Ponomarev, G. Franco, and N. J. Shaw, *Electrochimica Acta* **45**, 549 (1999).
- [92] V. Noack, H. Weller, and A. Eychmüller, *J. Phys. Chem. B* **106**, 8514 (2002).
- [93] A. Zaban, A. Meier, and B. A. Gregg, *J. Phys. Chem. B* **101**, 7985 (1997).
- [94] J. van de Lagemaat, N.-G. Park, and A. J. Frank, *J. Phys. Chem. B* **104**, 2044 (2000).
- [95] J. Weidmann, T. Dittrich, E. Konstantinova, I. Lauermann, I. Uhlendorf, and F. Koch, *Solar Energy Materials and Solar Cells* **56**, 153 (1999).
- [96] J. Bisquert, *J. Phys. Chem. B* **108**, 2323 (2004).
- [97] J. Bisquert and V. S. Vikhrenko, *J. Phys. Chem. B* **108**, 2313 (2004).
- [98] H. Scher and E. W. Montroll, *Phys. Rev. B* **12**, 2455 (1975).
- [99] Y. Kikuchi, T. Wakamatsu, H. Takahashi, and I. Endo, *Electrical Engineering in Japan* **143**, 1 (2003).
- [100] P. J. Cameron and L. M. Peter, *J. Phys. Chem. B* **107**, 14394 (2003).
- [101] R. van de Krol, A. Goossens, and E. A. Meulenkaamp, *J Appl Phys* **90**, 2235 (2001).



נוטים להתפזר בדומה לתוצאות שדווחו בספרות. אולם, מודלים פשטניים שפורסמו על תיאור מעבר שיעורי של זרם בהארה אינם כוללים בתוכם תהליכי פיזור, או שהם כוללים זאת באופן פשטני למדי. המודל המתואר בעבודה זו, כולל בתוכו תהליכי פיזור במעבר אלקטרוניים בצורה כמותית, דבר המאפשר התאמה למלכודות אלקטרוניים הנמצאות בשכבת  $\text{TiO}_2$ .

השוואה בין סימולציות למדידות תלויות עוצמה הראו שהרקומבינציה ב-  $\text{TiO}_2$  אינה עולה באופן לינארי עם צפיפות האלקטרוניים ב-  $\text{TiO}_2$ . מובן שתוצאה זו הינה מאוד רלוונטית לפעילותם של תאים סולרים, שכן היא מראה שמנגנון הרקומבינציה במקרה זה שונה באופן מהותי מזה הידוע בהתקני מצב מוצק (דוגמת Shockley, Read-Hall, Auger ורקומבינציה). כמו כן, מדידות אלו הראו שלמשק ה-  $\text{FTO}/\text{TiO}_2$  יש השפעה על הזרם בהארה.

בכדי לחקור את התפשטות הפוטנציאל האלקטרוסטטי קרוב ל-  $\text{FTO}$ , אור לייזר שבא מכיוון ה-  $\text{FTO}$  שימש ליצירת זוג חור-אלקטרון בממשק ה-  $\text{FTO}/\text{TiO}_2$ . מדידות נעשו גם על ממשקים מזופורוזיבים וגם על דחוסים. התוצאות הראו שעיקר הפוטנציאל נופל דווקא על שכבת ה-  $\text{TiO}_2$  הדחוסה ופחות על הממשק המזופורוזיבי.

יש לציין שחשיבות השדה החשמלי הנבנה בתאים סולרים מבוססי מולקולות הינה שנויה במחלוקת, שכן עדיין חסר מודל המתאר את עיקרון פעולתם של תאי שמש אלו. המחלוקת העיקרית קשורה בעצם לשדה האלקטרוסטטי בממשק שבין ה-  $\text{TiO}_2$  ל-  $\text{FTO}$  המוליך. גם כאן, הוצעו מספר מודלים שהתבססו על שדה הנבנה בממשק זה, וזאת ללא תצפית ניסיונית לשדה זה. לפיכך, חלק עיקרי בעבודת תזה זו הוקדש לשאלה: ' מהו עיקרון הפעולה של תאי שמש אלו, ומה חשיבותו של השדה החשמלי בממשק שבין ה-  $\text{TiO}_2$  למצע המוליך לפעילותם של תאי שמש?'

לבסוף עלה בידי, בעזרת המדידות במצב עמיד והשיעוריות וכמו כן גם מהסימולציות, להבין ולהבהיר מהם עקרונות הפעולה של תא שמש המבוסס על מולקולות צבע. בהמשך פיתחתי מודל שהתבסס גם על מדידות Kelvin probe. נתונים לגבי פונקציית העבודה הושגו ע"י מודיפיקציה של מערכת המדידה בכדי לאפשר גם מדידות מוצק ונוזל ביחס לאותו רפרנס. מנתונים אלו חישבתי את ערך המחסום האנרגטי בממשק בחושך, וזאת בניגוד למודלים הקיימים המבוססים על שדה אלקטרוסטטי הנבנה בממשק. מודל זה שפיתחתי הינו מודל המוגבל לתאי שמש בהם ממשק  $\text{FTO}/\text{TiO}_2$  מזופורוזיבי, שהוא הממשק הנפוץ בתאי שמש מבוססי מולקולות. עבור תאי שמש בעלי שכבת  $\text{TiO}_2$  דחוסה, Hopping הוא המנגנון המוצע המתאר את תהליך מעבר האלקטרוניים דרך המחסום האנרגטי בממשק.

## תקציר

תאי שמש מבוססי מולקולות צבע הינם אלטרנטיבה זולה היכולה להחליף את תאי השמש הקונבנציונליים. תאי שמש אלו מורכבים ממולקולות צבע הספוחות על שכבה מזופורוזיבית של  $\text{TiO}_2$  הטבולה באלקטרוליט המחובר חשמלית לאלקטרודת Pt. בהארה, דוגמת קרינה סולרית, אלקטרונים מוזרקים משכבת מולקולות הצבע המועררת לפס ההולכה של שכבת ה- $\text{TiO}_2$ , במקביל מולקולות הצבע המחומצנות נטענות מחדש ע"י האלקטרוליט.

ההבדל העיקרי בין תאי שמש מבוססי מולקולות צבע לאלו הקונבנציונליים, מבוססי צומת p-n, הינו ההפרדה בין המטען החיובי או השלילי העובר דרך השכבה המזופורוזיבית והאלקטרוליט. הפרדת המטען מתרחשת בממשק שבין ה- $\text{TiO}_2$  \ מולקולות הצבע \ אלקטרוליט: בעוד אלקטרונים עוברים בדיפוזיה דרך האלקטרוליט לעבר המגע הקדמי השקוף, מטענים שליליים עוברים דרך האלקטרוליט לאלקטרודת ה- Pt. מעבר אלקטרונים דרך שכבת ה- $\text{TiO}_2$  מתרחש תמיד קרוב לממשק עם הפאזה המוליכה המכילה מטענים חיוביים. ממשק זה גדול עד שלושה סדרי גודל מהשטח הגיאומטרי של שכבת ה- $\text{TiO}_2$ . מצבי שטח ב- $\text{TiO}_2$  פועלים כמלכודות לאלקטרונים ולכן מאטים בצורה משמעותית את קצב הדיפוזיה של האלקטרונים. על כן, במחקר זה התמקדתי בשאלה: 'מה שולט במעבר אלקטרונים דרך שכבה מזופורוזיבית של  $\text{TiO}_2$  טבולה באלקטרוליט?'

בכדי לחקור מעבר אלקטרונים בשכבת  $\text{TiO}_2$  מזופורוזיבית בתאי שמש, למדתי באמצעים ניסיוניים כיצד ספיחת מולקולות על  $\text{TiO}_2$  משנה את התכונות החשמליות של תא השמש. ניסויים אלו הראו שמתח המעגל הפתוח משתנה באופן סיסטמי עם שינוי דיפול המומנט של המולקולות. באופן מפתיע, גם הזרם בהארה הושפע באותו אופן. בעוד אפקט הפוטו-מתח מוסבר ע"י הזזה של פס ההולכה של ה- $\text{TiO}_2$  הנובעת מהדיפול מושרה, השפעת המולקולות על הזרם תחת הארה אינה ברורה. מדידות טרנספורט במצב העמיד של המערכת ותחת התפתחות בזמן נעשו בכדי לחקור על בוריה את השפעת המולקולות על ההולכה החשמלית ולהבין בצורה יסודית נדידת אלקטרונים בחומרים ננו-גבישיים. הקושי העיקרי במדידות במצב העמיד היה הכנת אלקטרודות בגודל מיקרו ע"י ליטוגרפיה. הקושי הניסיוני היה רב בכדי לאפשר מדידות הדירות, ותוצאות משמעותיות הושגו רק לגבי מספר מולקולות. מצאתי שהאפקט המולקולרי המשמעותי על ההולכה קשור בעצם להזזה בפס ההולכה של  $\text{TiO}_2$  כתוצאה מהדיפול המושרה כשם שהוזכר קודם לכן.

מדידות של הזרם בהארה תוך התפתחות בזמן נמצאו מתאימות לחקור את השפעת מצבי השטח בפער האסור ותהליך הרקומבינציה על מעבר האלקטרונים. התאמת המדידות הניסיוניות לסימולציה הראתה באופן ברור שתהליכי טרנספורט בשכבות ננו של  $\text{TiO}_2$





מכון ויצמן למדע  
WEIZMANN INSTITUTE OF SCIENCE

Thesis for the degree  
***Doctor of Philosophy***

חבור לשם קבלת התואר  
**דוקטור לפילוסופיה**

By  
***Sven Rühle***

מאת  
**סוון רולה**

מעבר אלקטרונים בשכבת  $TiO_2$  מזופורוזיבית  
ותכונות המגע החשמלי בממשק בין מוליך ל  $TiO_2$

***Electron transport in mesoporous  $TiO_2$  structures  
and  
contact properties at the  $TiO_2$ /conductive substrate interface***

Advisor  
***Prof. David Cahen***

מנחה  
**פרופ' דוד כאהן**

October 2004

חשוון תשס"ה

Submitted to the Scientific Council of the  
Weizmann Institute of Science  
Rehovot, Israel

מוגש למועצה המדעית של  
מכון ויצמן למדע  
רחובות, ישראל